

X-ray properties of ultraluminous X-ray sources

Tanuman Ghosh

Thesis Supervisor
Dr. Vikram Rana

Astronomy and Astrophysics
Raman Research Institute



June, 2023

*A Thesis submitted for the degree of
Doctor of Philosophy
at Jawaharlal Nehru University.*



Declaration

I, **Tanuman Ghosh** (Enrolment No.: RRI/2017/013), declare that the work reported in this thesis titled '*X-ray properties of ultraluminous X-ray sources*', is entirely original. This thesis is composed independently by me at Raman Research Institute (RRI) under the supervision of **Dr. Vikram Rana** and is the result of my own work unless otherwise stated. I further declare that the subject matter presented in this thesis has not previously formed the basis for the award of any degree, diploma, membership, associateship, fellowship, or any other similar title of any university or institution. I also declare that this thesis has been checked through the anti-plagiarism software OURIGINAL.

Signature of Candidate

Tanuman Ghosh

Research Fellow, RRI

Signature of Supervisor

Dr. Vikram Rana

Associate Professor, RRI

Raman Research Institute

Bengaluru 560080, Karnataka, INDIA

Date:

Place:



Certificate

This is to certify that the work contained in the thesis titled '*X-ray properties of ultraluminous X-ray sources*', submitted by **Tanuman Ghosh** (Enrolment No.: RRI/2017/013) to the Jawaharlal Nehru University for the award of the degree of *Doctor of Philosophy (Ph.D.)* in Physics, is the bonafide record of original research work carried out by the candidate from August 2017—June 2023, under my guidance and supervision at Raman Research Institute (RRI), Bengaluru, India. The results embodied in the thesis have not been submitted to any other University or Institute for the award of any degree or diploma.

Signature of Director
Prof. Tarun Souradeep
Director & Professor, RRI

Signature of Supervisor
Dr. Vikram Rana
Associate Professor, RRI

Raman Research Institute
Bengaluru 560080, Karnataka, INDIA

Date:

Place:

To my family

Acknowledgements

In the voyage of my long and exciting Ph.D. life, I was fortunate to have people around me whose constant support helped me thrive in all situations.

First, I would like to express my gratitude to my Ph.D. supervisor Dr. Vikram Rana for his guidance and valuable suggestions during these years. I would like to thank him for allowing me to work independently on any research problem I wanted to pursue.

I sincerely thank my collaborator Prof. Shiv Sethi (RRI, Bengaluru), with whom I have had long discussions on various subjects in Physics, which helped me become more confident as a researcher. I would also like to thank my other collaborator Dr. Matteo Bachetti (INAF, Italy), for useful discussions on various works which have helped improve my thesis. I would like to express my sincere gratitude to Prof. Banibrata Mukhopadhyay (IISc, Bengaluru), who has constantly motivated me in every situation and with whom I have collaborated and had stimulating discussions.

I am grateful to the Department of Science & Technology (DST), Government of India, and my institute for the fellowship I received during my Ph.D. I thank the Administration, IT & Computing Section, Estate office, and all the faculties for providing help whenever needed. The best place in the institute is its excellent library, where I spent most of my time throughout these years. Thanks to the library staff for their continuous support.

I was fortunate to have brilliant colleagues and a vibrant research environment in my department and the institute. Thanks to Agnibha, Anirban, Avik, and Hemanth, with whom I have had a lot of engaging discussion sessions during these years. Thanks to my friends, seniors, and juniors at RRI, whose company made my Ph.D. life a happy journey even in stressful times. I wholeheartedly thank Maheshwar for all the adda and for guiding me to learn cooking during the pandemic days. Thanks to Sandeep, Sanhita, Bapan, Dipak, Rishabh, Sagar, Anindya, Shovan, Saikat, Ranita, Nafisa, Subhajit, Sebanti, Vishnu, Ion, Rajkumar, Karamveer, Raj, Manami, Gunjan, Aman, Mukesh, Manish, Ashwin, Sourav, Sovan, Soumen, Sayantan, Jasim, Kinjal and many others for gifting me the joyful days. Thanks to the cooks in our hostel canteen who have cared for us in the difficult times

of our sickness and the pandemic. Thanks to all my friends with whom I was involved in sports and cultural activities.

My cordial gratitude to all of my teachers for whom I am who I am today. Finally, I would like to thank my parents, whose continuous support and encouragement helped my life progress.

List of Publications

- 1. *Constraint on the Accretion of NGC 6946 X-1 Using Broadband X-Ray Data*, **Ghosh T.**, Rana V., 2023, ApJ, 949, 78, DOI: [10.3847/1538-4357/acccf4](https://doi.org/10.3847/1538-4357/acccf4); [arXiv:2301.09837](https://arxiv.org/abs/2301.09837)
- 2. *Synchrotron Cutoff in Ultraluminous X-Ray Sources*, **Ghosh T.**, Sethi S., Rana V., 2023, ApJ, 948, 62, DOI: [10.3847/1538-4357/acbb60](https://doi.org/10.3847/1538-4357/acbb60); [arXiv:2210.02682](https://arxiv.org/abs/2210.02682)
- 3. *Spectral variability in NGC 1042 ULX1*, **Ghosh T.**, Rana V., 2022, MNRAS, 517, 4247, DOI: [10.1093/mnras/stac2979](https://doi.org/10.1093/mnras/stac2979); [arXiv:2209.02458](https://arxiv.org/abs/2209.02458)
- 4. *Hard X-Ray Flares and Spectral Variability in NGC 4395 ULX1*, **Ghosh T.**, Rana V., Bachetti M., 2022, ApJ, 938, 76, DOI: [10.3847/1538-4357/ac8f8f](https://doi.org/10.3847/1538-4357/ac8f8f); [arXiv:2202.01432](https://arxiv.org/abs/2202.01432)
- 5. *Super-Eddington accretion on to a stellar mass ultraluminous X-ray source NGC 4190 ULX1*, **Ghosh T.**, Rana V., 2021, MNRAS, 504, 974, DOI: [10.1093/mnras/stab774](https://doi.org/10.1093/mnras/stab774); Erratum: 2023, MNRAS, 522, 1183, DOI: [10.1093/mnras/stad997](https://doi.org/10.1093/mnras/stad997); [arXiv:2103.10265](https://arxiv.org/abs/2103.10265)

Other Publications/proceedings (Not part of the thesis work)

- 1. *Geometric phase for Dirac Hamiltonian under gravitational fields in the nonrelativistic regime*, **Ghosh T.**, Mukhopadhyay B., 2021, IJMPD, 30, 2150090-417, DOI: [10.1142/S0218271821500905](https://doi.org/10.1142/S0218271821500905); [arXiv:2010.05945](https://arxiv.org/abs/2010.05945)
- 2. *Gravitational geometric phase*, Mukhopadhyay B., **Ghosh T.**, Kanti Ganguly S., 2023, proceeding of the 16th Marcel Grossmann Meeting (MG16), 689, DOI: [10.1142/9789811269776_0052](https://doi.org/10.1142/9789811269776_0052); [arXiv:2111.03277](https://arxiv.org/abs/2111.03277)

Signature of Candidate
Tanuman Ghosh
Research Fellow, RRI

Signature of Supervisor
Dr. Vikram Rana
Associate Professor, RRI

Synopsis

Introduction

Ultraluminous X-ray sources (ULXs) are one of the brightest X-ray emitting sources with luminosity exceeding the classical Eddington limit of a $10M_{\odot}$ black hole (i.e., $L_x > 10^{39}$ erg s $^{-1}$). Initially, the powerhouse of ULXs was thought to be sub-Eddington accretion onto intermediate-mass black holes (IMBHs). However, recent spectral and timing studies have established that few sources are certainly stellar-mass compact objects like neutron stars (NSs). Many ULX populations could also be stellar-mass black holes (StMBHs). Nevertheless, there is a sub-class of sources known as hyperluminous X-ray sources (HLXs), which are still considered candidate IMBHs. ULXs are understood to be unique X-ray binary systems since their spectral properties are observed to be different from most of the sub-Eddington X-ray binaries or AGNs. Interestingly, most ULXs have shown unique spectral curvature $\sim 6\text{--}10$ keV, confirmed by broadband X-ray studies. These sources are mysterious since many essential questions about their properties remain unanswered. For example, what is the powerhouse of such high luminosity in the ULXs, why do their spectral properties differ from Galactic X-ray binaries (XRBs), what is the origin of unique spectral curvature in these sources, and what is the nature of the central compact objects? We study some individual sources using different space-based X-ray observatories, examine their timing and spectral properties, and explore plausible answers to some questions. We specifically explore some of their fundamental characteristics, like the nature of the compact objects and the physics of the accretion flow, and propose a new theoretical model to explain the unique spectral curvature of ULXs.

X-ray flaring in NGC 4395 ULX1

We report the detection of X-ray flaring events in NGC 4395 ULX1 using XMM-Newton observations. We find that the spectral state of this source is best classified as intermediate between the soft and supersoft ultraluminous states. The flaring incidents are found to be spectrally harder than the steady-emission intervals. Consequently, we also find that the high-energy photons exhibit higher fractional variability than the soft photons.

The continuum spectra are described by a two-component thermal accretion disk, i.e., one Keplerian disk and a slim disk. In all observations, we detect a broad hump-like feature around ~ 0.9 keV on top of the continuum spectra. A higher slim-disk temperature due to a higher mass accretion rate is a characteristic feature during the flaring events. The luminosity–temperature profile is broadly consistent with both $L \propto T^2$ and $L \propto T^4$ relations. The empirical prediction for a slim accretion disk in the case of super-Eddington accretion onto a stellar-mass compact object is $L \propto T^2$, which is a possible scenario in ULX1. The origin of the flaring events is understood as an intrinsic change in accretion rate or the presence of variable clumpy wind in the inner region of the accretion disk.

Spectral variability in NGC 1042 ULX1

We report X-ray spectral variability in an ultraluminous X-ray source NGC 1042 ULX1, using archival XMM-Newton and recent NuSTAR observations. In long-term evolution, the source has shown a trend of variation in spectral hardness. The variability in different XMM-Newton observations is prominent above ~ 1 keV. Cool thermal disk component with a characteristic temperature of ~ 0.2 keV manifests that the spectral state of NGC 1042 ULX1 in all epochs is similar to that of the ultraluminous state sources. An apparent anti-correlation between luminosity and powerlaw index demonstrates that the source becomes spectrally harder when it is in a brighter state. That is conceivably related to variation in accretion rate, the strength of comptonization, wind/outflow in the system, or a manifestation of varying disk occultation. Typical hard ultraluminous type spectra indicate that NGC 1042 ULX1 is a low inclination system in general. Spectral properties suggest that, like many other ULXs which show spectral curvature around ~ 6 – 10 keV, NGC 1042 ULX1 could be another stellar-mass super-Eddington accretor.

Synchrotron cutoff in ULXs

The origin of spectral curvature at around $E \simeq 10$ keV in ultraluminous X-ray sources is not well understood. We propose a simple but novel theoretical model based on synchrotron radiation to explain this spectral cutoff. We show that emission from different latitudes can explain the spectral cur-

vature, which is based on the underlying equation:

$$dI_n = \frac{e^2 \omega^2}{2\pi c} [\tan^2 \theta J_n^2(n\beta \cos \theta) + \beta^2 J_n'^2(n\beta \cos \theta)] d\Omega, \quad (1)$$

where $\beta = v/c$, B is the magnetic field strength, and θ is the angle between radiated emission and the particle's orbital plane. $J_n(x)$ is the Bessel function and $J_n'(x)$ its derivative. The integer n denotes the discrete energy levels of electron's energy with $\omega = n\omega_B$, where $\omega_B = eB/\gamma mc$, and $\gamma = 1/\sqrt{1-\beta^2}$. We show that relativistic plasma can give rise to such spectral curvature for neutron star magnetic fields ($B \sim 10^{12}$ G) due to the variation in the latitude of synchrotron radiation. A semi-relativistic plasma ($\gamma \sim 10$) with high latitude angle or a highly relativistic plasma ($\gamma \sim 10^5$) with emission close to the electron's orbital plane can adequately explain this curvature for two pulsar ULX systems, namely, NGC 5907 ULX1 and NGC 7793 P13. A corollary of our study is that most ULXs that show such spectral cutoff might be neutron star systems.

We also discuss results from the analyzed X-ray data of a few other ULX sources (e.g., NGC 4190 ULX1, NGC 4254 X2, NGC 1291 ULX1, NGC 4244 ULX1). We investigate their spectral properties with different models and explore their physical implications. The study of several ULX sources helps us understand and compare their physical characteristics. We study a ULX source NGC 6946 X-1, which exhibits soft spectra. A study of its continuum spectral properties shed light on the underlying accretion mechanism in this source.

Summary and future prospects

We have studied some individual ULXs and their spectral and timing properties, which helped us understand the physical scenarios in those systems. We estimated crucial physical properties like the mass of the compact object and possible magnetic field strength for some of these sources. We find the flaring events in NGC 4395 ULX1 for the first time, which is an interesting transient event that occurred in the ULX. We deciphered some characteristics of the transient flaring events in this ULX, which redirects to the origin of such incidents, such as an intrinsic change in accretion rate or the presence of variable clumpy wind that partially occults the inner region and imprints the hard emission variability. We find spectral variability in

NGC 1042 ULX1 and anti-correlation between spectral photon index and luminosity which can be interpreted as geometrically beamed hard emission through the optically thin tunnel or direct hard emission from neutron star accretion column, or varying strength of Comptonization due to change in accretion rate. We also develop a new theoretical model based on synchrotron radiation to explain the origin of ULX spectral curvature. We show the congruence of the theoretical model and data for two pulsar ULXs. In the future, this theoretical model can be further investigated extensively for multiple ULX sources. Investigation of other individual sources and class of ULX sources is crucial to constrain the physics of these systems. In the future, we would also undertake a detailed study of the wind or outflow mechanism due to super-Eddington accretion. One aspect for future studies will be a dedicated investigation of HLXs, their timing, and spectral properties. Future missions like Athena and XRISM will be vital to decipher more mysteries of ULXs owing to their high effective area and high spectral resolution.

Signature of Candidate

Tanuman Ghosh

Research Fellow, RRI

Signature of Supervisor

Dr. Vikram Rana

Associate Professor, RRI

Contents

List of Publications	xi
Synopsis	xiii
List of Figures	xxi
List of Tables	xxix
1 Introduction	1
1.1 X-ray Astronomy	1
1.2 X-ray binaries and accretion	2
1.2.1 Accretion	2
1.2.2 Accretion luminosity and Eddington limit	3
1.2.3 Sub-Eddington accretion and spectral states	5
1.3 Ultraluminous X-ray sources	7
1.3.1 Super-Eddington accretion	9
1.3.2 ULX spectra and different states	13
1.3.3 Wind and atomic features	16
1.3.4 Timing properties of ULX	18
1.4 Radiative processes in ULX	20
1.4.1 Thermal emission	21
1.4.2 Non-thermal emission	23

Contents

1.5	Thesis outline	25
2	X-ray observatories and data analysis techniques	27
2.1	X-ray observatories	27
2.1.1	XMM-Newton	28
2.1.2	NuSTAR	30
2.1.3	NICER	31
2.2	Data analysis techniques	32
2.2.1	Imaging analysis	33
2.2.2	Timing analysis	34
2.2.3	Spectral analysis	35
3	X-ray flaring in NGC 4395 ULX1	37
3.1	Prologue	37
3.2	Observation details	39
3.3	Timing Analysis	40
3.4	Spectral Analysis	45
3.4.1	Time-averaged spectroscopy	46
3.4.2	Time-resolved spectroscopy	50
3.5	Discussions	52
4	Spectral variability in NGC 1042 ULX1	61
4.1	Prologue	61
4.2	Observation details	62
4.3	Results	65
4.3.1	Spectral Analysis	65
4.3.2	Timing Analysis	71
4.4	Discussions	71
4.4.1	Accretion states of NGC 1042 ULX1	72
4.4.2	Nature of the accretor	75
4.4.3	Anti-correlation between $\Gamma-L_X$	75
5	Synchrotron cutoff in ULXs	81
5.1	Prologue	81

Contents

5.2	Synchrotron radiation: fundamentals	83
5.3	Analytic approximation of Bessel function	85
5.4	Pre-processing of data	89
5.4.1	Data reduction process	90
5.5	Analysis and Results	91
5.6	Discussions	95
6	Super-Eddington accretion onto ULXs	99
6.1	Prologue	99
6.2	Accretion constraint on NGC 6946 X-1	100
6.2.1	Observation details	101
6.2.2	Analysis and Results	102
6.2.3	Discussions	106
6.3	Accretion constraint on other ULXs	115
6.3.1	Observations and Results	116
6.3.2	Discussions	119
7	Summary and Future prospects	123
7.1	Summary	123
7.1.1	Hard X-ray flaring in NGC 4395 ULX1	123
7.1.2	Variability in spectra of NGC 1042 ULX1	124
7.1.3	Synchrotron spectral cutoff in ULXs	124
7.1.4	Super-Eddington accretion mechanism in ULXs	125
7.2	Future Prospects	126
	References	129

List of Figures

- 1.1 Different spectral states of sub-Eddington black hole XRBs are shown in a schematic diagram via a jet-disk coupling model taken from figure 7 of [Fender et al. \(2004\)](#). The upper central panel shows the hardness-intensity (HID) diagram, where hardness (ratio between count rates of hard and soft photons) increases to the right and intensity increases upwards. The lower panel shows how the bulk Lorentz factor of the outflow depends on the hardness. The sketches outside describe the picture of contributions from the jet (blue), corona (yellow), and accretion disk (red). The spectral state denoted as HS is the high/soft state, VHS/IS is the very high/intermediate state, and LS is the low/hard state. 6
- 1.2 The super-Eddington slim accretion disk schematic diagram taken from figure 1 of [Dotan & Shaviv \(2011\)](#) shows different regions of the accretion disk, including wind. The different regions are depicted as e.g., (A) the sub-Eddington thin accretion disk, (B) the disk becomes radiation-pressure dominated, the energy release becomes correlated to the Eddington limit, and the disk begins to inflate, (C) Above the convection layer, a porous layer is generated, (D) wind is accelerated from the region where the porous structure is optically thin, (E) the photosphere located within the wind. 11

List of Figures

1.3	Schematic representation of the super-critical accretion scenario with the outflowing wind into consideration (taken from figure 1 of Middleton et al. 2015a). The inclination of line of sight of the observer is θ , wind cone opening angle is θ_w . When θ is small (position 1), the maximum unobscured emission from the hot inner disk is observed. With moderate θ , a significant fraction of hard X-ray flux will be scattered out of the line of sight due to wind (position 2), and with very high θ (position 3), the outer photosphere of the wind will dominate the emission, which would be dominant in UV and mostly out of the X-ray bandpass.	12
1.4	From figure 1 of Sutton et al. 2013 , three different spectral types in ULXs are shown.	14
1.5	An example figure of Quasi-periodic oscillation discovered in ULX. Image is taken from figure 1 of Atapin et al. (2019)	17
1.6	Detection of pulsation in the Fourier power spectra of NGC 7793 P13 light curves. The inset in the figure exhibits the folded profiles. Image is taken from figure 1 of Israel et al. (2017b)	20
1.7	The model spectra of “ p ” free MCD emission shown for three values of p . The standard thin disk is for $p = 0.75$. While the p value decreases, the geometry of the inner region of the disk gets modified due to a higher accretion rate. In fact, it is seen that for a fixed temperature, a smaller p value gives a more enhanced soft energy band in the observed spectrum compared to the thin disk. The $p = 0.5$ limit is for a slim disk. The model spectra are plotted for fixed temperature and normalization using XSPEC (see Chapter 2) model diskpbb.	23
2.1	Artist impression of XMM-Newton observatory. Image credit - ESA/XMM-NEWTON (https://xmm-tools.cosmos.esa.int/external/xmm_science/gallery/images/Telescope.jpg).	28
2.2	Diagram of NuSTAR observatory. The top is the deployed, and the bottom is the stowed configuration. Image credit - https://heasarc.gsfc.nasa.gov/Images/nustar/Fig_observatory.pdf (see also figure 1 of Harrison et al. 2013).	30

List of Figures

2.3	The comparison of effective areas of different X-ray telescopes. XMM-Newton and NuSTAR are active imaging observatories with high effective areas in the soft and hard energy bands, respectively. Image credit - https://www.nustar.caltech.edu/page/researchers	32
2.4	Example of an RGB image from XMM-Newton pn camera for NGC 1291 ULX1 studied in this thesis. The soft energy band (red image) is in 0.3–1.0 keV, the medium band (green image) is in 1.0–3.0 keV, and the hard energy band (blue image) is in 3.0–10.0 keV energy range. The image is smoothed with a Gaussian function for visual purposes.	33
3.1	2000 seconds binned XMM-Newton pn light curves of ULX1 for four individual epochs, namely XM1, XM2, XM3, and XM4. The soft (0.3–1.0 keV) and hard (1.0–8.0 keV) count rates are shown in the first and second panels, respectively. The hardness ratio, which is defined as the hard/soft photon count rate, is shown in the third panel. The fourth panel shows the sum of the soft and hard band lightcurves, i.e., the total lightcurve. A steady but slight uprising trend of the flux is observed in the first epoch (XM1). In the second epoch (XM2), a flaring episode occurred from around 30 ksec to 80 ksec of that observation. Another steady but slightly declining trend of flux is seen in the third epoch (XM3). Finally, in the fourth epoch (XM4), a large flaring episode happened, covering most portion (~ 80 ksec) of that observation. As seen in the hardness ratio plots, the prominent flares in XM2 and XM4 are predominant in the hard energy band.	41
3.2	The example power spectral density plots for XM4 pn (left) and MOS2 (right) observations, respectively. This shows the presence of power law-shaped red noise in the power spectrum.	42
3.3	For XM2 (left) and XM4 (right) epochs of observation, different transient intervals are defined. The pre-flare, flare, and post-flare intervals are separately indicated. As discussed in the text, the pre-flare and post-flare intervals are combined to get the “non-flaring” interval.	44

List of Figures

3.4 Top: The unfolded MOS1 spectra for different epochs are plotted. Simple powerlaw model of zero photon index ($\Gamma = 0$) is used to unfold the spectra. The normalization of the model is kept arbitrarily high for plotting purposes. A significant long-term spectral variability is observed in different epochs of ULX1 spectra. In the left panel, the MOS1 spectra of the XM1 and XM3 epochs exhibit overlapping spectral features. XM2 and XM4 epochs clearly show differences in spectral shapes and divergence in hard spectral regimes. From the time-resolved spectroscopic analysis, the flaring and non-flaring spectra of the XM2 and XM4 epochs are plotted in the middle and right panels. A similar divergence in spectral characteristics predominantly above 1 keV is seen in these two figures. Bottom: The residuals of the best-fit continuum are shown for MOS1 spectra corresponding to the epochs shown in the top panels. For plotting purposes, the Gaussian component is removed from the best-fit model to show the significant contribution of Gaussian in the spectra. 47

3.5 The model components are shown for MOS1 spectra of different epochs. The red component is the gaussian, green represents the diskbb, and blue represents diskpbb components. Black represents the total model. The variation in the diskpbb model component due to flaring incidents is clear from the figure. 52

3.6 Relation between the unabsorbed bolometric luminosity of the hard slim disk component vs. temperature of that disk. The 95% confidence intervals on the normalizations of the powerlaw relations are indicated with the shaded regions. 55

4.1 The XMM-Newton and NuSTAR unfolded spectra of ULX1. A zero photon index powerlaw model is used to unfold the spectra and for visual purposes, the spectra have been rebinned. The MOS1 spectra are plotted for all XMM-Newton observations except for the XM6 epoch, for which the MOS2 spectrum is shown. For the N1 observation, the spectrum from the FPMA module is presented. 64

List of Figures

4.2	The N_H and Γ variation over different XMM-Newton observation epochs are shown in the top left and right panels, respectively. The relation between the N_H and Γ is depicted in the bottom panel. We utilize an absorbed powerlaw model with the N_H parameter being allowed to vary for different epochs of observation for these parameter estimates.	65
4.3	The spectra and residuals are shown for all XMM-Newton and NuSTAR observations. The <code>diskbb+powerlaw</code> model is considered for XMM-Newton epochs, and the <code>cutoffpl</code> model is considered for the NuSTAR observation. The black, red, and green colors correspond to MOS1, MOS2, and pn, while blue and light blue colors correspond to FPMA and FPMB data, respectively. The corresponding additive models are also shown in the top panels of each figure.	69
4.4	A representative plot of the background subtracted cleaned 3.0–20.0 keV light curve from NuSTAR FPMA with a 5000 seconds binning.	72
4.5	Negative correlation between $\Gamma-L_X$ for different XMM-Newton epochs for 0.3–8.0 keV energy range (Left). The same quantities are plotted on the right side also but for a 2.0–8.0 keV energy range.	76
5.1	The synchrotron spectra are shown as a function of multipoles (Eq. (5.1)) for different latitudes. The $B = 5 \times 10^{11}$ Gauss and $\gamma = 10$ is used for this figure. The role of high-latitude emission in introducing spectral curvature is seen. For a fixed B and γ , the spectral cutoff shifts to a lower harmonic due to high-latitude emission.	83
5.2	The 5–25 keV spectra of NGC 5907 ULX1 (left) and NGC 7793 P13 (right) are displayed for multiple NuSTAR observations. As discussed in the text, the spectra above ~ 5 keV show similar spectral shapes with variations in flux in different observations for both sources.	90

List of Figures

5.3 Example plots depicting the congruence of the theoretical model with the spectra of two ULXs. Each plot is shown for one observation of each source. The data with the model over-plotted are shown in the top panels, and corresponding residuals are shown in the bottom panels. The models shown here are for 1° angle in case of NGC 5907 ULX1 (left; Observation - 80001042002) and 30° angle for NGC 7793 P13 (right; Observation - 90301326002). 93

5.4 Based on the MCMC analysis described in the text, we display corner plots for two parameters N and x_{min} for emission angles: $1^\circ, 15^\circ, 30^\circ$ (from left to right). The top and bottom panels correspond to NGC 5907 ULX1 (Observation - 80001042002) and NGC 7793 P13 (Observation - 90301326002), respectively. The 0.16, 0.5, and 0.84 quantiles are shown as vertical lines in the figures. 50 bins are used in the histograms, which are smoothed with 3σ Gaussian kernel. 94

6.1 Presence of ~ 0.9 keV broad hump feature and a high energy spectral turnover is apparent from the residual of XN1 broadband spectra corresponding to an absorbed `powerlaw` fit. Data have been rebinned for visual purposes. 103

6.2 Unfolded broadband spectra of NGC 6946 X-1 for four simultaneous XMM-Newton and NuSTAR observations. The spectra are unfolded using a `powerlaw` model of 0 index and arbitrary normalization. For clarity, only MOS2 and FPMA spectra are exhibited for all four epochs. It is apparent from visual inspection that all four epochs show overlapping spectral features. Data have been rebinned for visual purposes. 104

6.3 The NGC 6946 X-1 spectra, model components, and residuals are shown for all epochs simultaneous fit with `tbabs*(gaussian+diskbb+diskpbb)` model. Data have been rebinned for visual purposes. 108

List of Figures

- 6.4 Left: For three different spins of the black hole, the variation of the estimated mass as a function of the disk inclination angle is shown. The non-rotating black hole scenario of $a^* = 0$, a moderate spin of $a^* = 0.5$, and a maximally rotating case of $a^* = 0.998$ are shown in the figure. Right: The dependency of estimated magnetic field strength for a neutron star system on the disk inclination angle is depicted. 111
- 6.5 The best-fit spectra with models and residuals are shown for four sources. NGC 4190 ULX1 (top left; ID - 0654650301), NGC 1291 ULX1 (top right; ID - 0201690201), NGC 4254 X2 (bottom left; ID - 0913090101), and NGC 4244 ULX1 (bottom right; ID - 0553880201) spectra are shown. The `diskbb+cutoffpl` model fit is shown for NGC 4254 X2, and the `diskbb` model fit is shown for the other three sources. 121

List of Tables

3.1	Details of 2018-2019 observations of NGC 4395 ULX1 discussed in this chapter. The exposure times noted here are flare-corrected approximate livetime CCD exposures for pn/MOS1/MOS2.	38
3.2	Fractional variability in pn and MOS lightcurves for all four epochs.	44
3.3	The best fit model (<code>tbabs(GAL)*tbabs*(gauss+diskbb+diskpbb)</code>) parameters of NGC 4395 ULX1 XMM-Newton spectra for the four epochs. The absorbed flux F_x and luminosity L_x are calculated in the 0.3–10.0 keV energy range. The Galactic absorption is fixed to 0.04×10^{22} cm^{-2} . “ p ” value of <code>diskpbb</code> model is fixed to 0.50, resembling a slim disk. The distance is assumed to be 4.76 Mpc (Vinokurov et al. 2018) to calculate the luminosity.	46
3.4	Parameters for the time-resolved spectroscopic analysis of XM2 and XM4 epochs using best-fit model same as in table 3.3.	50
4.1	The observation details of NGC 1042 ULX1 utilized in the chapter. The cleaned spectral exposures are mentioned for MOS1/MOS2/pn for XMM-Newton and FPMA/FPMB for NuSTAR in ksec unit	63
4.2	Spectral parameter details for the <code>powerlaw</code> model with linked N_H , in seven epochs of XMM-Newton observation of NGC 1042 ULX1. We list the observed (absorbed) fluxes and luminosities in 0.3–8.0 keV energy range. The intrinsic (unabsorbed) fluxes are typically ~ 1.2 –1.6 times the observed fluxes.	67

List of Tables

4.3	Spectral parameter details for the <code>diskbb+powerlaw</code> model in seven epochs of XMM-Newton observation of NGC 1042 ULX1. The observed (absorbed) fluxes and luminosities are measured in 0.3–8.0 keV energy range. We also quantify the intrinsic flux of the individual additive components in the same energy range.	67
5.1	The results from the python curve fit with the best-fit parameters and χ^2 are listed for 7 NuSTAR observations of NGC 5907 ULX1 and 10 NuSTAR observations of NGC 7793 P13. The errors are calculated with 1- σ confidence from the covariance matrix using the parameter <code>absoulte_sigma=True</code>	96
6.1	Sample of ULXs studied in this chapter	100
6.2	Observation log of NGC 6946 X-1. pn data are not used for observation 0870830201, and MOS1 data are not available for observation 0870830401.	101
6.3	Parameters for the fitted <code>tbabs*(gaussian+highcut*powerlaw)</code> model of NGC 6946 X-1 broadband spectra. The total absorbed flux (F_x) is measured in the 0.3–20.0 keV energy range.	106
6.4	Parameters for the fitted <code>tbabs*(gaussian+diskbb+diskpbb)</code> model of NGC 6946 X-1 broadband spectra. The bolometric unabsorbed total flux and the flux from individual disk components are measured in the 0.01–100.0 keV energy range.	107
6.5	Observation log of XMM-Newton data for four sources. In observation ID 0654650101 of NGC 4190 ULX1, the flaring corrected cleaned exposure time of pn data is extremely low (~ 0.1 ksec), hence not utilized for the spectral analysis.	116
6.6	The fitting parameters for <code>tbabs*powerlaw</code> model for four sources. The flux (F_x) is the absorbed flux in 0.3–10.0 keV energy range.	119
6.7	The fitting parameters for <code>tbabs*cutoffpl</code> model for four sources. The flux (F_x) is the absorbed flux in 0.3–10.0 keV energy range.	120
6.8	The fitting parameters for <code>tbabs*(diskbb+cutoffpl)</code> model for NGC 4254 X2. The flux (F_x) is the absorbed flux in 0.3–10.0 keV energy range.	120

List of Tables

6.9 The fitting parameters for `tbabs*(diskpbb)` model for three sources.
The flux (F_x) is the absorbed flux in 0.3–10.0 keV energy range. 120

Introduction

1.1 | X-ray Astronomy

Human curiosity to unravel the mysteries of the universe is pre-historic. This curiosity guided our mind to perceive the surroundings with the depth of logic and philosophy. As the “Homo Sapiens” progress through the modern era, our understanding of the universe is primarily based on experiments, logical inference from observations, and explaining possible theories, which are the basis of “Science.” Broadly defined, Astronomy is a branch of natural science where we study the universe as a whole and its constituents, i.e., the celestial objects. Since the invention of telescopes, observation of the sky has been revolutionized, and we can see cosmic events that were impossible to observe with the naked eye. The human eye can see a narrow frequency band of the electromagnetic spectrum, known as the “optical” spectrum. The wavelength of the received spectrum depends on the energy of the underlying physical phenomena from which the photons have been generated. Generally, the higher energetic band of the electromagnetic spectrum comes to us from the most violent phenomena occurring in the universe. The “X-ray” frequency belongs to such high energy phenomena.

X-ray astronomy sets off a new era since the observations of X-rays from the Scorpius constellation, a first of its kind outside of our solar system ([Giacconi et al. 1962](#)). Since X-rays cannot penetrate the Earth’s atmosphere, the observa-

tories which detect X-rays are all space-based. The celestial objects from which the modern observatories detect a significant fraction of X-rays are mostly extreme gravitating objects like active galactic nuclei, compact objects like white dwarfs, neutron stars and black holes, galaxy clusters, supernova remnants, and stars.

1.2 | X-ray binaries and accretion

A star remains in a state of equilibrium when it has sufficient fuel that burns to provide radiation pressure, counter-balancing its gravitational pull. When the star runs out of such fuel, it collapses due to its own gravitational pull and can form a compact object in the final stage of its life cycle. Depending on the initial mass of the star, it can end up in the states like a white dwarf, neutron star, or black hole. In some cases, another star often comes under the gravitational influence of the compact object and forms binary systems. The central compact object engulfs material from the companion by a process called “accretion”. Binary systems with the core of white dwarfs, neutron stars, or black holes are significant emitters of X-rays. Typically, when the system has a core of a neutron star or a black hole, accreting from their companion stars, they are named “X-ray binary (XRB)” systems (see, e.g., [Frank et al. 2002](#); [Shapiro & Teukolsky 1983](#)).

1.2.1 | Accretion

The primary source of the power from the binary systems is understood to be the extracted gravitational potential energy from the accreting material falling onto the compact objects ([Frank et al. 2002](#)). Suppose the mass of the gravitating body is M with a radius R . Accretion of mass m would release the gravitational potential energy as,

$$\Delta E_{acc} = \frac{GMm}{R}, \quad (1.1)$$

where G is the gravitational constant. This extracted energy is primarily liberated in the form of electromagnetic radiation. If we relate the accretion energy

with the emitted energy, which is a fraction of the total energy of the accreting material, we get,

$$\frac{GMm}{R} = \eta mc^2, \quad (1.2)$$

where η is the efficiency of the accretion given by the compactness (M/R) of the accreting object, i.e., $\eta = GM/Rc^2$, and c is the speed of light in the vacuum. For a simple nuclear fusion reaction, i.e., the well-known hydrogen “burning” process, $\eta = 0.007$. However, generally, for X-ray binaries like a black hole or neutron star systems, the η is assumed to be ~ 0.1 (Frank et al. 2002). Nonetheless, it is important to note that accretion efficiency significantly increases with increasing spin of a black hole (Reynolds 2021). This is due to the fact that observed emission from a black hole accretion predominantly comes from the inner region of the accretion flow close to the black hole horizon, which is practically the inner stable circular orbit (ISCO). This ISCO strongly depends on the spin of the black hole, inducing spin-dependence of the accretion efficiency η . In addition, efficiency can highly vary in the case of neutron star accretion, where the kinetic energy of the matter falling on the hard surface of the neutron star would efficiently radiate thermal energy, which increases the accretion efficiency value (D’Angelo et al. 2015; Narayan & Yi 1995).

1.2.2 | Accretion luminosity and Eddington limit

The luminosity of astrophysical sources is defined by the total energy emitted per unit time from those systems. For the accretion process, thus, the luminosity would be,

$$L_{acc} = \frac{GM\dot{m}}{R} = \eta \dot{m}c^2, \quad (1.3)$$

where \dot{m} is the accretion rate. There is, however, a limit of maximum possible luminosity from a star to maintain the condition of hydrostatic equilibrium, i.e., outward radiation pressure balancing the inward gravitational pressure. Assuming fully ionized hydrogen plasma and steady spherically symmetric accre-

tion, this maximum limit of luminosity is known as the Eddington luminosity (Frank et al. 2002), and it is given by,

$$L_{Edd} = \frac{4\pi GMm_p c}{\sigma_T} \simeq 1.3 \times 10^{38} \left(\frac{M}{M_\odot}\right) \text{ erg s}^{-1}, \quad (1.4)$$

where m_p is the proton mass, σ_T is the Thomson scattering cross-section, and M_\odot denotes the solar mass. This expression has limitations owing to the assumptions of spherically symmetric steady accretion and scattering by fully ionized hydrogen plasma. In general, if the hydrogen mass fraction is X , then (Poutanen et al. 2007),

$$L_{Edd} \simeq 1.5 \times 10^{38} \left(\frac{M}{M_\odot}\right) \left(\frac{1.7}{1+X}\right) \text{ erg s}^{-1}. \quad (1.5)$$

See Poutanen et al. 2007, where solar hydrogen mass fraction $X = 0.7$ is assumed, and in the fully ionized hydrogen assumption, $X = 1$. This maximum luminosity limit has utter importance in understanding and classifying sources based on the emitted power. The accretion rate that is responsible for the Eddington luminosity is known as the Eddington accretion rate (\dot{m}_{Edd}), such as,

$$L_{Edd} = \eta \dot{m}_{Edd} c^2. \quad (1.6)$$

For a solar mass ($1M_\odot$) object, it is expected that the luminosity of the source would be $L_x \lesssim 1.3 \times 10^{38} \text{ erg s}^{-1}$ (from Eq. 1.4). Most Galactic X-ray binary population exhibits luminosity less than their Eddington limit. Such accretion processes are known as sub-Eddington accretion. If the luminosity of the source becomes larger than the Eddington limit, for a fixed accretion efficiency, it is expected that the accretion rate would be higher than the Eddington accretion rate. Such an accretion process is known as super-Eddington accretion.

For example, a $10M_\odot$ object is expected to emit within the luminosity range of $1.3 \times 10^{39} \text{ erg s}^{-1}$. If the intrinsic luminosity is more than this limit, one can expect that the host is much more massive than $\sim 10M_\odot$. Many active galactic nuclei (AGNs) exhibit very high luminosity, e.g., $\sim 10^{45}$ – $10^{47} \text{ erg s}^{-1}$. They are supermassive black holes (SMBHs) at the center of the galaxies, with Millions to Billions of times more massive than solar mass. Thus, such high luminosity is

possible within the sub-Eddington accretion regime. However, if a $1M_{\odot}$ compact object like a neutron star shows luminosity $\sim 10^{39}$ – 10^{41} erg s $^{-1}$, then it is expected that their accretion mechanism is super-Eddington in nature.

1.2.3 | Sub-Eddington accretion and spectral states

Most XRBs are sub-Eddington accreting systems where the central compact object is a black hole or a neutron star engulfing material from the companion star. Depending on the mass of the companion star, the XRBs can be high-mass XRBs (HMXBs) or low-mass XRBs (LMXBs). Typically, for HMXBs, the accretion process is wind-fed accretion, whereas, for LMXBs, the process is Roche-Lobe overflow.

Interestingly, the black hole XRBs show transient properties like sudden outbursts and quiescent phases. The quiescent state has orders of magnitude less luminosity compared to the luminosity in an active state of the sources. The outburst phase generally exhibits different spectral states and transitions between them (see [Remillard & McClintock 2006](#) for a review).

Broadly, the most prominent spectral states are high/soft, low/hard, and very high state. The thermal emission-dominated spectra with higher luminosity belong to the high/soft or thermal state. In this case, the spectra are dominated mainly by the multi-color blackbody emission from accretion disks. The hard powerlaw dominated ($1.4 < \Gamma < 2.1$) low luminosity state is known as low/hard or simply hard state. The hard state in black hole XRBs is mainly understood to be associated with a quasi-steady radio jet. In XRBs, a significant fraction of radio spectra are often detected, which are generated via jet synchrotron emission. In fact, the non-thermal emission in these systems is associated with Compton up-scattering in the corona or synchrotron emission from the jet. Another state that is in a relatively higher luminosity regime with spectra being comprised of both thermal and softer powerlaw ($\Gamma > 2.4$) components is known as a very high state or steep power law state ([Remillard & McClintock 2006](#)).

These different states broadly exhibit some interesting timing characteristics ([Homan & Belloni 2005](#); [Homan et al. 2001](#)). The low state power spectrum

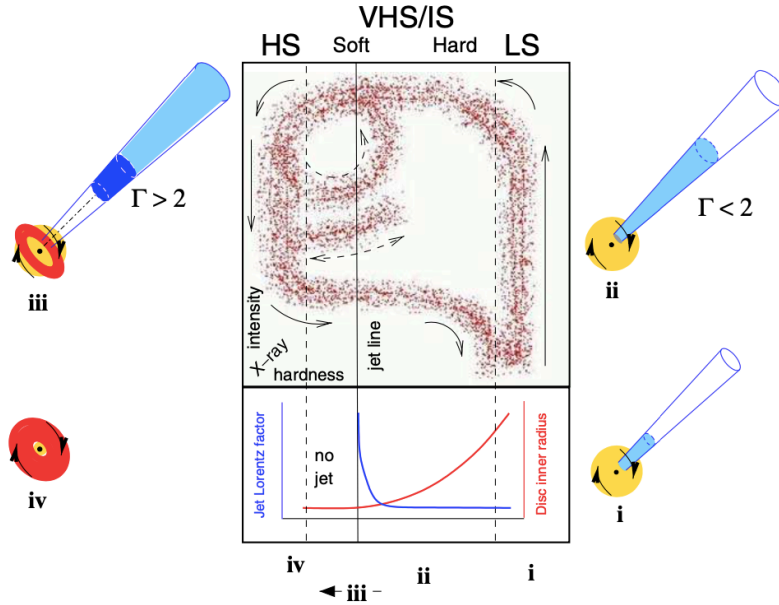


Figure 1.1: Different spectral states of sub-Eddington black hole XRBs are shown in a schematic diagram via a jet-disk coupling model taken from figure 7 of [Fender et al. \(2004\)](#). The upper central panel shows the hardness-intensity (HID) diagram, where hardness (ratio between count rates of hard and soft photons) increases to the right and intensity increases upwards. The lower panel shows how the bulk Lorentz factor of the outflow depends on the hardness. The sketches outside describe the picture of contributions from the jet (blue), corona (yellow), and accretion disk (red). The spectral state denoted as HS is the high/soft state, VHS/IS is the very high/intermediate state, and LS is the low/hard state.

exhibits strong band-limited noise with typically $\sim 20\text{--}50\%$ rms and a break frequency below 1 Hz. The intermediate/very high state typically shows weaker noise $\sim 1\text{--}20\%$ rms, break frequency around 1–10 Hz. Quasi-periodic oscillations (QPOs) are observed in this intermediate/very high state in between 1 and 10 Hz. In the case of high state, the noise is very weak, less than $\sim 2\text{--}3\%$ rms.

Figure 1.1 (taken from [Fender et al. 2004](#)) shows different spectral states and transitions between these states for the active phase of black hole binary systems. Typically, for an outburst, the XRB starts from a corona dominated quiescent state (i) and progresses to a low/hard state (ii) with increasing luminosity

and a steady jet. At some point in the very high state, the bulk Lorentz factor increases rapidly and produces internal shock in the outflow (iii), eventually ceasing the jet production, which leads to the disk-dominated high/soft state (iv).

1.3 | Ultraluminous X-ray sources

Ultraluminous X-ray sources (ULXs) are non-nuclear point sources that have apparent isotropic X-ray luminosity (in 0.3–10.0 keV energy band) more than $10^{39} \text{ erg s}^{-1}$ (see [Feng & Soria 2011](#); [Kaaret et al. 2017](#); [King et al. 2023](#) for detail reviews). This luminosity limit is broadly defined, corresponding to the Eddington luminosity of a $10M_{\odot}$ black hole. That means if ULXs are sub-Eddington accretors, their mass would be more than $10M_{\odot}$. Since the ULXs are far from the location of the galactic centers, they are not SMBHs. Nevertheless, one possible explanation is that the mass of the central accretor could be $10^2M_{\odot} \lesssim M \lesssim 10^4M_{\odot}$, i.e., an intermediate-mass black hole (IMBH) ([Colbert & Mushotzky 1999](#)).

There are, however, some arguments that do not support the IMBH interpretation. The understanding regarding the formation of IMBHs is still unclear. Some models include rapidly merging stellar-mass black holes (StMBHs) in globular clusters or stars in dense clusters. However, forming a binary system with an IMBH host would require a companion star with a sustainable mass transfer rate (see [King et al. 2023](#) and references therein), which needs to be better understood. Some sources have luminosity $L_x > 10^{41} \text{ erg s}^{-1}$ and are known as hyperluminous X-ray sources (HLXs). These sources are still considered the best IMBH candidates ([Brightman et al. 2016](#); [Kaaret et al. 2017](#); [Webb et al. 2010](#)). There are two prominent IMBH candidates, namely ESO 243-49 HLX-1 and M82 X-1 ([Kaaret et al. 2017](#)). [Sutton et al. \(2012\)](#) has studied some bright sources where the typical hard spectrum similar to the Galactic XRB sources indicates that their spectra are consistent with the hard spectral state. Their high luminosities suggest that the mass of these sources corresponds to IMBHs. Several studies of the spectra of ESO 243-49 HLX-1 ([Davis et al. 2011](#); [Godet et al. 2012](#);

(Straub et al. 2014) with different spectral models, which include fully relativistic thin disk and fully relativistic slim disk models, estimate the mass of the black hole at the core to be in the range of IMBH in all cases. Pasham et al. (2014) detected twin-peak high-frequency QPOs with a 3:2 frequency ratio in M82 X-1, which constrained the central black hole mass to be $428 \pm 105 M_{\odot}$. Although there are possible IMBH candidates in ULX and HLX systems, more recent observational evidence suggests that ULX spectral properties are quite different from the standard spectral properties of sub-Eddington XRBs (Gladstone et al. 2009; Sutton et al. 2013). Hence, most of the ULX spectral states are not related to the low state of IMBH spectra.

Two distinct spectral features of ULXs are the presence of soft-excess $\lesssim 2$ keV and spectral break in the high energies like ~ 6 – 10 keV. The consensus for explaining these features distinguishing from XRBs is that ULXs do not undergo the sub-Eddington accretion process. They are possibly super-Eddington accreting systems with stellar-mass hosts at the cores. These high luminosities in ULXs can be explained by super-Eddington accretion (Begelman 2002) or highly relativistic beaming (Körding et al. 2002) from stellar-mass accretors. In neutron stars, due to high magnetic field $\geq 10^{12}$ – 10^{13} G, the electron scattering cross-section can get reduced (Canuto et al. 1971), which in turn, would increase the maximum limit of the luminosity. However, these models are limited to the luminosity range up to 3×10^{40} erg s $^{-1}$ (see, e.g., King et al. 2023). King et al. (2001) suggested that high geometric collimation (or geometric beaming) can cause such extreme apparent luminosity. If the true luminosity of a ULX is L and the geometric beaming factor is $b \ll 1$, then the apparent spherical luminosity would be,

$$L_{sph} = \frac{1}{b} L \gg L. \quad (1.7)$$

To summarize, if sub-Eddington accretion onto IMBHs is not feasible, then the high emitted luminosity in ULXs can be interpreted with several other scenarios based on super-Eddington accretion rate and beaming. Recent consensus is that mild beaming ($b \lesssim 1$) with an accretion rate close to or above the Eddington accretion rate (i.e., $\dot{m} \geq \dot{m}_{Edd}$) is the dominant reason for such high

luminosity in these sources (Feng & Soria 2011). If the central accretor is an StMBH with $M < 20M_{\odot}$ or a neutron star, then the accretion rate is required to be significantly above the Eddington accretion rate (i.e., $\dot{m} > \dot{m}_{Edd}$). Whereas, to generate the same luminosity, for a massive StMBH ($20M_{\odot} < M < 100M_{\odot}$), the accretion rate can be close to the Eddington rate (i.e., $\dot{m} \sim \dot{m}_{Edd}$).

1.3.1 | Super-Eddington accretion

Super-Eddington accretion happens when the accretion rate is higher than the Eddington rate. It is theoretically expected that when the accretion rate is high, the inner region of the accretion disk geometry is modified from the standard accretion disk or the well-known thin accretion disk (Shakura & Sunyaev 1973). In a standard thin accretion disk, the disk scale height is much smaller than the radius ($H \ll R$). However, when the accretion rate increases, the inner region takes a funnel-like structure and $H \sim R$ (Abramowicz et al. 1988; Dotan & Shaviv 2011; Sadowski 2011).

The vertical dynamical equilibrium in accretion disk gives the relation between scale height H , radius R , and the isothermal sound speed $c_s = \sqrt{P/\rho}$, where P and ρ are total pressure and density, respectively, combined from gas and radiation.

$$\frac{H}{R} \approx \frac{c_s}{v_k}, \quad (1.8)$$

where, $v_k = \sqrt{GM/R}$ is the Keplerian velocity (King et al. 2023; Lasota 2016; Shakura & Sunyaev 1973). This can be written as (King et al. 2023),

$$\frac{H}{R} \approx \frac{L(R)}{L_{Edd}}, \quad (1.9)$$

$L(R)$ is the local luminosity at radius R . If $L(R) \ll L_{Edd}$, and $H \ll R$, the accretion disk is the standard thin accretion disk. If $L(R) \sim L_{Edd}$, then the scale height approaches the scale of radius $H \sim R$, and essentially, when $L(R) > L_{Edd}$, $H > R$, the accretion disk takes more of a spherical form rather than a disk.

There are some characteristic radii of the accretion disk in the super-Eddington regime. When the local luminosity exceeds the Eddington limit, the thin accre-

tion disk geometry starts to get modified to a puffed-up geometry and becomes a more spherical-like inner accretion flow. This characteristic radius is the “spherization radius” (R_{sph}). [Shakura & Sunyaev \(1973\)](#) showed that R_{sph} depends on the Eddington ratio $\dot{m}_0 = \dot{m} / \dot{m}_{Edd}$ as,

$$R_{sph} \simeq \frac{27}{4} \dot{m}_0 R_s, \quad (1.10)$$

where $R_s = 2GM/c^2$ is the Schwarzschild radius of a gravitating body (see also [Begelman et al. 2006](#); [King 2009](#)).

The photon diffusion or escape time scale is given by $H\tau/c$, where τ is the optical depth. The viscous infall time is R/v_r , where v_r is the radial velocity. Inside a certain radius, where the diffusion time scale equals the viscous infall time, the photons are trapped and advected faster than the escape time scale. This radius is known as the trapping radius ([Lasota 2016](#)),

$$R_{trapp} = \frac{H}{R} \frac{\dot{m}_0}{\eta} R_s. \quad (1.11)$$

This accretion flow, where photons are trapped inside the R_{trapp} , is called the advection-dominated accretion flow. Another model discussed by [Shakura & Sunyaev \(1973\)](#) is that inside the R_{sph} , the accretion flow is such that the local flux is equal to its Eddington value at all radii. For the black body accretion disk, the luminosity (or flux) is equal to the σT_{eff}^4 , where T_{eff} is the effective temperature, and σ is the Stefan-Boltzmann constant. The total luminosity from the disk is essentially the sum of luminosities from regions inside and outside of R_{sph} (see, e.g., [King et al. 2023](#)).

$$\begin{aligned} L_{total} &= L_{thin} + L_{thick} \\ &= 4\pi \left(\int_{R_{in}}^{R_{sph}} \sigma T_{eff}^4 R dR + \int_{R_{sph}}^{R_{\infty}} \sigma T_{eff}^4 R dR \right) \\ &\approx L_{Edd} (1 + \ln \dot{m}_0) \end{aligned} \quad (1.12)$$

This is known as the “windy” solution. Here, the accretion rate decreases with radius to preserve the radiation flux consistent with its Eddington value.

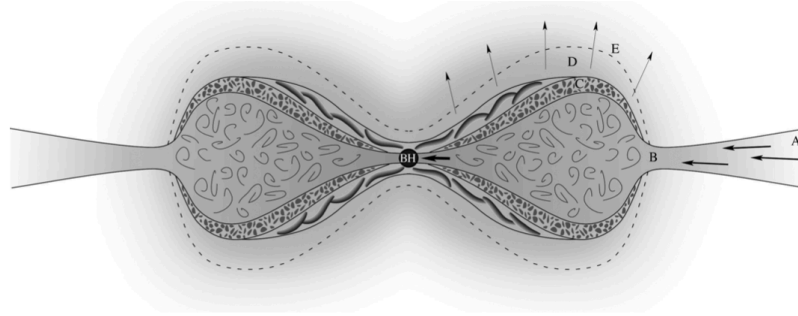


Figure 1.2: The super-Eddington slim accretion disk schematic diagram taken from figure 1 of [Dotan & Shaviv \(2011\)](#) shows different regions of the accretion disk, including wind. The different regions are depicted as e.g., (A) the sub-Eddington thin accretion disk, (B) the disk becomes radiation-pressure dominated, the energy release becomes correlated to the Eddington limit, and the disk begins to inflate, (C) Above the convection layer, a porous layer is generated, (D) wind is accelerated from the region where the porous structure is optically thin, (E) the photosphere located within the wind.

The excess energy generated due to the high accretion rate can be released via the launch of outflowing wind within the spherization radius ([Poutanen et al. 2007](#)).

Another model that depends on the advection-dominated accretion flow is often considered when discussing the radiative mechanism in ULXs, the “slim disk” model. The advective flow with a high accretion rate, where $H \sim R$, is known as the “slim disk” ([Abramowicz et al. 1988](#); [Sadowski 2011](#)). A characteristic radius in this scenario is where the transition between radiative and advective cooling occurs. This is the transition radius (R_{trans}). Interestingly, the total luminosity from slim disk geometry would be similar to the “windy” solution luminosity explained above, where the slim disk luminosity would be calculated with the region between R_{in} and R_{trans} .

Hence, the total disk luminosity would be,

$$L_{total} = L_{thin} + L_{slim} \approx L_{Edd}(1 + \ln \dot{m}_0). \quad (1.13)$$

In the slim disk scenario, inside the trapping radius, the disk is advection dominated, i.e., photon diffusion time from the disk interior to the surface is higher than the accretion time. As a consequence of this change in disk ge-

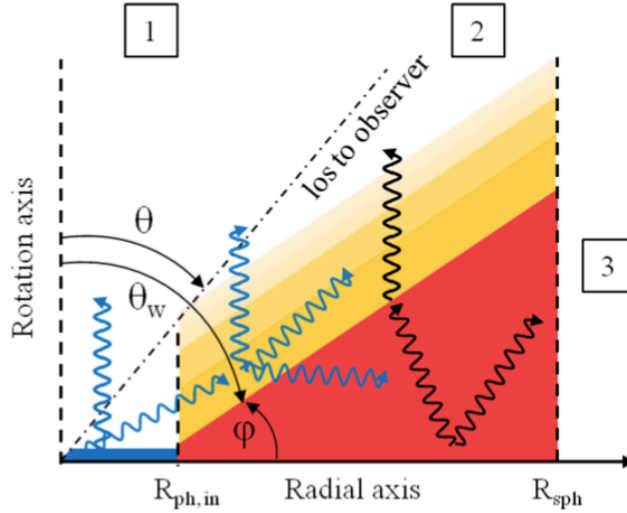


Figure 1.3: Schematic representation of the super-critical accretion scenario with the outflowing wind into consideration (taken from figure 1 of [Middleton et al. 2015a](#)). The inclination of line of sight of the observer is θ , wind cone opening angle is θ_w . When θ is small (position 1), the maximum unobscured emission from the hot inner disk is observed. With moderate θ , a significant fraction of hard X-ray flux will be scattered out of the line of sight due to wind (position 2), and with very high θ (position 3), the outer photosphere of the wind will dominate the emission, which would be dominant in UV and mostly out of the X-ray bandpass.

ometry, the temperature profile of the disk also changes. For a thin disk $T(R) \propto R^{-3/4}$, whereas, for a slim disk it is $T(R) \propto R^{-1/2}$. In figure 1.2 taken from [Dotan & Shaviv 2011](#), a schematic diagram of the “slim disk” is represented where an apparent change in the accretion disk geometry due to super-Eddington accretion rate can be observed.

There is another advection-dominated model where $H \gg R$, where most of the radiation is emitted through a long central funnel. This is known as the Polish doughnuts (e.g., [Abramowicz et al. 1978](#); [King et al. 2023](#); [Kozłowski et al. 1978](#)).

In both “windy” solution and advection-dominated solutions, the $L \approx L_{Edd}(1 + \ln \dot{m}_0)$ relation remains valid, and thus, it is an appropriate approximation for the unbeamed intrinsic luminosity of ULXs. If a beaming factor b is introduced,

then the apparent luminosity would be,

$$L_{app} = \frac{1}{b} L_{Edd} (1 + \ln \dot{m}_0) \quad (1.14)$$

In recent studies, there has been a detailed exploration of possible accretion geometries in ULXs. [Middleton et al. \(2015a\)](#) has described three different zones (see figure 1.3) for the geometry of super-critical accreting disk. In the region inside the inner photospheric radius ($R_{ph,in}$), the emission appears as a distorted hot disk as the wind is transparent ($\tau \leq 1$). In the second zone between the $R_{ph,in}$ and R_{sph} , the disk is advection-dominated due to the accretion rate being above \dot{m}_{Edd} and the wind is optically thick $\tau > 1$. The third zone is at a radius greater than R_{sph} , where optical depth τ of the wind decreases with increasing radius and quasi-thermal blackbody emission is generated.

1.3.2 | ULX spectra and different states

Modern X-ray observatories like XMM-Newton, Chandra, and NuSTAR provide high signal-to-noise ratio (S/N) spectra from ULXs, which help constrain the spectral properties with high precision. Typical continuum signatures include soft-excess $\lesssim 2$ keV and high energy spectral curvature ~ 6 –10 keV ([Gladstone et al. 2009](#); [Sutton et al. 2013](#)). Advection-dominated disk with outflowing wind scenario due to super-Eddington accretion ([Poutanen et al. 2007](#); [Shakura & Sunyaev 1973](#)) can broadly justify some of these properties. The spectra of ULXs are significantly different from those of sub-Eddington XRBs or AGNs, especially compared to the hard sources. More interestingly, there are dissimilarities between the spectral properties of different ULXs, which leads to the classification of ULX spectral states.

The key contributing factor while classifying the spectral states of ULXs is the spectral hardness and phenomenologically the relative contribution of spectral components (see [Kaaret et al. 2017](#); [Sutton et al. 2013](#)). When the spectra are dominated by thermal components from a geometrically modified accretion disk, the state is known as the “Broadened disk (BD)” state. Typically inner disk temperature of these sources is > 0.5 keV and disk contribution in

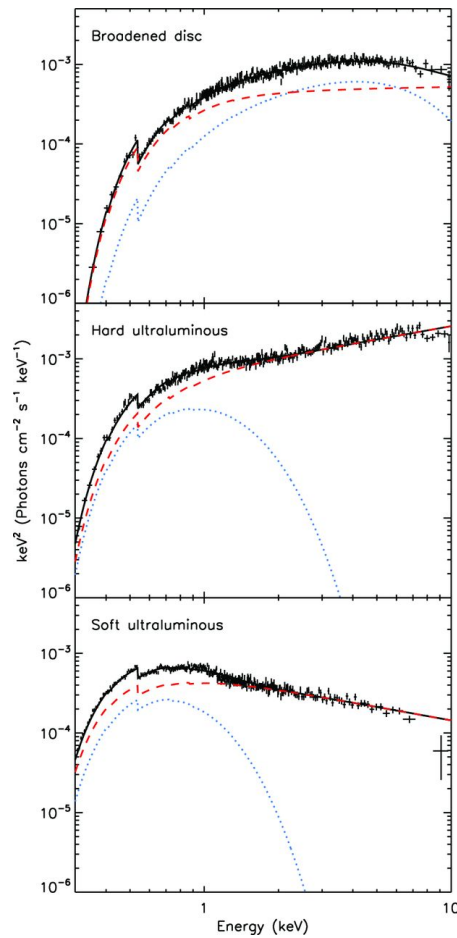


Figure 1.4: From figure 1 of [Sutton et al. 2013](#), three different spectral types in ULXs are shown.

the 0.3–1.0 keV spectra is much higher than the powerlaw component ([Sutton et al. 2013](#)). ULXs that show two-component spectra, i.e., a cool accretion disk and a powerlaw tail, in the 0.3–10.0 keV energy range, are classified as “Ultraluminous (UL)” state sources. Broadly, these UL state sources are further classified into two regimes, depending on the hardness of their spectra. These two classes are hard ultraluminous (HUL) or soft ultraluminous (SUL) regimes. For HUL sources, powerlaw index $\Gamma < 2$ and for SUL sources $\Gamma > 2$. In UL state sources, the relative contribution of flux from the powerlaw component in 0.3–1.0 keV energy is significantly higher than that of the disk component ([Sutton et al. 2013](#)). Figure 1.4 taken from [Sutton et al. \(2013\)](#) shows three dif-

ferent spectral types of ULXs. The literature has some correlated classifications of these HUL and SUL regimes. As defined in [Gúrpile et al. 2021a,b](#), they are identified as the hard intermediate and soft bright states, respectively. Typically, if the source luminosity is higher, the spectra from the source appear to be softer, thus named as soft bright states, and the comparatively lower luminosity sources exhibit harder spectra, i.e., the hard intermediate state. A possible physical reason for such a luminosity-hardness relation is that when the accretion rate is higher, more clumpy winds are generated, and the hot photons are down-scattered by the dense medium of the winds and become softer. A subclass of SUL sources is “supersoft ultraluminous” (SSUL) sources or “Ultraluminous supersoft sources” (ULSs). Spectra of SSUL sources are dominated by a single component cool blackbody emission ($T_{bb} < 0.14$ keV), and the most fraction of their flux are observed at energies < 1 keV ([Pinto et al. 2021](#); [Urquhart & Soria 2016](#)). Their bolometric luminosity is typically a few times 10^{39} erg s $^{-1}$. See figure 2 of [Kaaret et al. 2017](#) where different ULX spectral states are compared with spectra of Galactic black hole binaries.

It is crucial to understand that the distinctions between these classifications are not always rigid. Quite often, ULXs show the spectral transition between these different states or regimes (e.g., [D’Aì et al. 2021](#); [Gúrpile et al. 2021a,b](#); [Sutton et al. 2013](#); [Walton et al. 2020](#)). Several physical parameters like variation in accretion rate, accretion disk inclination angle with respect to the line of sight, the strength of the outflowing wind, and contribution from different radiative processes can cause such a spectral transition in different epochs of observation. The hardness of the sources depends on the mass outflow rate and the viewing angle of the disk. The softer sources are being observed close to the plane of the disk (e.g., [Middleton et al. 2015a,b](#); [Pinto et al. 2021](#)).

Modern observations with broadband X-ray coverage help constrain the different emission components of ULXs. The high S/N data for several ULXs show that two thermal components and an additional high-energy component best describe the broadband spectra. This additional high energy component is typically interpreted as Comptonization from the corona for non-magnetic sources or emission from the accretion column for highly magnetized neutron stars (e.g., [Walton et al. 2020](#); [West et al. 2018](#)). The two thermal components consist of a

soft/cool component and a hard disk component. They have different interpretations in different scenarios. For example, in a black hole system, the soft component can either come from the outer and cooler thin accretion disk or from the down-scattered photons from optically thick wind, and the hard component would come from the hot inner accretion flow due to super-Eddington accretion (e.g., [Luangtip et al. 2016](#); [Walton et al. 2014, 2015a](#)). It is considered that weakly magnetized neutron star ($B < 10^{11}$ G) would have a similar accretion scenario like the black hole systems ([King & Lasota 2016](#)). The thin accretion disk can extend up to the boundary layer of the neutron star, and the soft component comes from the disk, whereas the hard component comes from the optically thick plasma at the boundary layer ([Koliopanos et al. 2017](#); [Syunyaev & Shakura 1986](#)). Even when the magnetic field is high, due to extreme accretion and high luminosity ($L_x \gtrsim 5 \times 10^{39}$ erg s $^{-1}$), the material within the Alfvén radius becomes optically thick and can produce hard photons ([Koliopanos et al. 2017](#); [Mushtukov et al. 2017](#)). The cool thermal component comes from the accretion disk truncated at the magnetospheric radius (R_M). An alternative explanation of the cool thermal component is the optically thick wind generated down the R_{sph} .

1.3.3 | Wind and atomic features

A crucial feature as the consequence of super-critical inflow is the generation of outflowing wind. [Qiu & Feng \(2021\)](#) studied a sample of ULX sources, including black holes and pulsating ULXs, and argued that most sources show constant soft black body luminosity, a manifestation of this optically thick wind. In neutron stars, the thermal blackbody luminosity from wind exceeding the Eddington limit can possibly be related to the reduced scattering cross-section in a high magnetic field scenario or boosted radiation owing to the magnetic buoyancy ([Qiu & Feng 2021](#)). The ionized plasma in the wind clouds is the source of atomic lines, often detected by high-resolution grating instruments. Broad residuals between 0.5–2.0 keV are detected in several ULXs by CCD detectors from different observatories like XMM-Newton and Chandra ([Middleton et al. 2015b](#); [Stobbart et al. 2006](#)). This broad feature is associated with the forest of emission

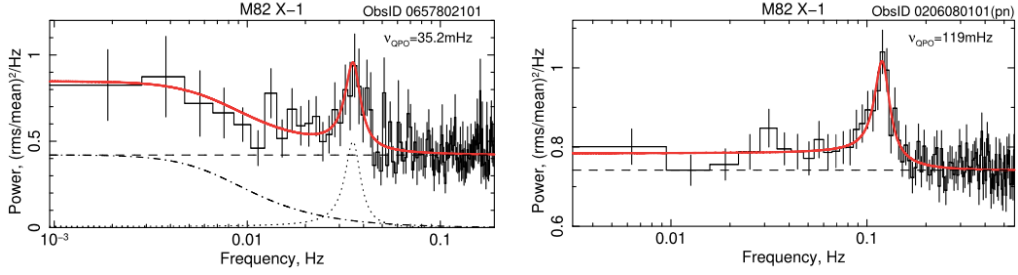


Figure 1.5: An example figure of Quasi-periodic oscillation discovered in ULX. Image is taken from figure 1 of [Atapin et al. \(2019\)](#).

and absorption lines concentrated around ~ 1 keV. These lines have been confirmed in several sources by XMM-Newton RGS instruments e.g., NGC 55 ULX, NGC 247 ULX-1, NGC 1313 X-1, NGC 5408 X-1, NGC 300 X-1, Ho IX X-1, Ho II X-1 (see, e.g., [Kosec et al. 2018a,b, 2021](#); [Pinto et al. 2016, 2017, 2020, 2021](#)).

The lines are mostly blue-shifted absorption lines and rest-frame emission lines ([Pinto et al. 2016, 2017](#)) or, in some cases, blue-shifted emission lines ([Kosec et al. 2018a](#)). The outflowing velocity estimated for these winds can be as high as $> 0.2c$, which is consistent with the expected velocity from radiatively driven winds in super-critical accretion scenario (see [King et al. 2023](#) and references therein). The kinetic luminosity of the wind is estimated as,

$$P_{wind} = \frac{1}{2} \dot{m}_{wind} v_{wind}^2 = 2\pi L_{ion} \frac{\Omega}{\zeta} v_{wind}^3 m_p, \quad (1.15)$$

where \dot{m}_{wind} is the wind outflow rate, v_{wind} is the velocity of the wind, Ω is the solid angle, L_{ion} is the ionizing luminosity, ζ is the ionization parameter. Some ionized elements observed in ULXs are Mg XII, Ne X, Ne IX, Fe XVI, Fe XVII, Fe XVIII, O VII, O VIII, N VII ([Pinto et al. 2016](#)). Some studies (e.g., [Middleton et al. 2015b](#)) have found that these wind features weaken when the source exhibits a harder spectral state. This could be related to the changing optical depth of the wind along our line of sight because of the wind precession or a change in the accretion rate in the system. In fact, the higher disk inclination of the ULX is a possible reason for these wind features being detected predominantly in softer sources, with hotter inner regions being shrouded from the line of sight.

1.3.4 | Timing properties of ULX

The variation of photon count rate with time (the light curve) is an essential aspect of study in ULX science to understand the temporal variability in the sources. This variability can happen in a broad range of duration, i.e., from very short (in order of seconds) to large (in order of days or months) time scale.

A straightforward study is to perform a Fast Fourier Transform (FFT) of the light curve and analyze their periodogram or power spectral density (PSD). There are individual ULXs whose PSDs have shown red-noise or broken power law (Atapin et al. 2019; Dewangan et al. 2006; Heil et al. 2009; Strohmayer & Mushotzky 2003; Strohmayer et al. 2007). Often, it is understood that fluctuation in accretion rate can give rise to such red noise in the power spectrum. Light curve variation is also measured with a quantity called fractional rms variability (Uttley & McHardy 2001; Vaughan et al. 2003). This measures the variance of the source light curve over the Poissionian noise normalized to the average count rate.

Some ULXs have shown significant variability ($\sim 30\%$ fractional rms; Middleton et al. 2015a), whereas many ULX sources have shown very low variability (Heil et al. 2009). Physically, it is possible that the intrinsic variability originating in accretion inflow can be weakened due to photon scattering inside the neutron star accretion column or by significant mass loss by the wind (Middleton et al. 2015a; Mushtukov et al. 2019). However, in soft sources like NGC 5408 X-1 or NGC 6946 X-1, linear rms-flux relations have been found (Hernández-García et al. 2015), thus suggesting significant variability. This can arise from the stochastic process of accretion flow being obscured by the clumpy wind generated due to the super-Eddington accretion process (Middleton et al. 2011; Sutton et al. 2013). In fact, Sutton et al. (2013) showed that high levels of fractional variability are more common in SUL or some BD ULX sources compared to the HUL sources.

Some ULXs have been discovered to exhibit QPOs on top of the noise in the power spectrum, like NGC 5408 X-1, NGC 6946 X-1, NGC 1313 X-1, M82 X-1, IC 342 X-1 (Agrawal & Nandi 2015; Atapin et al. 2019; Pasham et al. 2015; Pasham & Strohmayer 2012; Rao et al. 2010; Strohmayer & Mushotzky 2003,

2009). The origin of QPOs is not very well understood, but they can potentially come from accretion rate modulation or precession of accretion disk (King et al. 2023). See figure 1.5 as an example of QPOs in one ULX source (M82 X-1) taken from Atapin et al. (2019).

The discovery of pulsation in M82 X-2 (Bachetti et al. 2014) has changed the field of ULX science. It has confirmed the presence of a neutron star at the core of the ULX binary system. After this discovery, a few extragalactic ULX sources like NGC 5907 ULX1, NGC 7793 P13, NGC 300 ULX-1, NGC 1313 X-2, M51 ULX-7 have been confirmed to show pulsation (Carpano et al. 2018; Fürst et al. 2016; Israel et al. 2017a,b; Rodríguez Castillo et al. 2020; Sathyaprakash et al. 2019). Detection of pulsation in ULX requires advanced timing techniques like acceleration or jerk pulsation search (e.g., Andersen & Ransom 2018; Ransom et al. 2002). The discovered pulsing ULXs have a pulse period in the range of $\sim 1\text{--}30$ s. Few ULXs have been confirmed to show spin-down/up similar to Galactic pulsar binary systems (e.g., Bachetti et al. 2020; Israel et al. 2017a). In several cases, it is also seen that the pulsed fraction increases with increasing photon energy.

In figure 1.6, taken from Israel et al. 2017b, the detection of pulsation in the NGC 7793 P13 source is shown. In recent studies, searching for pulsation using the acceleration or jerk search technique has become a standard procedure to correct the Doppler smearing effect in individual ULX sources. See figure 1 of Israel et al. 2017a, where the pulsation in NGC 5907 ULX1 is found to be stronger after correcting the photon-arrival time for the derivative of the period (\dot{P}) term. However, not many ULX sources have shown such detection of pulsation. One reason could be the absence of enough count statistics in the data. Another physical reason could be that the pulsed emissions are prevented from being observed by other spectral components or due to unfavorable viewing angles and the presence of outflowing wind. It is also understood that the neutron star would not appear as a pulsar if the $R_M \ll R_{sph}$. In other words, the pulsed fraction would be stronger if $R_M \sim R_{sph}$, thus generating a high spin-up rate in the system (e.g., King & Lasota 2016; Walton et al. 2018a). Apart from these short-timescale variabilities in ULXs, some sources have shown periodicity in much longer timescales. Those are mostly related to orbital or super-orbital pe-

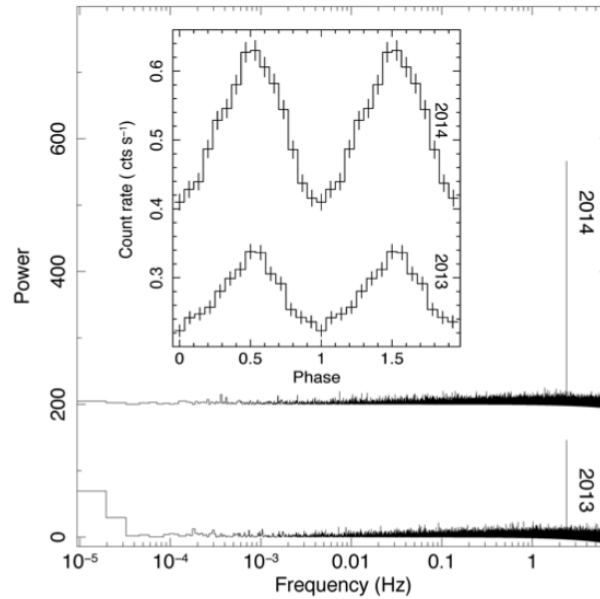


Figure 1.6: Detection of pulsation in the Fourier power spectra of NGC 7793 P13 light curves. The inset in the figure exhibits the folded profiles. Image is taken from figure 1 of [Israel et al. \(2017b\)](#).

riods (e.g., [Brightman et al. 2019](#); [Fürst et al. 2018](#); [Kaaret et al. 2006](#); [Vasilopoulos et al. 2021](#)).

1.4 | Radiative processes in ULX

Radiative processes in ULXs and XRBs, primarily responsible for the continuum emission, can be broadly divided into two types, e.g., thermal and non-thermal emissions. The primary source of the thermal-like emission in ULXs can be the accretion disk, wind, or boundary layer emission from the neutron star. Non-thermal emissions like synchrotron radiation or Compton scattering often contribute to hard energy spectra for binary systems or AGNs. Phenomenologically, the non-thermal emissions are approximated with the powerlaw spectrum.

1.4.1 | Thermal emission

Thermal processes are characterized as emission processes in thermal equilibrium. That signifies a characteristic temperature in the process, manifesting the radiated spectrum.

1.4.1.1 | Blackbody radiation

Blackbody radiation is the radiation from material in thermal equilibrium, which is optically thick (Rybicki & Lightman 1979). The spectrum is the Planckian function,

$$B_\nu(T) = \frac{2h\nu^3}{c^2} \frac{1}{\exp(\frac{h\nu}{k_B T}) - 1}, \quad (1.16)$$

where ν is the frequency of radiation, k_B is Boltzmann's constant, h is the Planck's constant, T is the blackbody temperature.

1.4.1.2 | Thin accretion disk

In X-ray binaries and ULXs, the major contribution of X-rays can come from the accretion disks. The standard thin accretion disk (Shakura & Sunyaev 1973) spectrum is essentially a sum of black body radiation with different peak temperatures, i.e., the multi-color disk (MCD). It is important to note that the geometrically thin and optically thick accretion disk is created for the sub-Eddington accretion process. In such a disk, the energy radiated within R and $R - \Delta R$ is $4\pi R \Delta R \sigma T^4$, where σ is the Stefan-Boltzmann constant. This energy equals the energy released for disk matter to fall within this distance of ΔR . Thus, the released energy is proportional to $R^{-2} \Delta R$. Hence,

$$T(R) \propto R^{-3/4}. \quad (1.17)$$

The observed flux spectrum from the thin accretion disk is given by (Makishima et al. 1986; Mitsuda et al. 1984),

$$f(E) = \frac{\cos \theta}{D^2} \int_{R_{in}}^{R_{out}} 2\pi R B(E, T) dR, \quad (1.18)$$

where, $B(E, T)$ is the Planckian distribution, R_{in} and R_{out} are the inner and outer boundaries of the disk, D is the distance to the source, and θ is the disk inclination with the line of sight. If we use Eq. 1.17 in Eq. 1.18, then we get,

$$f(E) = \frac{8\pi R_{in}^2 \cos \theta}{3D^2} \int_{T_{out}}^{T_{in}} \left(\frac{T}{T_{in}}\right)^{-11/3} B(E, T) \frac{dT}{T_{in}} \quad (1.19)$$

where, T_{in} and T_{out} are the inner and outer temperature of the disk. The total luminosity of the disk is related as $L = 4\pi R_{in}^2 \sigma T_{in}^4$.

1.4.1.3 | Super-Eddington accretion disk

The accretion disks in the super-Eddington accretion process geometrically differ from the thin accretion disk and become broadened accretion disks. The radial dependent temperature profile in the broadened accretion disk is,

$$T(R) \propto R^{-p}, \quad (1.20)$$

where, $p = 3/4$ is the thin accretion disk limit, and $p = 1/2$ is the slim accretion disk limit. Such an accretion disk is often called the “ p ” free multi-color disk.

The observed flux spectrum from the “ p ” free MCD is (Hirano et al. 1995; Mineshige et al. 1994; Watarai et al. 2000),

$$f(E) = \frac{2\pi R_{in}^2 \cos \theta}{pD^2} \int_{T_{out}}^{T_{in}} \left(\frac{T}{T_{in}}\right)^{-2/p} B(E, T) \frac{dT}{T} \quad (1.21)$$

Figure 1.7 shows the spectrum for different values of p ranging from 0.5 to 0.75 but for fixed temperature and normalization (i.e., fixed inner radius, disk inclination, and distance). We notice that for a smaller p value (e.g., slim disk), the spectrum has a more enhanced soft energy band compared to a standard thin disk.

1.4.1.4 | Bremsstrahlung radiation

Bremsstrahlung is the free-free emission due to accelerated charged particles in the presence of an electric field of another high energetic particle (Longair 2011;

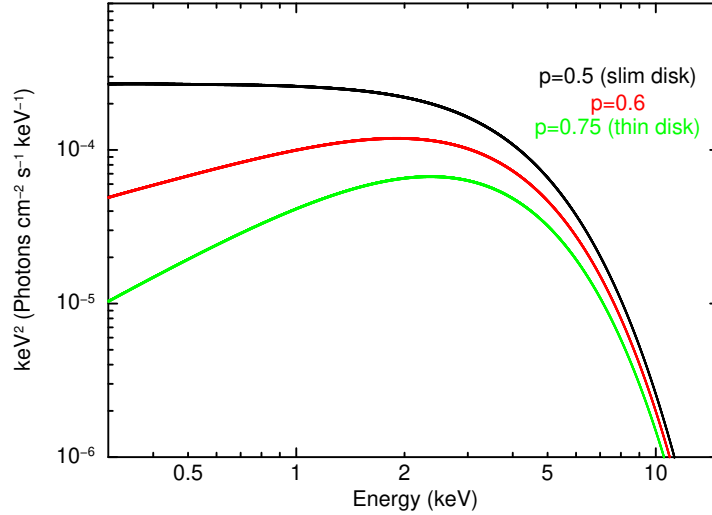


Figure 1.7: The model spectra of “ p ” free MCD emission shown for three values of p . The standard thin disk is for $p = 0.75$. While the p value decreases, the geometry of the inner region of the disk gets modified due to a higher accretion rate. In fact, it is seen that for a fixed temperature, a smaller p value gives a more enhanced soft energy band in the observed spectrum compared to the thin disk. The $p = 0.5$ limit is for a slim disk. The model spectra are plotted for fixed temperature and normalization using XSPEC (see Chapter 2) model `diskpbb`.

[Rybicki & Lightman 1979](#)). Electrons transitioning between unbound states manifest as continuous distribution known as the Bremsstrahlung spectrum. Bremsstrahlung can become an important emission mechanism in fainter spectral components (see [King et al. 2023](#); [Walton et al. 2015b](#)).

1.4.2 | Non-thermal emission

The emission in astrophysical sources, which does not depend on any characteristic temperature of the source, is non-thermal emission.

1.4.2.1 | Synchrotron radiation

Accelerated relativistic charged particles in the presence of a magnetic field radiate synchrotron radiation (Landau & Lifshitz 1975; Longair 2011; Rybicki & Lightman 1979). For an extremely relativistic particle ($\beta \approx 1$), the angle integrated synchrotron power per unit frequency from a single particle is given by (Rybicki & Lightman 1979),

$$P(\omega) = \frac{\sqrt{3}}{2\pi} \frac{q^3 B \sin \alpha}{mc^2} F\left(\frac{\omega}{\omega_c}\right), \quad (1.22)$$

where B is the magnetic field strength, q and m are the charge and mass of the particle, respectively, α is the pitch angle, ω is the emitted frequency, and $\omega_c = 3\gamma^2 q B \sin \alpha / 2mc$, γ is the relativistic boost.

1.4.2.2 | Cyclotron radiation

Cyclotron radiation has a similar emission mechanism to synchrotron, except the particle is non-relativistic, and the emission becomes discrete lines. In neutron star XRBs and ULXs, often cyclotron absorption lines are observed. These absorption features appear due to the resonant scattering of the photons by charged particles in the Landau orbits. The phenomena predominantly occur near the poles of the neutron stars in the presence of a high magnetic field. The discovery of the cyclotron line in M51 ULX-8 confirms the source as a neutron star, even though pulsation is not detected in its light curves (Brightman et al. 2018).

1.4.2.3 | Compton scattering

High-energy photons scattered by charged particles lose energy. This process is known as Compton scattering or Compton down-scattering. On the contrary, when a high-energy electron scatters a low-energy photon, and the scattered photon becomes highly energetic, the process is known as Inverse Compton scattering or Compton up-scattering. In many cases in XRBs and ULXs, the thermal disk photons work as the seed photons, which undergo an Inverse Compton scattering manifesting as a hard energy spectrum.

1.5 | Thesis outline

This thesis describes the study of some individual ULXs and their interesting X-ray spectral and timing properties. The primary motivation of this thesis is to explore different sources and find their new and unexplored physical characteristics. Also, it explains a new theoretical approach to describe the unique spectral curvature in ULX sources. In Chapter 1, we introduce the context of the study on ultraluminous X-ray sources and explain several aspects of X-ray emission mechanisms in X-ray binaries and ULXs. Chapter 2 discusses the X-ray observatories used for observing the sources and explains the primary data analysis methods. Chapter 3 reports the detection of the first X-ray flaring events observed in NGC 4395 ULX1. This chapter discusses detailed spectral and timing studies of the flaring events in the source, and the underlying physics is interpreted. Chapter 4 presents a comprehensive study of the highly luminous ULX source NGC 1042 ULX1 and its spectral variability using archival XMM-Newton data and the first hard X-ray data from NuSTAR observation. In Chapter 5, we discuss a novel theoretical model that explains the origin of spectral cutoff in ULX sources. Chapter 6 discusses the study of a sample of ULX sources, like NGC 6946 X-1, NGC 4190 ULX1, NGC 1291 ULX1, NGC 4254 X2, and NGC 4244 ULX1, using available X-ray data and compares their spectral properties which are found to have a common underlying mechanism of the super-Eddington accretion process. Finally, Chapter 7 summarizes the main context of the thesis and sets some future directions for the research in ULX science.

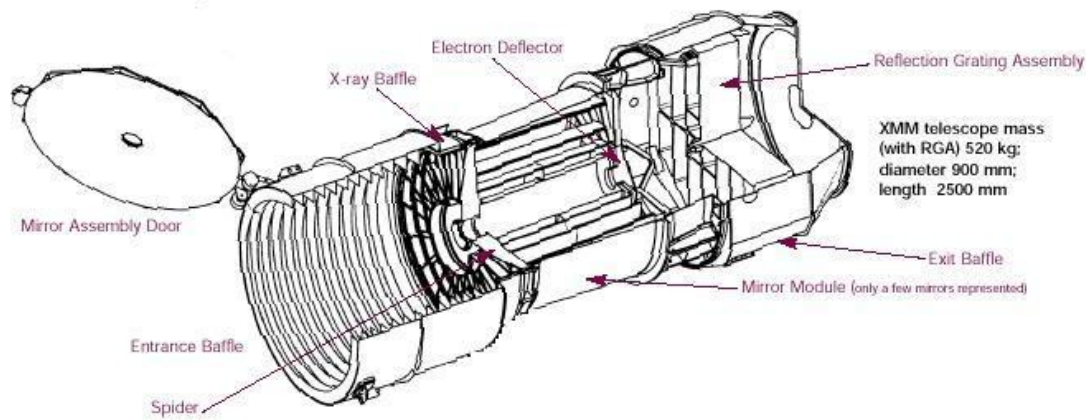
X-ray observatories and data analysis techniques

2.1 | X-ray observatories

X-rays cannot probe the Earth's atmosphere; hence, we need space-based observatories to detect X-rays from astrophysical sources. Here, we discuss the primary observatories from which we have utilized data for our work in this thesis. ULXs are predominantly extragalactic sources, and highly sensitive instruments are often essential to detect them. Observatories like XMM-Newton, Chandra, NuSTAR, Swift, and NICER are among the most used observatories to study ULX sources.

XMM-Newton (Jansen et al. 2001) is useful for its high sensitivity and effective area, good spectral resolution in grating instruments, and a well-calibrated full coverage of soft X-ray energy band in $\sim 0.3\text{--}10.0$ keV. NuSTAR (Harrison et al. 2013) becomes useful as a complimentary observatory since it has coverage in higher energy band $\sim 3.0\text{--}79.0$ keV. Hence, joint observations with XMM-Newton and NuSTAR become crucial in studying broadband X-ray properties of ULXs.

Often, ULXs are found in crowded regions in the sky. Hence, with its sub-arcsec spatial resolution, Chandra (Weisskopf et al. 2002) becomes helpful in separating nearby contaminating sources from the ULXs. Swift (Gehrels et al. 2004) and NICER (Gendreau et al. 2016) help monitor sources in a long-term



Technical drawing of one of the XMM-Newton telescopes

European Space Agency 

Credit: ESA/XMM-Newton, CC BY-SA 3.0 IGO

Figure 2.1: Artist impression of XMM-Newton observatory. Image credit - ESA/XMM-NEWTON (https://xmm-tools.cosmos.esa.int/external/xmm_science/gallery/images/Telescope.jpg).

interval. Hence, these two instruments are pivotal in detecting transient events in the sky and finding if these events are associated with ULXs.

Although we have utilized most of these observatories for the surveys of ULXs and analyzing their available data, the main results in this thesis are based on observations from XMM-Newton, NuSTAR, and partially from NICER. Hence, we will discuss the detailed properties of these three instruments in this chapter.

2.1.1 | XMM-Newton

X-ray Multi-Mirror Mission (XMM-Newton) is a European Space Agency (ESA) science mission with instruments and contributions directly funded by the ESA Member States and NASA. The mission was launched on December 10, 1999. There are three coaligned high throughput telescopes in the observatory. The primary focal plane instruments are two Reflection Grating Spectrometer (RGS) cameras and three imaging detectors (one pn and two MOS cameras) comprising the European Photon Imaging Camera (EPIC). These all are charge-coupled device (CCD) detectors.

The EPIC cameras have imaging capability with a field of view (FOV) of 30 arcmin. The typical spectral resolution of these cameras in $\sim 0.15\text{--}15.0$ keV energy range is $E/\Delta E \sim 20\text{--}50$, and angular resolution is ~ 6 arcsec full-width half maxima (FWHM) or ~ 15 arcsec half power diameter (HPD). The RGS cameras have high spectral resolution $\sim 150\text{--}800$ in $0.33\text{--}2.5$ keV energy range. The observatory also has an optical/UV telescope called Optical Monitor (OM). Figure 2.1 shows the XMM-Newton detector configuration.

The scientific reduction of XMM-Newton data is performed using the Science Analysis System (SAS)¹ software (Gabriel et al. 2004). To analyze the data, apart from the software, we utilize the Current Calibration Files (CCF). The science products are generated from the Observation Data Files (ODF). Primarily for EPIC data, tasks like `epproc` and `emproc` are used to reduce the scientific products of pn and MOS data, respectively. The data are cleaned from soft-proton and background flaring events using standard methods² and then the cleaned event files are utilized for further scientific analysis. The main tool to generate the spectra and lightcurves from the event files is `evselect`. In general, while generating the spectra and light curves, we use parameters like `PATTERN <= 4` for pn, which takes the single and double events, whereas, for MOS, we use the single, double, triple, and quadruple events by the parameter `PATTERN <= 12`. For timing analysis, we use the `barycen` tool to perform the barycentric correction. The `epiclccorr` task is used to subtract the background and obtain the cleaned source light curves. This `epiclccorr` task also corrects for the vignetting, bad pixels, chip gaps, point-spread function (PSF), and quantum efficiency in the data. `rmfgen` and `arfgen` tasks are used to generate the response matrix files (RMFs) and ancillary response files (ARFs), respectively. Standard filtering criteria with `#XMMEA_EP` flag for pn and `#XMMEA_EM` flag for MOS detectors are used. In all cases of pn spectral analysis, as recommended, the `FLAG==0` criteria have been used. `rgsproc` is used to create science products for RGS data.

Depending on the source nature, location of the source on the CCD chip, and observation telemetry factors, the analysis procedures slightly vary for different observations. In each chapter of the thesis, we have discussed relevant reduction

¹<https://www.cosmos.esa.int/web/xmm-newton/sas>

²<https://www.cosmos.esa.int/web/xmm-newton/sas-thread-epic-filterbackground>

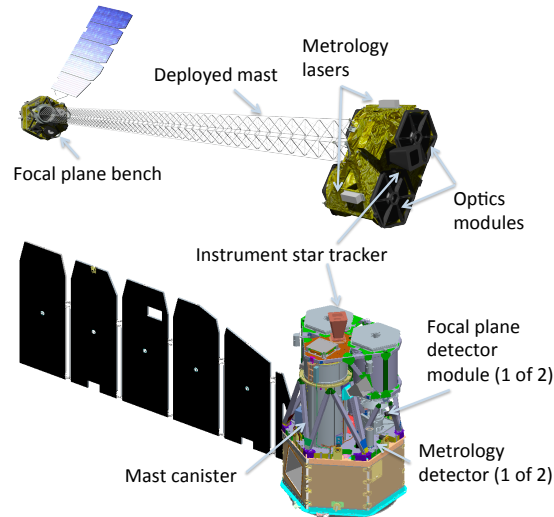


Figure 2.2: Diagram of NuSTAR observatory. The top is the deployed, and the bottom is the stowed configuration. Image credit - https://heasarc.gsfc.nasa.gov/Images/nustar/fig_observatory.pdf (see also figure 1 of Harrison et al. 2013).

and analysis procedures different from the general approach mentioned here.

2.1.2 | NuSTAR

The Nuclear Spectroscopic Telescope Array (NuSTAR) is the first X-ray imaging telescope in the high energy (3–79 keV) band of the electromagnetic spectrum (a project led by Caltech, funded by NASA, and managed by NASA Jet Propulsion Laboratory (JPL)). The observatory was launched on June 13, 2012, by NASA. Primary optics of NuSTAR mission is designed based on the conical approximation to the Wolter-I design. It consists of 133 mirror shells. There are two focal plane modules (FPMs): FPMA and FPMB. They are made up of Cadmium-Zinc-Telluride (CdZnTe) detectors. The energy resolution of the detectors is moderate, e.g., ~ 0.4 keV at 10 keV and ~ 0.9 keV at 68 keV. The angular resolution of

NuSTAR is 58" HPD or 18" FWHM. The temporal resolution is very high ($\sim 2\mu\text{s}$), and thus NuSTAR is useful for meaningful timing analysis of ULXs. NuSTAR detector played a vital role in discovering the first extragalactic ULX pulsar M82 X-2 (Bachetti et al. 2014).

The NuSTAR data analysis is done by HEASOFT (Nasa High Energy Astrophysics Science Archive Research Center (Heasarc) 2014) software³ `nustardas` package (jointly developed by the Space Science Data Centre (SSDC; Italy) and Caltech (USA)). Tools like `nupipeline` and `nuproducts` are used to generate clean, calibrated science products like spectra, light curves, images, and response files. The dynamically updated calibration files are also used while creating the science products. The `1cmath` tool is used for subtracting the background and obtaining the clean source light curves for both FPMs in NuSTAR data. In each chapter, we briefly note if there are any specific filtering criteria used for the NuSTAR data analysis. The detector configuration is shown in figure 2.2.

Figure 2.3 shows the effective areas of different X-ray detectors. In the soft energy regime, XMM-Newton is one of the instruments with a very high effective area, whereas NuSTAR plays a crucial role in the high energy band, which is not covered by any other X-ray imaging detector.

2.1.3 | NICER

Neutron Star Interior Composition Explorer (NICER) was launched on June 3, 2017. The payload is in the International Space Station (ISS), primarily focused on studying the timing properties of neutron stars in soft X-ray band (0.2–12.0 keV). The primary instrument in NICER consists of 56 X-ray concentrator optics and silicon drift detectors. NICER has a higher effective area compared to XMM-Newton. However, NICER is a non-imaging instrument with a 5 arcmin diameter of FOV; hence, analysis of ULXs within crowded regions is less sensitive. NICER is useful for well-isolated ULX sources with minimum contamination from nearby sources. The timing precision of the detector is < 300 ns. The spectral resolution $E/\Delta E$ varies between ~ 6 –80 in 0.5–8.0 keV energy range.

³<https://heasarc.gsfc.nasa.gov/docs/software/heasoft/>

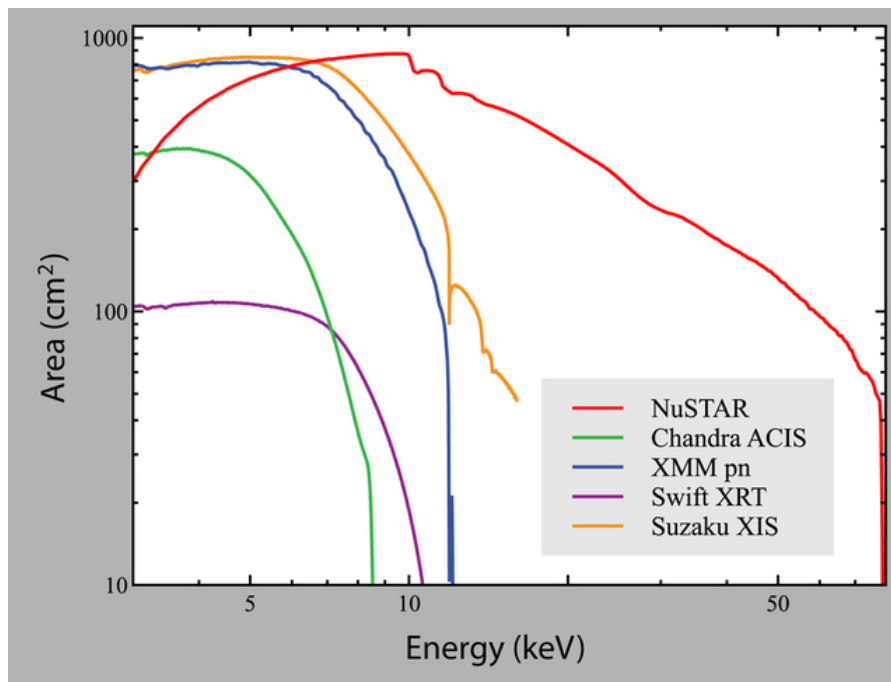


Figure 2.3: The comparison of effective areas of different X-ray telescopes. XMM-Newton and NuSTAR are active imaging observatories with high effective areas in the soft and hard energy bands, respectively. Image credit - <https://www.nustar.caltech.edu/page/researchers>.

2.2 | Data analysis techniques

The X-ray data analysis has four primary aspects: imaging analysis, timing analysis, spectral analysis, and polarimetric studies. The thesis primarily explores the first three avenues using modern X-ray observatories. Several packages like FTOOLS (Blackburn 1995; Blackburn et al. 1999), XRONOS, and XSPEC (Arnaud 1996) from HEASOFT have been used to analyze the light curves and spectra in most of the studies. Other packages like HENDRICS ⁴ (Bachetti 2018) and PRESTO ⁵ (Ransom 2011) have been used for accelerated search timing analysis. Sometimes, we have separately written codes ⁶ to analyze spectral and timing data, wherever required. The data from the observatories utilized in the thesis

⁴<https://hendrics.stingray.science/en/latest/>

⁵<https://github.com/scottransom/presto>

⁶<https://www.python.org>

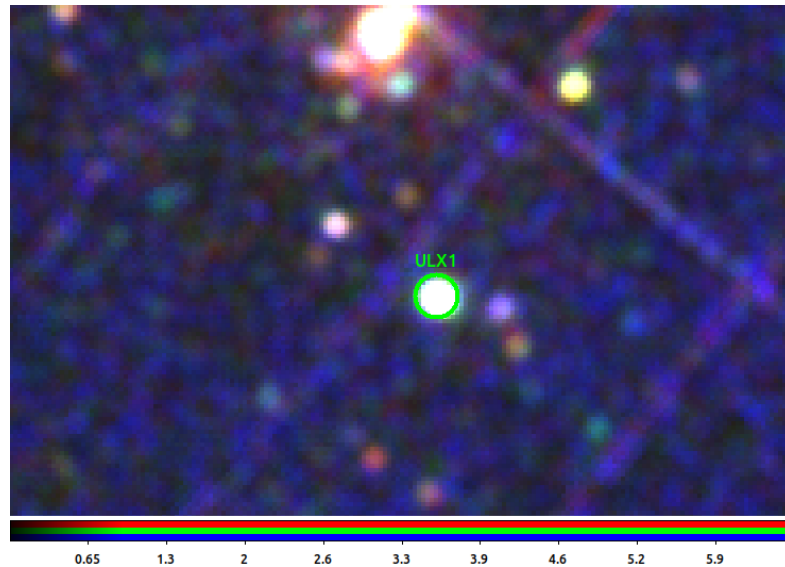


Figure 2.4: Example of an RGB image from XMM-Newton pn camera for NGC 1291 ULX1 studied in this thesis. The soft energy band (red image) is in 0.3–1.0 keV, the medium band (green image) is in 1.0–3.0 keV, and the hard energy band (blue image) is in 3.0–10.0 keV energy range. The image is smoothed with a Gaussian function for visual purposes.

are available or will be available after the proprietary right period (in case the data are obtained from our proposal) in the High Energy Astrophysics Science Archive Research Center (HEASARC) archive⁷.

2.2.1 | Imaging analysis

The images are created from the cleaned event files from the observations. A tool like ds9⁸ reads those images, which helps us localize the ULX and its coordinates. ds9 is also used to create true color images (RGB images) to identify images processed in different energy bands separately. For example, in figure 2.4, we show the RGB image of NGC 1291 ULX1 from XMM-Newton pn data.

⁷<https://heasarc.gsfc.nasa.gov/db-perl/W3Browse/w3browse.pl>

⁸<https://sites.google.com/cfa.harvard.edu/saoimageds9>

2.2.2 | Timing analysis

The primary timing analysis tool is `lcurve` from FTOOLS. `lcurve` reads the intensity vs. time from the events and produces binned lightcurves. This tool can easily calculate and plot the simultaneous energy time series, ratio, or sum of the multiple time series.

The basic tool to calculate the power spectrum density of the lightcurves is `powspec`. A fast FFT algorithm or a slow Fourier algorithm can compute the power spectrum. However, for ULXs, more advanced tools are required to perform a robust pulsation search, including tools like HENDRICS and PRESTO. In the case of pulsar binaries, detection of pulsation can be affected due to the orbital motion of the pulsar. If the duration of observation is longer than even a small fraction of the orbital period, the apparent pulsar spin frequency would vary with time due to Doppler shifting. In fact, the detection significance would be low in such cases since the Fourier signal will be smeared across the neighboring bins. Thus, a technique named Fourier Domain Acceleration Search technique (Dimoudi et al. 2018; Ransom et al. 2002) is utilized to detect pulsation. This acceleration search technique accounts for the Doppler smearing while searching for pulsation by assuming a constant acceleration over the observation time scale, which is a small fraction of the orbital period.

The HENDRICS (Bachetti 2018) is based on the `Stingray` software⁹ (Huppenkothen et al. 2019). The primary purpose of this tool in the study of ULXs is to utilize the accelerated search of pulsations in the time series data, which is implemented by tasks like `HENacclsearch` or `HENzsearch`. PRESTO (Ransom 2011) is another software that utilizes the acceleration search algorithm. On top of that, it has the capability to utilize the jerk search technique, which is advantageous compared to the other timing analysis tools. As in the acceleration search technique, a constant acceleration with linearly varying spin frequency is assumed; in jerk search, however, a constant jerk is assumed with linearly varying acceleration and quadratically varying spin frequency. This technique is available through the `acclsearch` program within PRESTO.

⁹<https://docs.stingray.science>

2.2.3 | Spectral analysis

The primary X-ray spectral fitting package XSPEC (Arnaud 1996) is used for analyzing the spectra of ULXs. The spectrometers capture the photon counts (C) within the instrument channel (I), which can be converted to the spectrum as follows:

$$C(I) = \int f(E)R(I, E)dE, \quad (2.1)$$

where, $R(I, E)$ is the instrumental response and the spectrum is $f(E)$. Finding the $f(E)$ from $C(I)$ by inverting the above equation is not possible due to the non-invertible nature of the response matrix. Thus, a “forward folding technique” is undertaken for spectral fitting. A model spectrum $f(E)$ is chosen, and for each $f(E)$, the count spectrum $C_p(I)$ is predicted. Then $C_p(I)$ is matched with the observed $C(I)$. A fit statistic is used for the comparison.

Usually, photon counts are in Poissonian distribution. However, the distribution can become Gaussian for a large sample of photon counts. This can be performed by grouping the spectrum with sufficient counts per bin. In the case of Gaussian distributed data, we can use χ^2 statistics to compare the data and the model. The fit statistic is then defined as:

$$\chi^2 = \sum_{i=1}^N \frac{(y_i - m_i)^2}{\sigma_i^2}, \quad (2.2)$$

where, m_i are the predicted model count rates, y_i are the observed data rates and σ_i are their errors. The best fit is found by minimizing the χ^2 statistics and ideally when the χ^2 value is similar to the degrees of freedom (ν), i.e., $\chi^2/\nu \sim 1$. This thesis mostly uses the χ^2 statistics for spectral analysis. If the data are not Gaussian and the distribution is Poissonian due to low count statistics, then instead of χ^2 , another statistic, known as Cash statistics (cstat; Cash 1979), is used.

Most of the works of this thesis are based on the fundamental structure of data analysis described in this chapter. Nevertheless, where any different procedures have been followed it is described in the respective chapters.

X-ray flaring in NGC 4395 ULX1

*This chapter is based on the results that appeared in the literature as
Hard X-Ray Flares and Spectral Variability in NGC 4395 ULX1, Ghosh
T., Rana V., Bachetti M., 2022, ApJ, 938, 76 (Ghosh et al. 2022); arXiv:2202.01432*

3.1 | Prologue

A large number of ULXs have been observed and studied in detail with modern X-ray observatories. However, only a handful of ULX sources have shown short-term timing variability in terms of fractional variability and quasi-periodic or periodic oscillation. In particular, transient incidents like strong X-ray flaring in ULXs are less common than in XRBs. Sources like NGC 1313 X-1 (Walton et al. 2020), NGC 247 ULX-1 (Pinto et al. 2021), NGC 4559 X7 (Pintore et al. 2021), NGC 7456 ULX-1 (Pintore et al. 2020), NGC 55 ULX (Barra et al. 2022; Pinto et al. 2017; Stobbart et al. 2004), M74 X-1 (Krauss et al. 2005), 4XMM J111816.0-324910 in NGC 3621 (Motta et al. 2020) are a few examples which have shown variability in their lightcurves like strong flaring, dips or slow heartbeat like features. Even in these sources, the transient incidents do not happen at regular intervals. Hence, detecting such flaring events in a ULX source is exciting since these flaring activities can help shed light on the dynamics of accretion processes in these sources.

Variability in ULXs, especially fractional variability in the lightcurves, are

Table 3.1: Details of 2018-2019 observations of NGC 4395 ULX1 discussed in this chapter. The exposure times noted here are flare-corrected approximate livetime CCD exposures for pn/MOS1/MOS2.

Serial No.	Observation ID	Date	Epoch ID	Cleaned Exposure (ksec)
1	0824610101	2018-12-13	XM1	71/89/94
2	0824610201	2018-12-19	XM2	48/67/69
3	0824610301	2018-12-31	XM3	50/66/70
4	0824610401	2019-01-02	XM4	77/97/100

predominantly found to be stronger in soft ULX sources (Sutton et al. 2013) compared to ULXs in other spectral states. The soft ULX sources generally exhibit powerlaw index $\Gamma > 2$ in 0.3–5.0 keV energy band (Pinto et al. 2021). Some sources, like NGC 55 ULX and NGC 247 ULX-1, exhibit soft spectra and fall somewhere between the ULX and ULS spectral states (See figure 1 of Pinto et al. 2017). Although their spectra are softer compared to many other soft ULX sources, unlike most ultraluminous supersoft sources, they show spectra extending up to ~ 5 keV. Typically, their spectra are best modeled by two black-body components (Pinto et al. 2017, 2020, 2021). Interestingly, both sources have shown variability in the form of flaring or dips in the lightcurves (Barra et al. 2022; Pinto et al. 2017, 2021; Stobbart et al. 2004).

NGC 4395 ULX1 (2XMM J122601.4+333131; Liu & Bregman 2005) is a soft ULX and has been known to exhibit a long-term variability (Kaaret & Feng 2009). Vinokurov et al. 2018 suggested that the source possibly exhibited a period of 62.8 days in archival observations. Nevertheless, the source has never shown significant short-term transient features in X-rays. Earnshaw & Roberts 2017 studied this source using previous XMM-Newton and Chandra observations. Those data also did not show any significant short-term timing variability like flaring incidents in this source. We have studied four high-quality XMM-Newton observations taken in 2018-2019. We detect flaring activities from this source for the first time in two of these observations.

3.2 | Observation details

The NGC 4395 galaxy contains a low luminous AGN, and XMM-Newton targeted the galactic center four times within three weeks of time scale between December 2018 and January 2019. The source ULX1 is around ~ 3 arcmin away from the AGN. Thus in all four observations, ULX1 was in the field of view of XMM-Newton detectors. In X-ray observations by XMM-Newton and Chandra, it is found that ULX1 is well isolated from any other nearby X-ray sources. Thus, the spectral and timing studies are clean from contamination from other X-ray sources. The main observations used for a detailed study of ULX1 in this chapter are noted in table 3.1.

The data reduction procedure for these observations is broadly based on the method outlined in Chapter 2. The source extraction region is a circle of 25 arcsec radius centered at $\alpha, \delta = 12 : 26 : 01.5, +33 : 31 : 31.0$, and the background extraction region is a circle of 50 arcsec radius in a nearby source-free region on the same chip. After removing the background flare-affected time intervals from the cleaned events, the final spectra and lightcurve products are produced.

Unfortunately, for all pn data, ULX1 falls near the chip gap. Additionally, strong bad column events in the source region have affected all pn observations. The most affected data are from the XM3 and XM4 epochs, where a significant fraction of the source region falls in the chip gap, and the bad column passes through the central region of the source. Such events have significant charge loss, and as a consequence, the pn spectra in these observations have a significant flux loss. In XM1 and XM2 observations, the bad column passes through the edge of the source region. Hence, these two epochs are comparatively less affected. Nevertheless, we have verified how significantly the chip gap and bad column issue in pn observations affected their spectra. We find that the spectral profile is unaffected except for a flux loss in XM3 and XM4 observations (see section 3.4 for details). Hence, simultaneous pn and MOS1/2 spectral fitting are performed with different models for further analysis.

The purpose of a robust timing analysis includes searching for fast-timing properties like pulsation or exploring the short-time variability. Hence, we used minimally filtered data for timing analysis to maximize the number of counts

and increase sensitivity for searching short-time variability features. Thus, light curves are created following the procedure described in Chapter 2 for XMM-Newton data reduction. Spectral analysis of the pn data is done with a strict filtering constraint of `FLAG==0` for all observations. This strict constraint minimizes the charge loss effect in the data affected due to bad column and chip gap. As a general procedure, all pn and MOS1/2 spectra are grouped using `specgroup` with a minimum 20 counts per energy bin and oversampling factor 3. In all observations, pileup in the data is evaluated with `epatplot`, and no significant pileup is found.

The RGS data for all four observations are extracted using standard procedure. However, we find that the RGS source spectra are significantly dominated by the background in all four observations, thus making them unreliable for any meaningful scientific analysis. In the full energy range for different epochs, the combined RGS1+RGS2 spectral count rate varies between ~ 0.007 – 0.016 counts/sec, whereas the cleaned exposure time is within the range between ~ 171 – 226 ksec.

3.3 | Timing Analysis

A sample of soft ULXs, including NGC 4395 ULX1, were studied in [Earnshaw & Roberts 2017](#) with archival X-ray observations. In those samples of sources, NGC 4395 ULX1 exhibited itself as the least variable source. During 2018-2019 XMM-Newton observations, the source exhibits both short-term (in the time scale of a few kilo seconds) and long-term (in the time scale of a few days) timing variability.

In figure 3.1, we plot the pn lightcurves for all epochs with a 2000 sec binning. An apparent visual inspection detects that in the XM1 and XM3 epochs, the source exhibits a relatively steady flux, while strong flare-like activity is detected in epochs XM2 and XM4. We also investigate the time series in two different energy bands to inspect any energy-dependent nature of the flaring events. The soft energy band of the light curves is set between 0.3 and 1 keV (figure 3.1 first panel), and the hard energy band is set above 1 keV (second panel). The

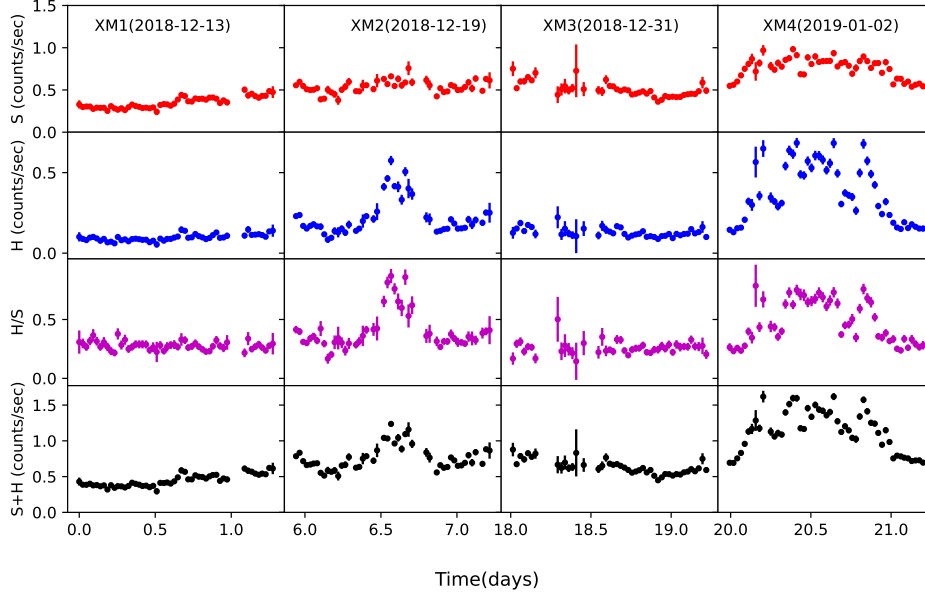


Figure 3.1: 2000 seconds binned XMM-Newton pn light curves of ULX1 for four individual epochs, namely XM1, XM2, XM3, and XM4. The soft (0.3–1.0 keV) and hard (1.0–8.0 keV) count rates are shown in the first and second panels, respectively. The hardness ratio, which is defined as the hard/soft photon count rate, is shown in the third panel. The fourth panel shows the sum of the soft and hard band lightcurves, i.e., the total lightcurve. A steady but slight uprising trend of the flux is observed in the first epoch (XM1). In the second epoch (XM2), a flaring episode occurred from around 30 ksec to 80 ksec of that observation. Another steady but slightly declining trend of flux is seen in the third epoch (XM3). Finally, in the fourth epoch (XM4), a large flaring episode happened, covering most portion (~ 80 ksec) of that observation. As seen in the hardness ratio plots, the prominent flares in XM2 and XM4 are predominant in the hard energy band.

background dominates above ~ 5 keV for XM1 and XM3 epochs, and for XM2 and XM4 epochs, the background only starts dominating above ~ 8 keV (see Section 3.4.1). However, it is essential to directly compare light curves from all four epochs. Hence, the hard energy band of the light curves is created between 1.0 and 8.0 keV for all four epochs. The third panel in figure 3.1 is the ratio of hard photon count rate to soft photon count rate, i.e., defined as the hardness

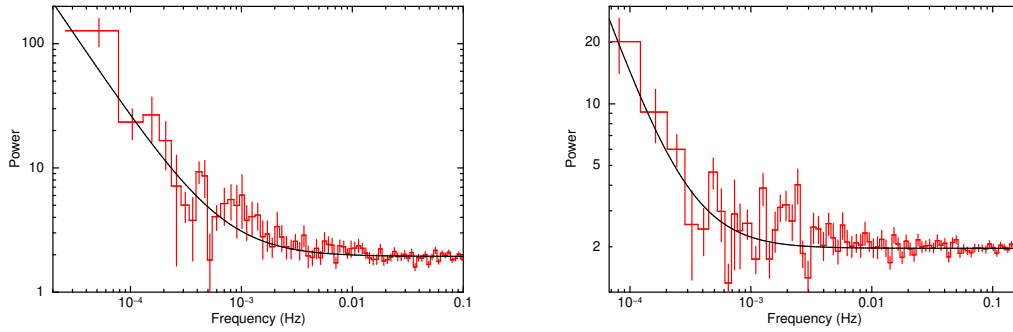


Figure 3.2: The example power spectral density plots for XM4 pn (left) and MOS2 (right) observations, respectively. This shows the presence of power law-shaped red noise in the power spectrum.

ratio. The fourth panel, on the other hand, shows the sum of soft and hard band photon count rates. It is apparent from the figure that the ULX1 count rate varies significantly between different epochs within only three weeks. The flaring incident in XM2 observation lasts around ~ 50 ksec, which is prominent primarily in the hard energy band of the light curves. The flaring detected during the XM4 epoch is the longest flaring episode among these observations, spanning around ~ 80 ksec, a large fraction of the total observation time scale of that epoch. In reality, the long flare of the XM4 epoch consists of multiple ephemeral sub-flaring episodes. Nevertheless, the minimum count rate level of these transient sub-flares is significantly above the count rate level of persistent epochs like XM1 and XM3. Thus, the whole ~ 80 ksec long flare in the XM4 epoch is considered as a single flaring epoch for our scientific analysis. The hardness ratio in the XM2 and XM4 epochs demonstrates that the variability in the light curves is significantly different in the two energy bands, and the flaring events are stronger in the hard spectral band (above ~ 1 keV). However, XM1 and XM3 epochs do not show any flaring events. Thus, the hardness ratio remains nearly constant for these two persistent epochs.

The inherent properties of the transient events occurring in ULXs are often best understood by short-term variability studies. A simple Fourier space investigation of the time series is the first task to search for such variabilities. We perform the power spectral density (PSD) analysis but find no evidence of quasi-

periodic or periodic oscillation in any of the observations. We, nevertheless, detect the presence of red noise at low frequencies in some of the observations. In figure 3.2, we show the PSDs from the pn and MOS2 light curves of the XM4 epoch. We can detect powerlaw like PSD manifesting the red noise in both data. Detection of such red noises in both pn and MOS instruments suggests that the nature of the power spectrum is related to the intrinsic properties of the source and not just due to any artifact owing to the bad column or chip gap in pn data.

An essential aspect of time series analysis in ULXs is to search for transient pulsation. As discussed earlier, the acceleration search technique is essential to detect such transient pulse periods while correcting for the Doppler shift due to binary orbital period correction. We utilize the EPIC pn data for this purpose due to its high time resolution ~ 73.4 ms. We implement `HENaccelesearch` task of HENDRICS to search for pulsation in the 0.3–8.0 keV energy range. We restrict the frequency range within 0.01–6.8 Hz to avoid any artifact due to the Nyquist limit. In this `HENaccelesearch` task, the maximum number of Fourier frequency bins (z_{max}) is used as 100 with a Fourier frequency bin resolution (Δz) of 1. No significant pulsation is detected in any of these epochs.

We also utilize the `HENZsearch` task with a fast-folding algorithm that searches for the first spin derivative to search for pulsation in the same energy and frequency range. No pulsation is detected in this case also. Nevertheless, an important aspect of this tool is that it estimates the upper limit on the pulsed amplitude $\frac{I_{max} - I_{min}}{I_{max} + I_{min}}$ for the best candidate frequency within 90% confidence. Here, I_{max} and I_{min} represent the maximum and minimum values of the folded profile, respectively. It is easy to estimate the upper limit on the pulsed fraction, defined as $\frac{I_{max} - I_{min}}{I_{max}}$ from the pulsed amplitude. We find that in these four epochs, the upper limit on pulsed fraction varies between ~ 10 –17%.

To extend our analysis in smaller time intervals of the flaring epochs, we further divide the XM2 and XM4 epochs into three sub-epochs (see figure 3.3 left and right panel, respectively). They are named pre-flare, flare, and post-flare intervals. The similar count rates and overlapping spectral properties of the pre-flare and post-flare intervals persuade us to combine them as a single “non-flaring” interval. A similar pulsation search exercise using the methods mentioned above is executed in those segmented “flaring” and “non-flaring”

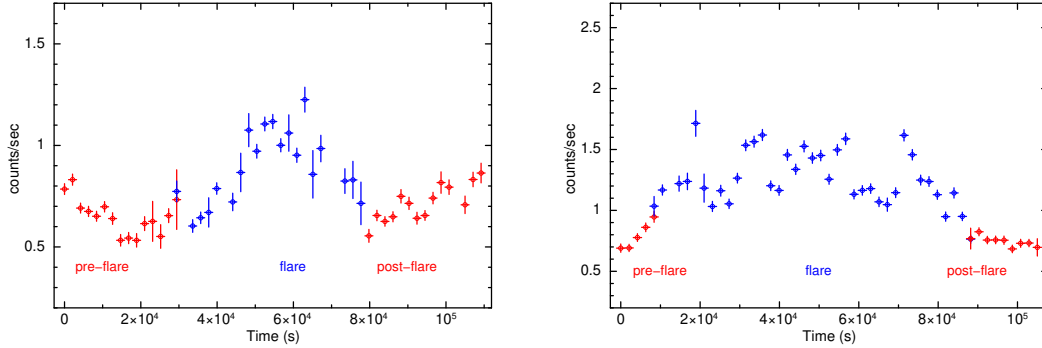


Figure 3.3: For XM2 (left) and XM4 (right) epochs of observation, different transient intervals are defined. The pre-flare, flare, and post-flare intervals are separately indicated. As discussed in the text, the pre-flare and post-flare intervals are combined to get the “non-flaring” interval.

Table 3.2: Fractional variability in pn and MOS lightcurves for all four epochs.

Epoch	pn		MOS	
	soft	hard	soft	hard
XM1	0.17 ± 0.02	0.17 ± 0.02	0.15 ± 0.02	0.11 ± 0.04
XM2	0.11 ± 0.01	0.52 ± 0.04	0.12 ± 0.02	0.47 ± 0.04
XM3	0.15 ± 0.02	0.08 ± 0.06	0.19 ± 0.02	0.09 ± 0.05
XM4	0.15 ± 0.01	0.47 ± 0.03	0.14 ± 0.01	0.47 ± 0.03

intervals. No pulse period is found in either case. During these segmented intervals, the upper limit of the pulsed fraction is found to be varying between ~ 11 – 23% .

We also utilize the `accelsearch` tool from the PRESTO package by employing the “jerk” search technique. The maximum number of Fourier frequency bins is 200, and the maximum number of Fourier frequency derivative bins `wmax` is used as 600 (Andersen & Ransom 2018). The frequency range is restricted within the range specified before. Again, no significant pulsation is detected.

Another quantitative measurement of variability in the light curves is measuring the fractional root mean square (RMS) variability amplitude (F_{var}). This measures the variance of a source over the Poissonian noise in the time series,

normalized to the average count rate (Edelson et al. 2002; Vaughan et al. 2003).

$$F_{var} = \sqrt{\frac{S^2 - \bar{\sigma}^2}{\bar{x}^2}}, \quad (3.1)$$

where $S^2 = \frac{1}{N-1} \sum_{i=1}^N (x_i - \bar{x})^2$ and $\bar{\sigma}^2 = \frac{1}{N} \sum_{i=1}^N \sigma_i^2$. x_i is the count rate at i 'th bin, \bar{x} is the mean count rate, N is the total number of bins, σ_i is the uncertainty in count rate in i 'th bin. The error on F_{var} is quantified as,

$$\sigma_{F_{var}} = \frac{1}{F_{var}} \sqrt{\frac{1}{2N} \frac{S^2}{\bar{x}^2}}. \quad (3.2)$$

We use the 1000 second binned XMM-Newton pn light curves in both soft and hard energy bands and estimate the F_{var} and its error. The measured F_{var} values are listed in table 3.2. To verify whether the variability in pn light curves is an artifact of the bad column or chip gap as described in section 3.2, we also utilize the MOS observations and measure the F_{var} in the light curves. To increase the count statistics, first, we add the MOS1 and MOS2 light curves for both soft and hard energy bands and bin the net light curves by 1000 sec. A similar variability trend is detected in both the pn and MOS data (see table 3.2). Thus, it is confirmed that these variabilities are intrinsic properties of ULX1. The estimates demonstrate that the F_{var} is significantly higher in the flaring XM2 and XM4 epochs than the non-flaring XM1 and XM3 in the hard energy band, i.e., above 1.0 keV. The hard lightcurves in XM2 and XM4 flaring epochs have a fractional variability of $\sim 50\%$, whereas, for the soft lightcurves and the steady XM1 and XM3 epochs, the variability is $\lesssim 20\%$.

3.4 | Spectral Analysis

Here, we discuss the results from spectral analysis of the 2018-2019 XMM-Newton observations in detail. The neutral absorption model Tuebingen-Boulder ISM absorption (tbabs in XSPEC) accounts for both Galactic and local extinctions. The updated abundance (Wilms et al. 2000) and photoionization cross-section (Verner et al. 1996) are used. We use two absorption components where the

Table 3.3: The best fit model (tbabs (GAL) *tbabs*(gauss+diskbb+diskpbb)) parameters of NGC 4395 ULX1 XMM-Newton spectra for the four epochs. The absorbed flux F_x and luminosity L_x are calculated in the 0.3–10.0 keV energy range. The Galactic absorption is fixed to $0.04 \times 10^{22} \text{ cm}^{-2}$. “ p ” value of diskpbb model is fixed to 0.50, resembling a slim disk. The distance is assumed to be 4.76 Mpc (Vinokurov et al. 2018) to calculate the luminosity.

Parameter	Unit	XM1	XM3	XM2	XM4
N_H	10^{22} cm^{-2}	$0.05^{+0.03}_{-0.02}$	$0.06^{+0.03}_{-0.02}$	0.04 ± 0.01	0.05 ± 0.01
E_{line}	keV	0.91 ± 0.02	0.92 ± 0.02	$0.92^{+0.03}_{-0.04}$	$0.95^{+0.02}_{-0.03}$
σ_{line}	keV	$0.15^{+0.03}_{-0.02}$	$0.11^{+0.03}_{-0.02}$	$0.14^{+0.04}_{-0.03}$	0.13 ± 0.03
$Norm$	$10^{-5} \text{ photons cm}^{-2} \text{ s}^{-1}$	$5.71^{+2.90}_{-1.54}$	$3.68^{+2.03}_{-0.96}$	$4.12^{+2.44}_{-1.33}$	$3.86^{+1.67}_{-1.03}$
T_{thin}	keV	$0.17^{+0.03}_{-0.04}$	$0.18^{+0.02}_{-0.03}$	$0.22^{+0.02}_{-0.03}$	$0.22^{+0.02}_{-0.03}$
$norm_{thin}$		55^{+95}_{-28}	42^{+85}_{-18}	20^{+19}_{-7}	16^{+13}_{-6}
T_{slim}	keV	$0.54^{+0.07}_{-0.05}$	$0.58^{+0.12}_{-0.09}$	$0.78^{+0.08}_{-0.07}$	0.84 ± 0.05
$norm_{slim}$		$0.06^{+0.04}_{-0.03}$	$0.03^{+0.06}_{-0.02}$	0.02 ± 0.01	0.02 ± 0.01
$\chi^2/d.o.f$		165/168	150/140	218/206	275/238
F_x	$10^{-13} \text{ erg s}^{-1} \text{ cm}^{-2}$	5.31 ± 0.12	5.26 ± 0.14	9.24 ± 0.18	11.06 ± 0.17
L_x	$10^{39} \text{ erg s}^{-1}$	1.44 ± 0.03	1.43 ± 0.04	2.51 ± 0.05	3.0 ± 0.05

Galactic absorption column¹ is a fixed parameter at the value of $0.04 \times 10^{22} \text{ cm}^{-2}$ (HI4PI Collaboration et al. 2016) and the local absorption is measured by another tbabs component which is allowed to vary as a free parameter. The statistical uncertainties in the spectral parameters are measured within a 90% confidence interval unless mentioned otherwise. The fluxes and their errors are estimated using the model cflux.

3.4.1 | Time-averaged spectroscopy

We first analyze the spectra from individual epochs and investigate the time-averaged spectroscopic properties of the source in each epoch. The MOS1 spectra for all four epochs are plotted in figure 3.4 - top left panel.

¹<https://heasarc.gsfc.nasa.gov/cgi-bin/Tools/w3nh/w3nh.pl>

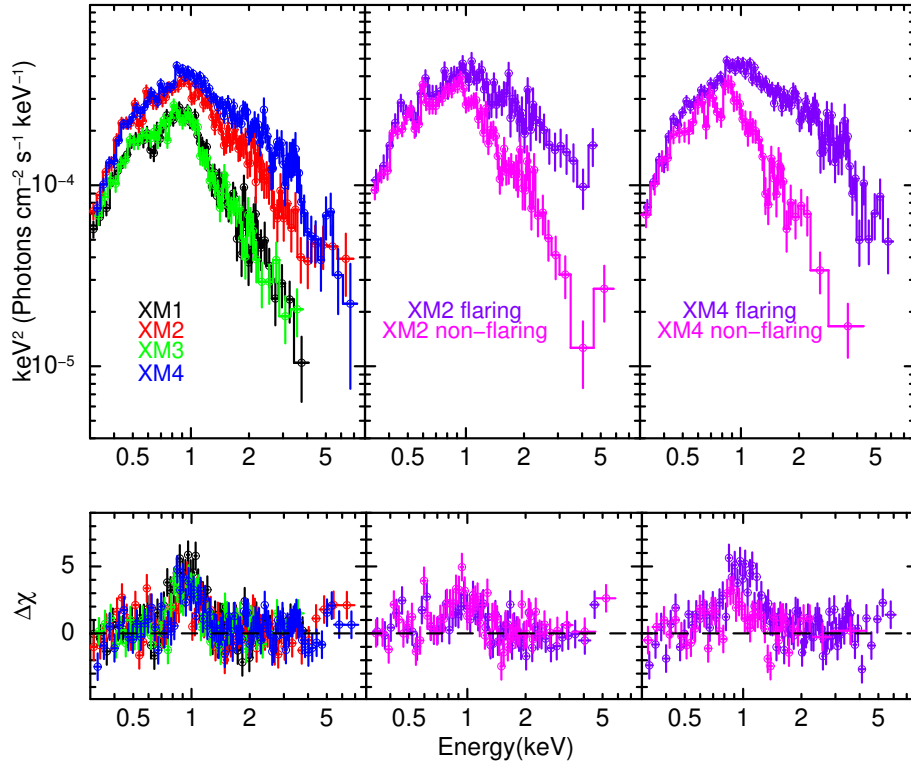


Figure 3.4: Top: The unfolded MOS1 spectra for different epochs are plotted. Simple powerlaw model of zero photon index ($\Gamma = 0$) is used to unfold the spectra. The normalization of the model is kept arbitrarily high for plotting purposes. A significant long-term spectral variability is observed in different epochs of ULX1 spectra. In the left panel, the MOS1 spectra of the XM1 and XM3 epochs exhibit overlapping spectral features. XM2 and XM4 epochs clearly show differences in spectral shapes and divergence in hard spectral regimes. From the time-resolved spectroscopic analysis, the flaring and non-flaring spectra of the XM2 and XM4 epochs are plotted in the middle and right panels. A similar divergence in spectral characteristics predominantly above 1 keV is seen in these two figures. Bottom: The residuals of the best-fit continuum are shown for MOS1 spectra corresponding to the epochs shown in the top panels. For plotting purposes, the Gaussian component is removed from the best-fit model to show the significant contribution of Gaussian in the spectra.

The spectra of the XM1 and XM3 epochs exhibit similar features in terms of flux and spectral profile. Spectra from both epochs are steep and extend only up to ~ 5 keV, after which the background starts dominating. Whereas the flaring epochs XM2 and XM4 have comparatively harder spectra and higher flux compared to the other two epochs, and their spectra extend up to ~ 8 keV, after which the S/N decreases significantly.

It is important to verify whether the chip gap and strong bad column issue in the pn data affect the source spectral properties. For that purpose, we carry out an individual analysis of pn and MOS1/2 data for all four observations with a simple absorbed `powerlaw` model along with an additional Gaussian component. The necessity of the Gaussian component is discussed below. We find that the spectral parameters from pn data are consistent with the MOS1/2 data within the statistical confidence range, with the only exception of the normalization component of the `powerlaw` model in XM3 and XM4 epochs. Hence, we perform simultaneous fitting of pn and MOS1/2 data for each epoch with the cross-calibration constant fixed to 1 for the MOS1 camera, and for the MOS2 and pn camera, the cross-calibration constant parameter is left free to vary. The other parameters of the models are tied between the cameras. As expected, the cross-calibration values remain within 10% of MOS1, except for pn data in XM3 and XM4 epochs, since these pn data are most affected by the noisy detector column and chip gap as described in Section 3.2.

We explore various physically motivated and phenomenological models in XSPEC to quantify the contribution of different emission mechanisms in ULX1 spectra. To characterize the spectral hardness of individual epochs, we use the simple `powerlaw` fit. The powerlaw index in XM1 and XM3 epochs are found to be ~ 4.6 and ~ 4.8 , respectively, and in XM2 and XM4 epochs, they are ~ 3.7 and ~ 3.5 respectively. It is clear that the flaring epochs XM2 and XM4 are spectrally harder than XM1 and XM3 epochs. It is also interesting to compare the spectral photon indices of NGC 4395 ULX1 with those observed from canonical BH XRBs that range between ~ 1.7 in low/hard state to ~ 2.5 in steep power-law state or very high state (Remillard & McClintock 2006). Thus, it is found that in all epochs, ULX1 spectra are much steeper compared to the spectra of sub-Eddington BH XRBs. On top of the powerlaw continuum, we detect a soft

excess around ~ 0.4 keV and a broad Gaussian emission-like feature around ~ 0.9 keV. A more complicated model consisting of a thermal blackbody disk, a powerlaw, and a Gaussian can provide a good fit to the ULX1 spectra in all epochs. Nevertheless, it is crucial to understand that the powerlaw model extends to low energies arbitrarily, which can cause degeneracy between parameters of the powerlaw component and the other low energy components like the extinction or Gaussian line. Hence, it is prudent to explore other models for ULX1 spectra that provide more robust, physically consistent descriptions.

Two-component models composed of a cool and a hot thermal component are widely used to justify ULX spectra. Soft ULXs like NGC 55 ULX and NGC 247 ULX-1 to moderately hard ULXs like NGC 1313 X1 and NGC 4559 X7 have been modeled with such combination of two thermal component models (Kara et al. 2020; Pinto et al. 2017, 2020; Pintore et al. 2021; Walton et al. 2020). An interpretation would be that the cooler component originates from the outer disk, and the hotter component comes from the inner accretion disk, the geometry of which would depend on the accretion rate of the system. Such a physical scenario motivates us to explore a continuum with a thin accretion disk and a slim accretion disk to fit the NGC 4395 ULX1 spectra. We find that a cool thermal component, represented by a `diskbb` in XSPEC and a comparatively hotter slim accretion disk (`diskpbb` in XSPEC, with $p = 0.50$) provide an adequate continuum description in all epochs. The “ p ” parameter of the `diskpbb` model always gives the value close to the lower limit of the parameter, i.e., 0.50. Hence, we keep the parameter fixed to the value of 0.50 and let other parameters free to vary. It is important to reiterate that the $p = 0.50$ is the slim disk limit. On top of the continuum, we find that a broad Gaussian-like feature around 0.9 keV is always prominent. We find that without any such Gaussian model component, the $\chi^2/d.o.f$ for only continuum fits are 402/171 for XM1, 297/209 for XM2, 255/143 for XM3, and 375/241 for XM4 epochs. However, if we include the Gaussian component to model such a broad feature, the fit statistics are significantly improved (see table 3.3). Thus, the best-fit description of a physically motivated model that we use to fit the data is `tbabs(Gal)*tbabs*(gauss+diskbb+diskpbb)`.

The absorption parameter N_H value remains consistent in all four epochs

Table 3.4: Parameters for the time-resolved spectroscopic analysis of XM2 and XM4 epochs using best-fit model same as in table 3.3.

Parameter	Unit	XM2		XM4	
		flaring	non-flaring	flaring	non-flaring
N_H	10^{22} cm^{-2}	$0.05^{+0.07}_{-0.02}$		0.07 ± 0.02	
E_{line}	keV	$0.90^{+0.03}_{-0.02}$		$0.91^{+0.02}_{-0.04}$	
σ_{line}	keV	$0.19^{+0.11}_{-0.08}$	$0.15^{+0.12}_{-0.05}$	$0.21^{+0.02}_{-0.03}$	$0.09^{+0.06}_{-0.03}$
$Norm$	$10^{-5} \text{ photons cm}^{-2} \text{ s}^{-1}$	$7.09^{+10.98}_{-4.65}$	$5.83^{+29.76}_{-2.5}$	$9.63^{+2.87}_{-3.85}$	$4.35^{+5.33}_{-1.41}$
T_{thin}	keV	$0.18^{+0.10}_{-0.09}$	$0.18^{+0.04}_{-0.09}$	$0.15^{+0.07}_{-0.02}$	$0.18^{+0.02}_{-0.05}$
$norm_{thin}$		32^{+3983}_{-27}	41^{+3139}_{-23}	68^{+259}_{-59}	58^{+204}_{-26}
T_{slim}	keV	$0.89^{+0.21}_{-0.08}$	$0.52^{+0.08}_{-0.05}$	$0.80^{+0.02}_{-0.03}$	$0.56^{+0.18}_{-0.11}$
$norm_{slim}$		0.02 ± 0.01	$0.11^{+0.12}_{-0.07}$	0.04 ± 0.01	$0.05^{+0.14}_{-0.04}$
$\chi^2/d.o.f$		349/327		409/344	
F_x	$10^{-13} \text{ erg s}^{-1} \text{ cm}^{-2}$	$12.36^{+0.45}_{-0.42}$	7.87 ± 0.21	12.49 ± 0.21	6.50 ± 0.25
L_x	$10^{39} \text{ erg s}^{-1}$	$3.35^{+0.12}_{-0.11}$	2.14 ± 0.06	3.39 ± 0.06	1.76 ± 0.07

($\sim 0.05 \times 10^{22} \text{ cm}^{-2}$). Similarly, the Gaussian line energy remains consistent at a $\sim 0.9 \text{ keV}$ value. The temperature of the low-energy thin disk component also remains similar in these four epochs. However, the temperature of the hot inner disk component of `diskpbb` model is higher in the XM2 and XM4 epochs compared to that of the XM1 and XM3 epochs. Typically, the average `diskpbb` temperature in the XM2 and XM4 epochs is ~ 1.5 times higher than that in the XM1 and XM3 epochs. The best-fit parameters are noted in table 3.3. The residuals from the same model for MOS1 spectra are plotted in the bottom left panel of figure 3.4 for each observation. The Gaussian component is removed from the best-fit model in the plot for visual purposes. The strong presence of such a Gaussian-like structure is evident from the residual plots. The model components are shown in figure 3.5 (top panel). The contribution of each component and their variation in different epochs is clear from the figure.

3.4.2 | Time-resolved spectroscopy

An interesting approach to understanding the properties of flaring episodes in ULX1 described in section 3.3 is to conduct a robust comparative study of the

spectral properties in flaring and non-flaring epochs. Here, we primarily consider the XM2 and XM4 epochs, where the flares are prominent. As discussed earlier, we divide the XM2 and XM4 epochs into three sub-epochs: pre-flare, flare, and post-flare. Since the spectral flux and properties overlap during pre-flare and post-flare regimes, we consider them as single non-flaring intervals. The flaring and non-flaring spectra of MOS1 for the XM2 and XM4 epochs are overplotted in figure 3.4 top middle and right, respectively. Apparently, the spectra of flaring and non-flaring states remain consistent below 1 keV but significantly diverge in the higher energy band, i.e., after 1 keV. This property has already been shown in part from the timing analysis.

Since the $\text{tbabs}(\text{Gal}) * \text{tbabs} * (\text{gauss} + \text{diskbb} + \text{diskpbb})$ model adequately describes the spectra from both steady XM1 and XM3 epochs and the flaring XM2 and XM4 epochs, we fit the same model for the time-resolved spectra of the flaring epochs. The flaring and non-flaring spectra are fitted simultaneously for each observation, linking absorption and line energy parameters but letting the disk parameters vary freely. The best-fit values of the spectral parameters and their error estimates are quoted in table 3.4. Figure 3.4 shows the residuals from the best-fit model (without the Gaussian component) for MOS1 spectra of the XM2 epoch (bottom-middle) and XM4 epoch (bottom-right). Interestingly, similar to the time-averaged spectroscopic results, the cool `diskbb` temperature remains similar between flaring and non-flaring episodes. However, the best-fit `diskpbb` temperature in the flaring episode of XM2 is ~ 1.7 times higher than the non-flaring episode. For the XM4 epoch, the factor is ~ 1.4 . Also, as expected, the spectral parameters of non-flaring episodes of XM2 and XM4 epochs remain consistent with the values estimated for XM1 and XM3 epochs where no flaring is detected. Especially the similar temperature of the disk components could indicate steady accretion in the non-flaring episodes of XM2 and XM4 and the steady XM1 and XM3 epochs. Figure 3.5 (bottom panel) shows the model components for flaring and non-flaring spectra. The variation of contribution from spectral components due to flaring events is seen from the figure, specifically the variation in `diskpbb` component.

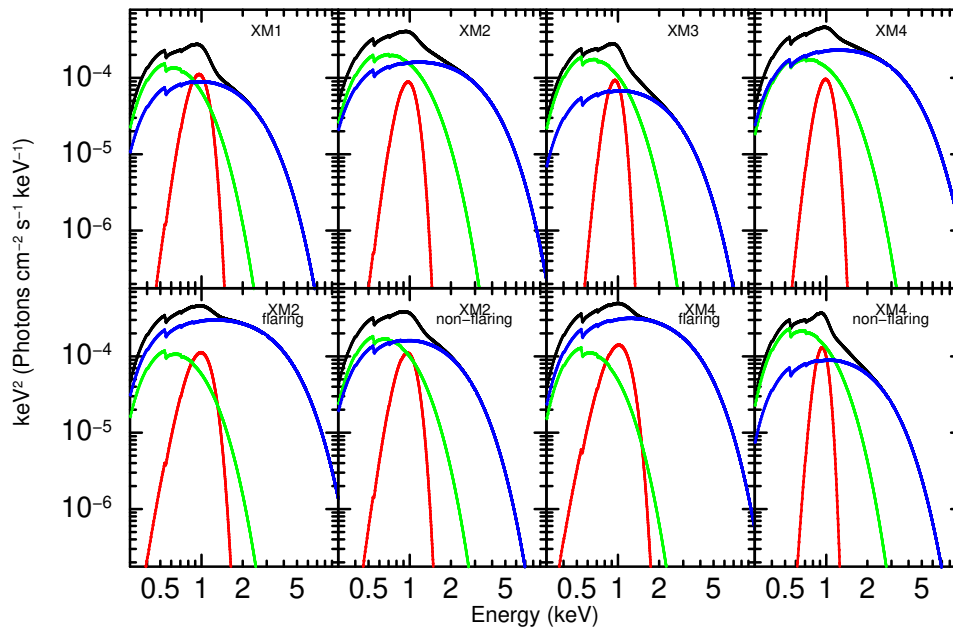


Figure 3.5: The model components are shown for MOS1 spectra of different epochs. The red component is the gaussian, green represents the diskbb, and blue represents diskpbb components. Black represents the total model. The variation in the diskpbb model component due to flaring incidents is clear from the figure.

3.5 | Discussions

Previously [Earnshaw & Roberts 2017](#) analyzed some archival data of ULX1, including data from XMM-Newton observations, and showed that ULX1 spectra exhibit a steep powerlaw tail and a presence of Gaussian-like feature near ~ 0.9 keV, which a mekal model could explain. Nevertheless, recent studies of multiple ULX sources suggest that a two-component thermal model might be more physically motivated to describe the spectra of ULXs ([Kara et al. 2020](#); [Pinto et al. 2017, 2020](#); [Walton et al. 2020](#)).

An interpretation of the two-thermal component is that accretion disks around ULXs have a two-tiered structure. Far from ULXs, the disk is a typical thin accretion disk (Shakura & Sunyaev 1973). Once the local luminosity of the disk approaches the Eddington limit, the inner region of the disk inflates. Winds are launched down the spherization radius, which carries away the excess mass, and advection plays a crucial role inside the accretion disk. Such a physical scenario would depict that the low-energy thermal disk component corresponds to the outer thin accretion disk, and the high-energy component corresponds to the inner accretion flow from a slim accretion disk modified by the disk wind. Considering this physical accretion scenario, we would discuss how these new XMM-Newton observations conform with the description.

Before 2018, the XMM-Newton observations of NGC 4395 ULX1 do not show any significant short-term variability in the source (Earnshaw & Roberts 2017). However, significant flaring episodes are detected in the latest 2018-2019 observations. The hard spectral component is best described by the radial advection of the slim accretion disk component modeled by `diskpbb`, which eventually implies the super-critical accretion scenario. The luminosity measurement ($L \sim 1.4\text{--}3.0 \times 10^{39} \text{ erg s}^{-1}$) shows that if ULX1 hosts a typical $\sim 10M_{\odot}$ black hole, then it is accreting at or just above the Eddington accretion rate. Thus, as a first impression, one might compare the ULX1 spectral state with the broadened disk spectrum while comparing it with known ULX spectral categories. Nevertheless, it is crucial to note that the hot inner disk temperature of ULX1 is relatively less than the typical hot temperature found in BD state ULX sources. Also, in addition, ULX1 requires a cool thermal component, not typically seen in BD ULXs. An alternative comparison would be with SUL or ULS sources based on the soft nature of ULX1. In all observations, the source exhibits a powerlaw photon index of $\Gamma > 2$ in the 0.3–5.0 keV energy band; hence an apparent classification would be that NGC 4395 ULX1 is a soft ultraluminous source. However, many SUL sources show higher luminosity compared to what is observed for NGC 4395 ULX1 (Sutton et al. 2013). There cannot be a direct comparison with ULSs since ULS sources usually exhibit a single ultrasoft blackbody spectrum, whereas ULX1 shows two disk component spectra. Thus, we infer that NGC 4395 ULX1 is an intermediate case between SUL and ULS state

sources. It is interesting to compare that the spectral properties of NGC 4395 ULX1, like the spectral profile, two thermal component continuum, and atomic emission/absorption-like features, are similar to those of NGC 55 ULX and NGC 247 ULX-1, in particular (Pinto et al. 2017, 2021). The geometry of the accretion disk might be a key factor for the soft spectral nature of the source. The line of sight could be nearer to the plane of the disk, thus obscuring the hard photons coming from the inner and hotter region of the accretion disk (see similar discussion for NGC 55 ULX in Pinto et al. 2017).

The power spectral density of the ULX1 time series in a few observations shows powerlaw type low-frequency red noise. Variation in mass accretion rate in X-ray binaries can cause such red noise in the power spectrum (Uttley & McHardy 2001). However, on top of the red and white noise, no quasi-periodic or periodic oscillation signature is found in any of the observations. The energy-dependent analysis of the time series of flaring XM2 and XM4 epochs confirms that the hard spectral components dominate the flaring activities. Similar behavior is observed in some other ULXs (e.g. Gúrpide et al. 2021a,b; Middleton et al. 2015a). One interpretation could be the partial occultation of the inner region of the accretion disk due to the outflowing wind launched by the super-critical accretion. In principle, this might explain our results since the presence of a Gaussian-like feature also supports the presence of outflowing wind. Another interpretation could be that this variability happens due to a genuine change in the accretion rate, which eventually contributes to the flaring behavior.

The luminosity-temperature relation in a standard thin accretion disk follows $L \propto T^4$ relation. However, in the absence of beaming, for an advection-dominated disk, the relation is $L \propto T^2$ (Kubota & Makishima 2004). This could be the case in our data, as we show in figure 3.6. We plot the unabsorbed bolometric luminosity in 0.01–10.0 keV energy band from the `diskpbb` component and corresponding disk temperature. We have extended the energies of the instrumental responses in XSPEC to obtain the bolometric flux (F_{bol}) from the `diskpbb` component following a similar study by Urquhart & Soria 2016. For this luminosity-temperature relation analysis, we have also included two additional XMM-Newton observations (ID - 0142830101,0200340101) to increase the statistics in the luminosity vs. temperature plot. These two observations are chosen,

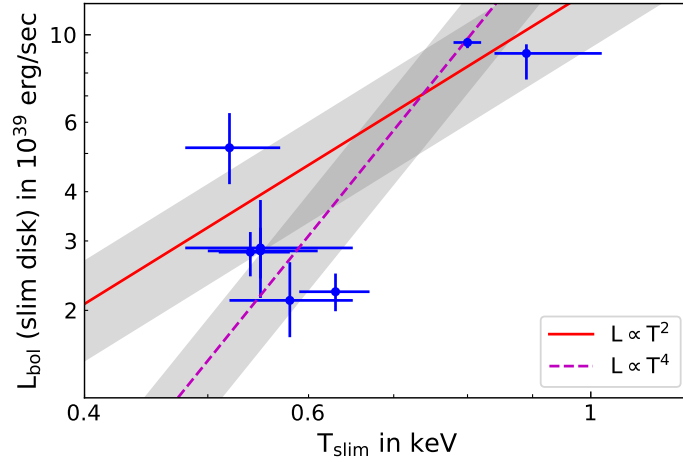


Figure 3.6: Relation between the unabsorbed bolometric luminosity of the hard slim disk component vs. temperature of that disk. The 95% confidence intervals on the normalizations of the powerlaw relations are indicated with the shaded regions.

particularly since their exposures are comparable to those of the four observations studied here. In these two older observations, the source exhibits similar spectral characteristics as it shows in the non-flaring epochs of the 2018-2019 observations. The spectral parameters of these two observations are consistent with those of the non-flaring epochs when fitted with the same spectral model.

We followed the same data reduction method for these two observations as we did for other observations in this chapter. The source exhibits steep spectra extending up to only 5 keV, similar to the non-flaring XM1 and XM3 epochs, after which the background starts significantly dominating the source spectra. In observation 0142830101, the pn data is affected by chip gap and bad column, as happened for other observations discussed in this chapter. To verify whether the spectral properties are affected due to the chip gap and bad column, we give a similar treatment as described in sections 3.2 and 3.4. Simultaneous pn and MOS1/2 data fitting is performed with cross-calibration of MOS1 fixed to 1 and left free to vary for MOS2 and pn cameras. In observation 0200340101, the pointing of the detector is such that the source is highly off-axis (see also [Earnshaw & Roberts 2017](#)) and falls out of the field of view of the pn camera.

Thus, for this observation, only MOS1 and MOS2 data are utilized.

We have utilized the data points from flaring and non-flaring epochs for XM2 and XM4 epochs, and for other observations, the time-averaged data points are used. The bolometric luminosity and disk temperature and their 1σ errors are obtained. Then, we fit the data using `scipy.odr` routine² (Boggs & Rogers 1990) with both $L \propto T^2$ and a $L \propto T^4$ relations. To adopt a conservative approach, we consider the larger error on both axes for the fitting method. In figure 3.6, we see that the luminosity-temperature plane of the `diskpbb` component is broadly consistent with both $L \propto T^2$ and $L \propto T^4$ relations. We have also shown the 95% confidence intervals on the normalizations of the powerlaw relations by the shaded regions in the figure.

For a disk inclination angle θ and distance to the source D , the bolometric luminosity is $L_{bol} = \frac{2\pi D^2}{\cos\theta} F_{bol}$. Conventionally, it is assumed that $L_{bol} = 4\pi D^2 F_{bol}$, which is equivalent to the disk inclination angle of $\sim 60^\circ$ (see Urquhart & Soria 2016 for details). We have used the simple $L_{bol} = 4\pi D^2 F_{bol}$ relation to estimating the bolometric luminosity. However, it is important to note that since the inclination angle of the disk is highly uncertain, the absolute value of the L_{bol} needs to be taken with caution. However, the luminosity-temperature plane would follow a fixed positive powerlaw relation for a fixed inclination in all epochs. From the figure 3.6, although the data broadly follow both the relations, empirically, for an advection-dominated accretion disk or a slim disk, the $L \propto T^2$ relation is expected to be more appropriate.

We also study the relation between luminosity and accretion rate for the source. We know that for a slim disk in the presence of advection, the luminosity relates with the Eddington ratio as $L \sim L_{edd}[1 + \ln \dot{m}_0]$ (Shakura & Sunyaev 1973). The ratio of luminosities during flaring and non-flaring episodes is

$$\frac{L_{flare}}{L_{non-flare}} \sim 2. \quad (3.3)$$

Hence, from this relation, we can estimate how the mass accretion rate has changed during flaring events. Simple algebra would lead to the relation between the Eddington ratios of flaring and non-flaring episodes as

²<https://docs.scipy.org/doc/scipy/reference/odr.html>

$$\dot{m}_{0\,flare} \simeq e \cdot \dot{m}_{0\,non-flare}^2. \quad (3.4)$$

However, if the apparent change in the luminosity of the advection-dominated disk is dominated by geometrical beaming from the disk winds, then,

$$L \propto L_{edd}[1 + \ln \dot{m}_0] \dot{m}_0^2, \quad (3.5)$$

since, the beaming factor is proposed to scale as $73/\dot{m}_0^2$ (King & Lasota 2016; King et al. 2017; King 2009). Since, in ULX1, the luminosity ratio is small (~ 2), the relation between luminosity and Eddington ratio would take an approximate form of,

$$\frac{L_{flare}}{L_{non-flare}} \sim \frac{\dot{m}_{0\,flare}^2}{\dot{m}_{0\,non-flare}^2}. \quad (3.6)$$

In this case, the Eddington ratios of flaring and non-flaring episodes would take a simple form as,

$$\dot{m}_{0\,flare} \simeq \sqrt{2} \dot{m}_{0\,non-flare}. \quad (3.7)$$

The spectral parameters can be used to estimate some physical parameters relevant to ULX1 accretion. The normalizations of the accretion disk component provide an estimate of the inner radius (R_{in}) of the disk.

$$R_{in} \simeq \zeta \kappa^2 N^{\frac{1}{2}} D_{10} (\cos \theta)^{-\frac{1}{2}} km, \quad (3.8)$$

where ζ is the geometric correction factor and κ is the color correction factor, D_{10} is the distance in 10 kpc unit, N is the normalization, and θ is the inclination angle of the disk (Kubota et al. 1998; Soria et al. 2015). The inner radius from the disk normalizations is calculated for all four epochs XM1, XM2, XM3, and XM4. The large uncertainty measurement in the normalization parameter of diskbb indicates that the radius of the thin accretion disk can take a very large value ranging between $\sim 2000(\cos \theta)^{-\frac{1}{2}}$ km to $\sim 7000(\cos \theta)^{-\frac{1}{2}}$ km assuming $\zeta \sim 0.412$ and $\kappa \sim 1.7$ (Kubota et al. 1998; Shimura & Takahara 1995), relevant for a thin disk.

However, the normalization of the diskpbb component, i.e., the slim accretion disk, remains similar in different epochs. Hence, we take a simple average to estimate the inner radius of the slim disk. It is important to caution that, to estimate such an inner radius, it is assumed that the radius is, in fact, constant, which is appropriate for $L \propto T^4$ relation. Nevertheless, if the $L \propto T^2$ relation is considered, then the inner radius need not be constant unless advection plays a significant role in the inner accretion flow. Since diskpbb model is just an approximate powerlaw scaled model of the radial dependent temperature, it does not formally include all the physical effects of advection on the inferred inner radius.

For a slim accretion disk, it is more appropriate to assume the value $\xi \sim 0.353$ and $\kappa \sim 3$ (Soria et al. 2015; Vierdayanti et al. 2008). Thus, the radius from the average normalization turns out to be $\sim 273(\cos\theta)^{-\frac{1}{2}}$ km. This corresponds to the last stable circular orbit ($R_{ISCO} = 6GM/c^2$) of a $\sim 31M_\odot$ non-rotating black hole if the disk is face-on, or if the disk inclination is $\sim 60^\circ$, then the mass of the non-rotating black hole would be $\sim 43M_\odot$. On the other hand, if the estimated radius corresponds to the magnetospheric radius of a neutron star, i.e., $R_M = 7 \times 10^7 \Lambda m_1^{\frac{1}{7}} R_6^{\frac{10}{7}} B_{12}^{\frac{4}{7}} L_{39}^{-\frac{2}{7}}$ cm, where $m_1 = M/M_\odot$ is the neutron star mass in solar mass units, $B_{12} = B/10^{12}$ G, $L_{39} = L/10^{39}$ erg s $^{-1}$, $R_6 = R/10^6$ cm and $\Lambda \sim 0.5$ for disk accretion (Mushtukov et al. 2017). Then for a $1.4M_\odot$ neutron star, the estimated magnetic field would be $\sim 6.1 \times 10^{11}$ Gauss for a face on disk geometry or for disk inclination of $\sim 60^\circ$, the magnetic field strength would be $\sim 1.58 \times 10^{12}$ Gauss. The neutron star radius of $\sim 10^6$ cm is used. For disk inclination of $\sim 60^\circ$, the average luminosity in 0.3–10.0 keV is measured for four epochs which is $\sim 2.1 \times 10^{39}$ erg s $^{-1}$. The luminosity would be two times less for a face on disk.

If we consider the above interpretations as the description of ULX1 spectral properties, then the variable part of the spectrum is dominated by the inner disk component. This might be related to an intrinsic variation in accretion rate or due to a variable clumpy wind partially occulting the inner region, which in turn imprints such variability in hard emission. However, it is important to understand that the measured neutral absorption column density remains similar

during these different observation epochs. This suggests that if the wind clouds that block the inner region of the disk are not highly ionized, the transient flaring phenomena are directly related to the inner disk region, which could be far distanced from the wind cloud regions. Nevertheless, if the wind cloud regions are highly ionized, then changes in line of sight scattering would imprint such high variability without exhibiting variation in neutral absorption components.

Another plausible scenario of hard photons dominating the flaring events could be related to the inverse-Compton scattering process. Due to the high accretion rate, the number of inner disk photons can proliferate significantly during the flaring events. These photons would eventually interact with highly energetic electrons via the inverse-Compton process in the Coronal region and thus release harder photons. Hence, we see that flaring events are spectrally harder than non-flaring events.

Finally, the broad Gaussian-like emission feature around ~ 0.9 keV in NGC 4395 ULX1 is similar to such reported detections in several other ULX sources like NGC 1313 X1, NGC 55 ULX, NGC 247 ULX-1 (Pinto et al. 2017, 2020, 2021). The broad feature is a combination of a forest of lines that EPIC instruments cannot resolve. Such lines concentrated around ~ 0.9 keV include Mg XII, Fe XXII-XXIII, Ne X, Ne IX, O VIII, and O VII lines, which have also been observed in soft sources like NGC 55 ULX and NGC 247 ULX-1 (see, e.g., Kosec et al. 2021; Pinto et al. 2017).

It is also important to mention that such ~ 1 keV broad feature in EPIC data can be modeled by emission lines around ~ 0.9 keV or absorptions around ~ 0.7 and ~ 1.2 keV (Middleton et al. 2015a, 2014). However, for the analysis of NGC 4395 ULX1 spectra, we utilize the gaussian model to explain the broad feature owing to its well-constrained parameters and simpler nature of spectral fitting. However, without any confirmation from grating data from RGS, we cannot discard the presence of absorption lines in ULX1 spectra since the spectral resolution of EPIC data is insufficient to decipher all the lines within that energy band. Unfortunately, the S/N of RGS data is poor for all four observations. The background mostly dominates the RGS spectra of ULX1, which did not allow us to precisely quantify any emission or absorption feature present in the source. Future X-ray monitoring of NGC 4395 ULX1 will be crucial in establishing its

transient nature and a better understanding of the physical properties and accretion mechanism of the source.

Spectral variability in NGC 1042 ULX1

This chapter is based on the results that appeared in the literature as Spectral variability in NGC 1042 ULX1, Ghosh T., Rana V., 2022, MNRAS, 517, 4247 (Ghosh & Rana 2022); arXiv:2209.02458

4.1 | Prologue

Investigation of spectral variability in individual ULX sources can indicate some of the crucial features of the accretion mechanism and the nature of the accretors. A systematic study of spectral variability should include the correlation study between different spectral parameters and their implications. Such studies are widely done in the case of XRB and AGN systems (e.g., Yang et al. 2015). With more data availability, similar studies have also been getting attention in the field of ULXs (e.g., Kajava & Poutanen 2009).

A sample of ULXs has been studied by Kajava & Poutanen (2009), which shows distinctive luminosity-spectral photon index (L_X - Γ) correlation and anti-correlation in different sources. Such correlation studies become essential to decipher the variation in ULX accretion scenarios over time. However, it is crucial to consider some critical factors before concluding a correlation property. Since the powerlaw model extends to the lower energy band without any bound, it is evident that the absorption and other soft continuum components, like a cool accretion disk, can become degenerate with the powerlaw component (e.g., Feng

& Kaaret 2009; Kajava & Poutanen 2009; Pinto et al. 2017). Therefore, it is possible that the luminosity contribution from the soft spectral counterparts is often misinterpreted. Hence, it becomes imperative to investigate and mitigate these “artifacts” before establishing that such correlations are based on real physical property.

NGC 1042 ULX1 (2XMM J024025.6-082428) is an extreme ULX. Sutton et al. (2012) studied that the peak X-ray luminosity of the source reaches $L_X \sim 5 \times 10^{40}$ erg s⁻¹. NGC 1042 is a SAB(rs)cd type galaxy, and the distance to the galaxy is ~ 18.9 Mpc. Sutton et al. (2012) investigated a population of extremely bright ULXs using archival X-ray data from the XMM-Newton and Chandra observatories. One of the extremely luminous ULX in that sample is NGC 1042 ULX1. In this chapter, we study ULX1 utilizing seven archival XMM-Newton observations, three of which (0093630101, 0306230101, 0553300401) were studied in detail by Sutton et al. (2012). We also analyze one NuSTAR observation of ULX1 to investigate its high energy properties beyond ~ 10 keV. Our main focus is on the spectral characteristics and variability of the source in different XMM-Newton observations and exploring a detailed investigation of how the different spectral parameters vary over time. A crucial property that we investigate with NuSTAR data is searching for typical spectral curvature in NGC 1042 ULX1. Such a curvature is not detected in any XMM-Newton observation.

The details of observations and the analysis procedure for this chapter are discussed in section 4.2. The main results of NGC 1042 ULX1 spectral and timing analysis are discussed in section 4.3. Finally, section 4.4 includes a detailed discussion of the analysis.

4.2 | Observation details

We study all archival XMM-Newton (Jansen et al. 2001) and one new NuSTAR (Harrison et al. 2013) observation of NGC 1042 ULX1. The details of observations used in this chapter are given in table 4.1. None of the archival XMM-Newton observations are pointed observations for NGC 1042 ULX1. Those observations primarily targeted other sources like NGC 1052 galaxy and SDSSJ024052-

Table 4.1: The observation details of NGC 1042 ULX1 utilized in the chapter. The cleaned spectral exposures are mentioned for MOS1/MOS2/pn for XMM-Newton and FPMA/FPMB for NuSTAR in ksec unit

Serial No.	Observation ID	Date of observation	Epoch ID	Exposure
XMM-Newton				
1	0093630101	2001-08-15	XM1	13.6/-/9.8
2	0306230101	2006-01-12	XM2	49.4/47.9/-
3	0553300301	2009-01-14	XM3	46.8/44.5/-
4	0553300401	2009-08-12	XM4	53/-/42.6
5	0790980101	2017-01-17	XM5	48.5/46/-
6	0865260301	2021-01-29	XM6	-/19.9/16.3
7	0891800401	2021-07-16	XM7	26.4/26.4/20.5
NuSTAR				
1	30701004002	2021-12-16	N1	104/103

082827. Therefore, ULX1 falls highly off-axis in most observations in XMM-Newton detectors. As a consequence, all three EPIC cameras do not always simultaneously detect the source. The NuSTAR observation taken in 2021 was part of a joint NICER+NuSTAR venture. However, unfortunately, we find that the background completely dominates the NICER spectrum of the source. Hence, we only utilize the NuSTAR data for our scientific purposes.

After extracting the XMM-Newton science products following the standard procedure, we clean the data from the background and proton flare by eliminating the time intervals strongly affected by flaring activities by identifying those intervals in the single event high energy light curves ¹. We then perform a detailed spectral and timing study of NGC 1042 ULX1. We employ a stringent filtering constraint of FLAG== 0 for the spectral analysis of both pn and MOS data.

As mentioned earlier, the source ULX1 (RA: 02:40:25.6, Dec.: -08:24:30.0; [Sutton et al. 2012](#)) is highly off-axis in most of the XMM-Newton observations. Nevertheless, a 30 arcsec radius circle encloses the source region in all obser-

¹<https://www.cosmos.esa.int/web/xmm-newton/sas-thread-epic-filterbackground>

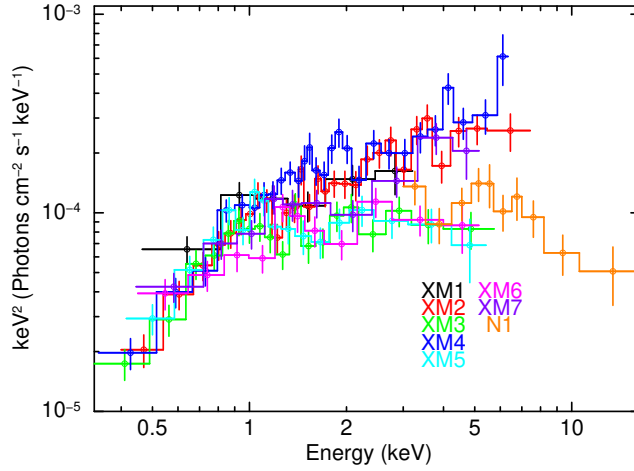


Figure 4.1: The XMM-Newton and NuSTAR unfolded spectra of ULX1. A zero photon index powerlaw model is used to unfold the spectra and for visual purposes, the spectra have been rebinned. The MOS1 spectra are plotted for all XMM-Newton observations except for the XM6 epoch, for which the MOS2 spectrum is shown. For the N1 observation, the spectrum from the FPMA module is presented.

observations. Thus, it is reasonable to consider ULX1 as a point source in all cases. The source photons are extracted from a 30 arcsec circle around the source, and a nearby source-free 60 arcsec circle from the same chip is used for extracting corresponding background photons. The `specgroup` task is utilized to group the spectra with a minimum of 20 counts per energy bin and an oversampling factor 3 has been used to ensure the minimum width of a group as $1/3$ of the corresponding energy resolution (in full-width half maxima).

The standard data reduction process for NuSTAR is followed as discussed in chapter 2. The grouping of NuSTAR spectra is performed to ensure a minimum of 20 counts per energy bin. In the NuSTAR detectors, the source region is selected as a 30 arcsec circle around the source, and the background is chosen from a 60 arcsec radius circle in a nearby source-free region.

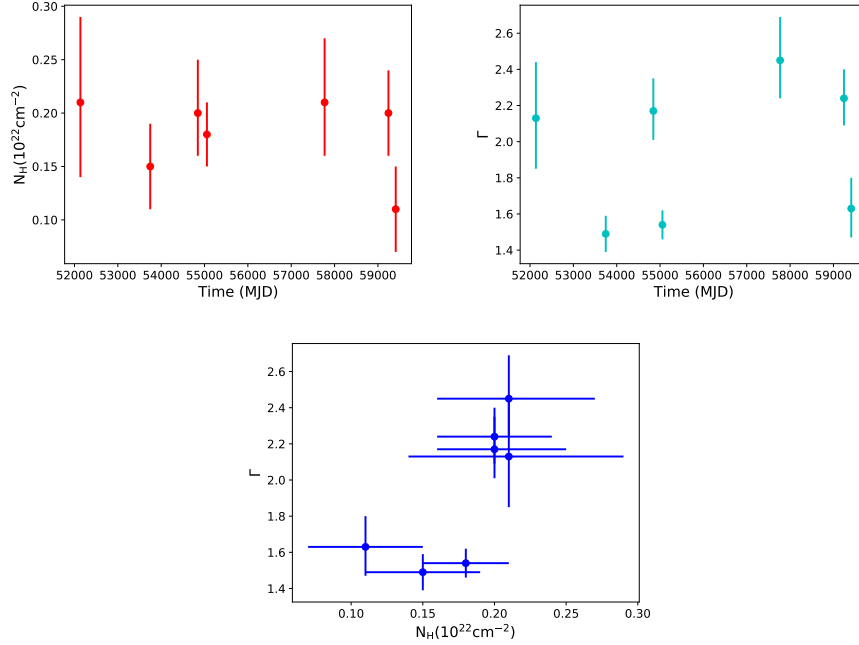


Figure 4.2: The N_H and Γ variation over different XMM-Newton observation epochs are shown in the top left and right panels, respectively. The relation between the N_H and Γ is depicted in the bottom panel. We utilize an absorbed powerlaw model with the N_H parameter being allowed to vary for different epochs of observation for these parameter estimates.

4.3 | Results

4.3.1 | Spectral Analysis

In this section, we discuss the results from the spectral analysis of NGC 1042 ULX1. The analysis followed the standard procedure discussed in previous chapters. The `tbabs` model with updated abundances (Wilms et al. 2000) and cross-sections (Verner et al. 1996) is used to quantify the neutral absorption component. Similar to the previous chapter, we report uncertainties on the measured spectral parameter with a 90% confidence interval unless mentioned otherwise. The `cflux` model estimates the fluxes and their errors throughout the chapter.

As a first exercise, we inspect the source spectral properties visually by plotting the unfolded spectra from all observations studied in this chapter (see fig-

ure 4.1). For this purpose, we have used a `powerlaw` model with zero photon index, i.e., essentially a constant model, to generate the unfolded spectra. Apparently, below ~ 1 keV, the spectra from all epochs remain mostly overlapping. However, above ~ 1 keV, the variability in different epoch spectra is clearly observed. For XMM-Newton spectra, the S/N decreases significantly after 8.0 keV; for NuSTAR spectra, the background dominates significantly after 20.0 keV. Hence, we restrict the analysis of XMM-Newton spectra within the 0.3–8.0 keV energy range, and for NuSTAR spectra, 3.0–20.0 keV energy range is utilized.

We start with a simple absorbed `powerlaw` model to simultaneously fit the spectra from individual XMM-Newton epochs and observe the variation of spectral parameters during these epochs. For each observation, the parameters from all cameras are linked except for a constant parameter. This constant parameter is allowed to vary to take into account the cross-calibration effects. However, the parameters for each epoch are not linked to other epochs and are left free to vary. The time evolution of the parameters N_H and Γ and their correlation properties are plotted in figure 4.2. The neutral absorption parameter N_H is found to be consistent within error among these different epochs of observation (see figure 4.2 - top left). Nevertheless, interestingly, we find that the spectral photon index (Γ) shows a significant variation in different epochs ranging between ~ 1.4 – 2.7 (see figure 4.2 - top right). The relation between N_H and Γ is shown in figure 4.2 - bottom panel. This figure depicts that N_H does not have any substantial influence on the significant variation of photon indices in different epochs.

We also simultaneously fit spectra from all XMM-Newton epochs by keeping N_H free to vary globally but linking between different epochs to inspect the influence of N_H on the spectral hardness and flux. We find that keeping N_H linked between different epochs does not significantly alter the fit statistics in terms of $\chi^2/d.o.f$ from 631/534 to 642/540, which is expected since the N_H parameter in all epochs is found to be statistically similar. Nevertheless, more importantly, this comes with a prize of better constraints on the other spectral parameters. Our primary aim is to quantify the spectral variability for different epochs by robust measurements of the continuum spectral parameters. Hence, we keep this N_H parameter linked for further analysis of XMM-Newton data. Linking the N_H parameter also ensures that the apparent spectral variability in the con-

Table 4.2: Spectral parameter details for the powerlaw model with linked N_H , in seven epochs of XMM-Newton observation of NGC 1042 ULX1. We list the observed (absorbed) fluxes and luminosities in 0.3–8.0 keV energy range. The intrinsic (unabsorbed) fluxes are typically ~ 1.2 – 1.6 times the observed fluxes.

Parameters	Unit	XM1	XM2	XM3	XM4	XM5	XM6	XM7
Model = tbabs*powerlaw								
N_H	10^{22}cm^{-2}	0.18 ± 0.02						
Γ		2.00 ± 0.14	1.55 ± 0.07	2.11 ± 0.10	1.53 ± 0.06	$2.34^{+0.12}_{-0.11}$	2.17 ± 0.09	$1.84^{+0.12}_{-0.11}$
N_{pl}	10^{-4}	$1.51^{+0.20}_{-0.19}$	1.19 ± 0.08	1.01 ± 0.08	1.46 ± 0.10	1.18 ± 0.10	0.98 ± 0.10	1.20 ± 0.13
$\chi^2/d.o.f$		642/540						
F_{obs}	$10^{-13} \text{erg s}^{-1} \text{cm}^{-2}$	$5.72^{+0.81}_{-0.76}$	$6.96^{+0.44}_{-0.43}$	$3.54^{+0.28}_{-0.27}$	$8.77^{+0.53}_{-0.52}$	$3.55^{+0.31}_{-0.30}$	$3.28^{+0.32}_{-0.31}$	$5.26^{+0.59}_{-0.57}$
L_{obs}	$10^{+40} \text{erg s}^{-1}$	$2.44^{+0.35}_{-0.32}$	$2.98^{+0.19}_{-0.18}$	$1.51^{+0.12}_{-0.11}$	3.75 ± 0.22	1.52 ± 0.13	$1.40^{+0.14}_{-0.13}$	$2.25^{+0.25}_{-0.24}$

Table 4.3: Spectral parameter details for the diskbb+powerlaw model in seven epochs of XMM-Newton observation of NGC 1042 ULX1. The observed (absorbed) fluxes and luminosities are measured in 0.3–8.0 keV energy range. We also quantify the intrinsic flux of the individual additive components in the same energy range.

Parameters	Unit	XM1	XM2	XM3	XM4	XM5	XM6	XM7
Model = tbabs(diskbb+powerlaw)								
N_H	10^{22}cm^{-2}	$0.23^{+0.04}_{-0.03}$						
T_{in}	keV	$0.23^{+0.04}_{-0.03}$						
N_{disk}		$6.20^{+10.31}_{-4.45}$	$2.82^{+5.78}_{-1.94}$	$3.67^{+6.42}_{-2.41}$	$2.45^{+5.60}_{-1.82}$	$6.46^{+9.50}_{-3.48}$	$2.70^{+5.66}_{-2.30}$	$6.38^{+9.91}_{-3.47}$
Γ		$1.56^{+0.49}_{-0.47}$	1.39 ± 0.13	1.81 ± 0.28	1.45 ± 0.11	$1.71^{+0.36}_{-0.39}$	$2.01^{+0.27}_{-0.26}$	$1.10^{+0.24}_{-0.25}$
N_{pl}	10^{-4}	$0.99^{+0.51}_{-0.37}$	$0.99^{+0.15}_{-0.14}$	$0.72^{+0.23}_{-0.20}$	1.33 ± 0.16	$0.60^{+0.27}_{-0.22}$	$0.79^{+0.26}_{-0.20}$	$0.58^{+0.18}_{-0.15}$
$\chi^2/d.o.f$		574/532						
Spectral regimes		HUL/SUL	HUL	HUL/SUL	HUL	HUL/SUL	HUL/SUL	HUL
F_{obs}	$10^{-13} \text{erg s}^{-1} \text{cm}^{-2}$	$6.50^{+1.63}_{-1.27}$	$7.24^{+0.49}_{-0.48}$	$3.69^{+0.36}_{-0.34}$	$8.88^{+0.57}_{-0.56}$	$3.85^{+0.44}_{-0.40}$	$3.25^{+0.36}_{-0.34}$	$6.67^{+0.89}_{-0.82}$
L_{obs}	$10^{+40} \text{erg s}^{-1}$	$2.78^{+0.70}_{-0.54}$	3.10 ± 0.21	$1.58^{+0.15}_{-0.14}$	$3.80^{+0.25}_{-0.24}$	$1.65^{+0.19}_{-0.17}$	1.39 ± 0.15	$2.85^{+0.38}_{-0.35}$
F_{pl}	$10^{-13} \text{erg s}^{-1} \text{cm}^{-2}$	$6.87^{+1.08}_{-1.04}$	$8.04^{+0.51}_{-0.5}$	$4.2^{+0.7}_{-0.58}$	$10.18^{+0.6}_{-0.64}$	$3.73^{+0.8}_{-0.64}$	$4.14^{+0.93}_{-0.67}$	$6.36^{+0.76}_{-0.73}$
F_{disk}	$10^{-13} \text{erg s}^{-1} \text{cm}^{-2}$	$2.57^{+1.36}_{-1.75}$	$1.17^{+0.68}_{-0.61}$	$1.53^{+0.74}_{-0.84}$	$1.02^{+0.73}_{-0.63}$	$2.68^{+0.83}_{-0.86}$	$1.12^{+0.78}_{-0.92}$	$2.65^{+0.8}_{-0.64}$

tinuum properties is not artificial (see section 4.4 for details).

As discussed earlier, we start with the simplest model, i.e., an absorbed powerlaw model widely used to fit spectra for X-ray binaries and ULXs. When we keep the N_H parameter linked between different epochs, the best-fit value of N_H is $0.18 \pm 0.02 \times 10^{22} \text{cm}^{-2}$. In this case, the wide range variation of Γ still holds (see table 4.2). We also find variations in the measured absorbed and unabsorbed luminosities in different epochs. The highest absorbed luminosity is ~ 3 times more than the lowest absorbed luminosity of the source.

We also explore the thermal component models to justify the ULX1 spectra. We find that a single component MCD, i.e., diskbb model, is not a good descrip-

tion for the simultaneous spectral fit ($\chi^2/d.o.f = 932/540$). We then explore the widely used two-component model composed of a `diskbb` and a `powerlaw` component. We find that this combination of `diskbb` and `powerlaw` component model gives a significantly improved statistical fit compared to a single component `powerlaw` fit. The temperature of the disk component remains statistically consistent within 90% confidence in all epochs. Therefore, we eventually link this parameter for different epochs and let it vary globally. Compared to the single component `powerlaw` model fit, the `diskbb+powerlaw` model provides a much better fit ($\Delta\chi^2 \simeq -68$ for 8 less degrees of freedom). Even though the cool disk component significantly contributes to the softer regime of the spectra (see the model components in figure 4.3), the variation in photon indices still prevails in this two-component model combination. Also, interestingly, we find that the epochs XM2 and XM4, which have exhibited hard spectra, show a trend that they have comparatively more ratio of powerlaw flux and disk flux ($\frac{F_{pl}}{F_{disk}}$) than the other epochs, which have softer spectra (see table 4.3).

We also explore another widely used two-component model, which is composed of two thermal components, i.e., two temperature disk blackbody components (`diskbb+diskbb`; [Gúrpide et al. 2021a](#); [Koliopanos et al. 2017](#)). Nevertheless, the statistical fit with these two `diskbb` components in some cases provides unphysically high uncertainties in the hotter disk component parameter. This could partly be due to any degeneracy between different spectral parameters. Hence, we do not explore this model in further detail within the current limitation of data. Indeed, it is essential to mention that future on-axis and long exposure observations of this source could be useful to constrain such a model properly.

For the analyzed XMM-Newton data, we consider that the two-component model `diskbb+powerlaw` is the best-fit model combination, providing a good statistical fit of ULX1 spectra in all epochs. Figure 4.3 depicts the spectra and residuals for all XMM-Newton epochs, as well as the additive model components for the best-fit model combination. In table 4.2 and 4.3, the spectral parameters are listed for the `powerlaw` and `diskbb+powerlaw` models, respectively.

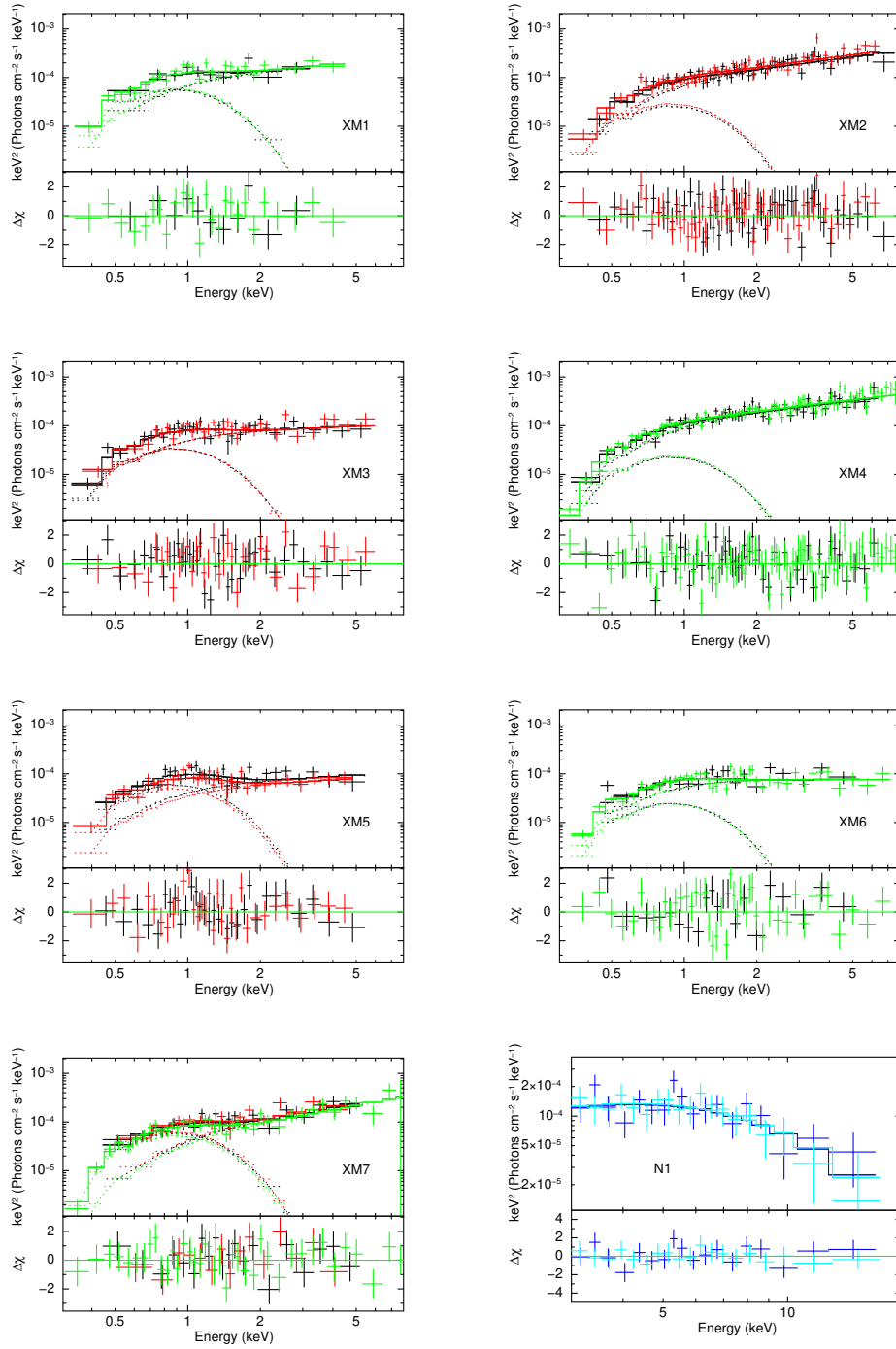


Figure 4.3: The spectra and residuals are shown for all XMM-Newton and NuSTAR observations. The `diskbb+powerlaw` model is considered for XMM-Newton epochs, and the `cutoffpl` model is considered for the NuSTAR observation. The black, red, and green colors correspond to MOS1, MOS2, and pn, while blue and light blue colors correspond to FPMA and FPMB data, respectively. The corresponding additive models are also shown in the top panels of each figure.

We have also analyzed the new 2021 NuSTAR data apart from the archival XMM-Newton observations, primarily to explore the ULX1 spectral properties in the hard energy band. Unfortunately, the simultaneous counterpart of the soft energy observation by NICER is completely dominated by the background. Therefore, the NICER data is not useful for any purposeful scientific analysis. Since the soft counterpart is unavailable, the NuSTAR spectra are fitted with absorption N_H fixed to the best-fit values taken from XMM-Newton fits.

First, we fit an absorbed powerlaw model with N_H fixed to $0.18 \times 10^{22} \text{ cm}^{-2}$ (from the XMM-Newton spectral fit) and find that $\chi^2/d.o.f = 32/34$ with $\Gamma = 2.74_{-0.20}^{+0.21}$, which is a statistically acceptable fit suggesting that the current NuSTAR data are broadly consistent with a simple powerlaw model. However, we find that an exponential cutoff powerlaw model (cutoffpl) instead of powerlaw provides a lower χ^2 value ($\chi^2/d.o.f = 21/33$). Nevertheless, the photon index is found to have a large error bar ($\Gamma = 0.14_{-1.65}^{+1.39}$), including a negative value in the lower error and an unconstrained normalization ($< 15.64 \times 10^{-5}$) with a folding energy value of $E_{fold} = 2.45_{-0.98}^{+2.86}$ keV, due to limited S/N of the data. Hence, we keep the photon index of the cutoffpl model fixed to 0.59, a typical value found in pulsar ULXs (see [Walton et al. 2020](#)). The fit remains statistically similar to the case of a free photon index. The $\chi^2/d.o.f = 21/34$ with folding energy at $E_{fold} = 2.96_{-0.33}^{+0.39}$ keV.

Caution is needed when treating this folding energy value compared to other ULX sources. Due to the unavailability of the simultaneous soft counterpart data, the cutoffpl parameters, including the photon index, are not well determined. Nevertheless, the turnover in the NuSTAR spectra is apparent from figure 4.1. One crucial comparison with the XMM-Newton data is that we could not detect the cutoff in any XMM-Newton observation when fitted with this cutoffpl model. In fact, there is no statistical improvement compared to simple powerlaw fit, and the folding energy is unconstrained. However, 2021 NuSTAR data detect the cutoff, although at the low energy threshold of NuSTAR. The unabsorbed flux in 3.0–20.0 keV energy range is $(2.49_{-0.29}^{+0.30}) \times 10^{-13} \text{ erg s}^{-1} \text{ cm}^{-2}$ and corresponding luminosity is $(1.06_{-0.12}^{+0.13}) \times 10^{40} \text{ erg s}^{-1}$. The NuSTAR spectra are plotted in figure 4.3 (last panel). We performed another exercise to provide statistical justification for the observed spectral turnover by fitting the NuSTAR

data with a broken powerlaw model following the work by [Stobbart et al. \(2006\)](#). We find that the $\chi^2/d.o.f = 19/32$ and the break energy is $E_{break} = 6.64_{-1.24}^{+1.98}$ keV, with power law photon index for $E < E_{break}$ is $1.98_{-0.60}^{+0.49}$ and for $E > E_{break}$ is $4.0_{-0.77}^{+2.49}$. This statistically validates the observed spectral break in the NuSTAR data. Here, we would mention that although the powerlaw model is a good fit to the NuSTAR data, the apparent spectral cutoff observed in figure 4.1 in accordance with other ULX broadband spectra, and similar statistical fit with both cutoffpl and broken powerlaw models favor the interpretation that the spectral cutoff in this ULX is detected with NuSTAR data.

4.3.2 | Timing Analysis

The time series analysis of NGC 1042 ULX1 shows that the light curves are steady for all XMM-Newton and NuSTAR observations. The background-subtracted source light curve for FPMA is plotted in figure 4.4. We use the HENDRICS software ([Bachetti 2018](#); [Huppenkothen et al. 2019](#)) to search for pulsation in the pn data of four XMM-Newton observations by implementing the HENZsearch tool with the fast folding algorithm.

The search was restricted to the frequency range of 0.1–6.8 Hz and the energy range of 0.3–8.0 keV. There is no detection of pulsation in any observation. The upper limits on the pulsed amplitude for all four epochs range between ~ 20 –40% (in 90% confidence interval). Since NuSTAR data provides hard energy photons, and pulsations are often stronger in the hard energy band, we utilize the new NuSTAR data for searching pulsation with a similar method within the 0.1–10.0 Hz frequency range and 3.0–20.0 keV energy range. However, we do not detect any pulsation here either, which could be due to the low S/N of NuSTAR data. The upper limit of pulsed amplitude is $\sim 40\%$.

4.4 | Discussions

This chapter focuses on studying a highly luminous and variable ULX source, NGC 1042 ULX1. A sample of extremely bright ULX sources, including NGC

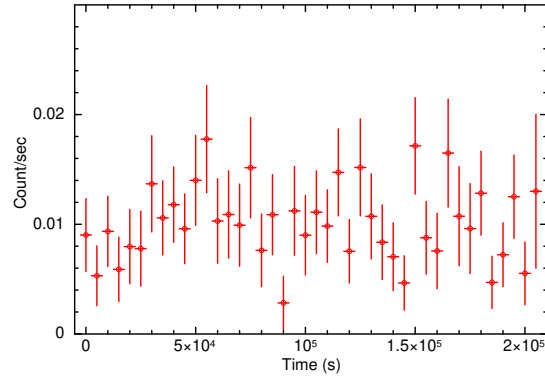


Figure 4.4: A representative plot of the background subtracted cleaned 3.0–20.0 keV light curve from NuSTAR FPMA with a 5000 seconds binning.

1042 ULX1, was studied by [Sutton et al. \(2012\)](#). Based on the analysis of three archival XMM-Newton observations and one Chandra observation, [Sutton et al. \(2012\)](#) discussed both sub-Eddington accretion onto the IMBHs and super-Eddington accretion onto stellar-mass compact objects are possible scenarios for ULX1. However, the IMBH scenario was preferred due to the apparent absence of soft excess and characteristic spectral cutoff in the XMM-Newton data. Nevertheless, it is essential to consider that spectral curvature in NGC 1042 ULX1, which is not constrained from any XMM-Newton data, could be owing to the low S/N of the data (see the discussion of [Sutton et al. 2012](#)). However, the current analysis of XMM-Newton and NuSTAR provides more detailed insight into the source, which is thoroughly discussed in this section.

4.4.1 | Accretion states of NGC 1042 ULX1

It is imperative to compare the accretion state of any individual ULX with the known ULX spectral states (e.g., [Gúrpide et al. 2021a,b](#); [Kaaret et al. 2017](#); [Sutton et al. 2013](#)) from the study of its spectral properties. The interpretation of the relative contribution of soft and hard components suggests that the NGC 1042 ULX1 spectra indicate similarity with the spectra of ultraluminous state sources. The spectral hardness in terms of the photon index value suggests that

the source mostly resembles the HUL regime, although, in some epochs, the error on the photon index extends to the SUL regime. Owing to the limitation of available XMM-Newton data quality, it would be difficult to rule out the degeneracy between the soft thermal disk component and hard powerlaw component, manifested by the somewhat large measurement uncertainties in the spectral parameters. Nonetheless, the variability in spectral profile for different epochs of observation is evident from figure 4.1, figure 4.3 and the quantified results noted in table 4.2 and 4.3.

Another critical point of our analysis is that the differences in spectral nature in different epochs are more prominent beyond ~ 1 keV. Other ULXs, like NGC 1313 X-1, NGC 55 ULX1, Holmberg IX X1, M51 ULX8, NGC 4395 ULX1 (Ghosh et al. 2022; Gúrpile et al. 2021a; Middleton et al. 2015a; Sutton et al. 2013; Walton et al. 2020) have also shown such interesting behavior. Generally, it can be understood as a physical scenario where there is no significant variation in the cool emission component in different observations, but the hot emission counterpart shows variability. Typically, when the accretion rate reaches the Eddington limit, the optically thick wind is expected to launch down the spherization radius, which would eventually manifest as a cool thermal disk blackbody-like component in the spectra. The powerlaw component, on the other hand, is an approximation of hot inner accretion flow modified by a Comptonization process, which is a dominant emission mechanism in several ULXs (see, e.g., Pinto et al. 2017; Urquhart & Soria 2016; Walton et al. 2020). Current data do not allow us to constrain a more complicated treatment of the Comptonization model like the `comptt` model component. However, if the Comptonization process indeed dominates the hard spectrum, then the variation of the powerlaw model in different epochs would indicate a variation in up-scattered photon fraction in these epochs of observation. The reason is that spectral hardness for a Comptonization process directly depends on how many photons are up-scattered from the disk seed photons and manifested as hard spectral components. Also, the soft `diskbb` component temperature of ULX1 remains consistent in different epochs within the $\sim 90\%$ confidence interval. This finding suggests that the hard component is the origin of such spectral variability, i.e., either variability in the inner accretion flow or contribution from the Comptonization process.

Gúrpide et al. 2021a,b studied spectral variability in a sample of ULX sources and discussed some possible physical scenarios that could be responsible for such variabilities. A critical aspect of super-Eddington accretion inflow is that a strong radiatively driven outflow is generated down the spherization radius due to the high accretion rate onto stellar-mass accretors. Such outflow can be optically thin or thick depending on whether the inclination angle of the system is low or high, respectively (Gúrpide et al. 2021a; Poutanen et al. 2007). Hence, the probability of hard photons dominating the line of sight emission would be enhanced for a low disk inclination system. On the contrary, for a higher inclination angle system, the hot inner region of the disk would be shrouded, most of the hard photons would be down-scattered by the optically thick wind, and thus soft emission would dominate the spectrum. Thus, changes in inclination would imply the variation in the occultation of the inner region of the disk, which would imprint the variability in the hardness of the observed spectrum.

Additionally, the spectra of NGC 1042 ULX1 show a negative correlation between luminosity and spectral photon index (see figure 4.5 and section 4.4.3), which means that the source exhibits harder spectra when it is in a higher luminosity state. A possible explanation is that the hard photons are aligned to the line of sight through the optically thin tunnel. When the accretion rate is higher in the inner region of the accretion disk, which would also correspond to a higher luminosity, the hard (hot) photons would reach us. Thus, it can be interpreted that, in general, NGC 1042 ULX1 is a low inclination system where the outflowing wind is optically thin. Therefore, an increase in accretion rate does not ensure that the hard photons would be down-scattered and move out of the line of sight. On top of that, geometrical collimation or beaming would play an essential role in explaining such luminosity-spectral hardness relation. The hard emission, which primarily originates from the inner accretion flow, is significantly beamed toward the line of sight through the optically thin tunnel. Hence the hard emission would be more intensified compared to the softer component with increasing accretion rate (e.g., King 2009; Luangtip et al. 2016; Middleton et al. 2015a; Poutanen et al. 2007).

Considering the black hole and neutron star scenarios is crucial while discussing the Comptonization process in ULXs. For a non-magnetic system, this

Comptonization could be external Comptonization in the Corona region due to inverse-scattering, or if the source is a strongly magnetized neutron star, it could be a magnetized Comptonization due to shock formation in the polar region. It is also a common assumption that the hard sources are strongly magnetized neutron star systems where the emission directly comes from the accretion column (Gúrpide et al. 2021a).

4.4.2 | Nature of the accretor

We could not confirm any detection of pulsation candidates in the source using the acceleration search technique in the Fourier space of the time series. Therefore, it is not possible to conclude whether ULX1 hosts a neutron star or a black hole. It is interesting to compare the spectra of NGC 1042 ULX1 with the spectra of known pulsating ULXs (PULXs) and sources that show similar properties like PULX spectra (see, e.g., Pintore et al. 2017; Walton et al. 2018a). The spectral curvature, which is apparently missing in XMM-Newton data, is clearly visible in the 2021 NuSTAR data. Such confirmation of spectral curvature similar to other ULX sources recognizes ULX1 as a super-Eddington accreting source. Our analysis shows the presence of a cool accretion disk component with a characteristic temperature similar to the ultraluminous state sources described in Sutton et al. 2013. Moreover, the presence of characteristic spectral curvature is confirmed by the current analysis of the data. Therefore, based on these findings, it is possible to discard the notion of ULX1 as a sub-Eddington IMBH system in a low/hard state. The best interpretation regarding the nature of the compact object within the limitation of currently available data is that ULX1 spectral characteristics are similar to that of ultraluminous state sources, which indicates that ULX1 is a super-Eddington accretor (either a stellar-mass black hole or a neutron star).

4.4.3 | Anti-correlation between $\Gamma-L_X$

The correlation studies of different spectral parameters like Γ and L_X are explored for X-ray binaries (e.g., Yang et al. 2015) and ULXs (e.g., Kajava & Poutanen 2009). Such correlation information has broader implications for under-

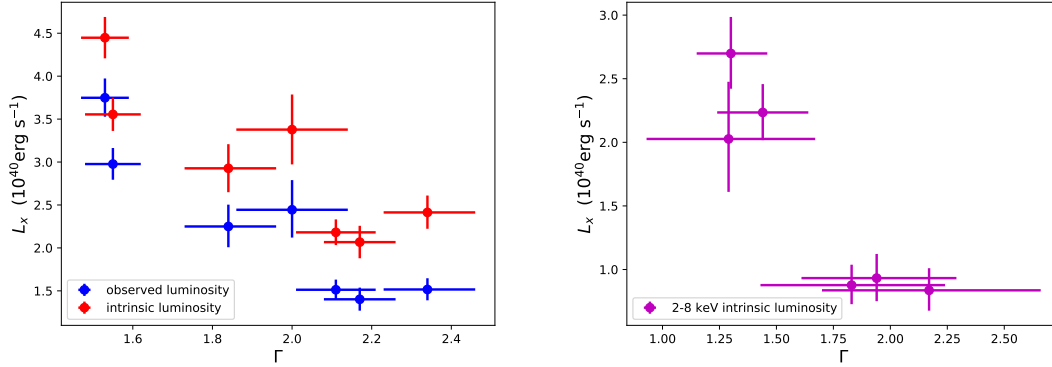


Figure 4.5: Negative correlation between Γ – L_X for different XMM-Newton epochs for 0.3–8.0 keV energy range (Left). The same quantities are plotted on the right side also but for a 2.0–8.0 keV energy range.

standing a complete picture of the physical accretion processes in these sources. A similar study for NGC 1042 ULX1 is warranted. Hence, in figure 4.5, we plot the relation between luminosity and spectral photon index. We find a negative correlation for these two parameters and discuss the theoretical notion. Before that, it is important to discuss possible “artifacts” which can arise from the absorption and low-energy thermal components.

We study the correlation properties for powerlaw fit in both cases when the absorption parameter is left free to vary for all epochs and linked between different epochs. The anti-correlation between Γ and L_X prevails in both scenarios. In fact, in all cases, the unabsorbed and the absorbed luminosities are negatively correlated with Γ . Broadly, this negative correlation between Γ and L_X is not influenced by the absorption parameter, as shown in figure 4.2. Nevertheless, caution is necessary when interpreting such correlation between Γ and N_H , where a slightly lower N_H trend is seen when the spectra are harder, i.e., Γ is lower. The Pearson r-coefficient² is ~ 0.77 with p-value ~ 0.04 and the Spearman correlation coefficient³ is ~ 0.73 with p-value ~ 0.06 . The p-values indicate the probability of getting the same correlation outcome from a completely uncorre-

²<https://docs.scipy.org/doc/scipy/reference/generated/scipy.stats.pearsonr.html>

³<https://docs.scipy.org/doc/scipy/reference/generated/scipy.stats.spearmanr.html>

lated system. In other words, typically, if $p > 0.05$, the correlation might have occurred by chance and cannot be considered statistically significant. Although no statistically significant correlation can be established between N_H and Γ , we will continue discussing two possibilities for such a trend. First, the degeneracy between the parameters of the powerlaw model and softer spectral components can give rise to such correlation since the extension of the powerlaw model in the lower energy range is arbitrary. Another possibility could be that the N_H - Γ correlation is indeed physical. When the accretion rate is higher, luminosity also increases, and from the analysis, we find a trend of increasing hardness in the system. Owing to the low inclination of the disk, the beamed hard photons pass through the optically thin tunnel and align with the line of sight. Hence, the neutral N_H component is apparently less dominant when the source is in a harder spectral state. In either case, the anti-correlation between Γ and L_X is significant and can be perceived as real.

When the absorption parameter is linked, we estimate the correlation coefficients between Γ and L_X . The Pearson r-coefficient for absorbed luminosity is ~ -0.921 with p-value ~ 0.003 , and the Spearman correlation coefficient for the same is ~ -0.857 with p-value ~ 0.014 . On the other hand, for unabsorbed luminosity, the Pearson r-coefficient is ~ -0.857 with a p-value is ~ 0.014 , and the Spearman correlation coefficient is ~ -0.857 with p-value ~ 0.014 (see figure 4.5 - left). Therefore, both absorbed and unabsorbed luminosity are negatively correlated with the powerlaw index, suggesting this property is intrinsic to the source.

With a more conservative approach, we also study the correlation property by removing any “artifact” from the soft energy regime apart from the neutral absorption. Thus, a correlation trend between 2.0–8.0 keV intrinsic L_X and Γ (figure 4.5 - right) is inspected. This approach estimates the correlation trend only in the high energy spectrum by minimizing any artificial boost in the luminosity of the soft energy part. With this motivation, we fit the data in the 2.0–8.0 keV range with an absorbed powerlaw model by fixing the N_H to the best-fit value from 0.3–8.0 keV fit. The negative correlation between L_X and Γ still holds even though the measurement uncertainties are large due to lower count statistics. Particularly, observation XM1 has very low count statistics in the 2.0–8.0

keV energy range; hence, the measurement errors are very high. Therefore, this observation is not considered in figure 4.5 - right. In this figure, the Pearson r-coefficient is ~ -0.922 , and the p-value is ~ 0.009 . The Spearman correlation coefficient, on the other hand, for the same data points, is ~ -0.771 , and the p-value is ~ 0.072 . It is crucial to point out that the Pearson and Spearman correlation coefficient measurements need to be treated with caution owing to the low sample space, and in addition, these measurements do not consider the uncertainties in the parameters.

Understanding the underlying theoretical interpretation for the appearance of such anti-correlation properties is essential. First, we compare with the results and interpretation of Yang et al. (2015) in the context of XRBs in general. The systems studied in Yang et al. (2015) have very low Eddington ratio ($\frac{L_X}{L_{Edd}}$ varying between $\sim 10^{-8.5}$ to $10^{-1.5}$). Thus, it is necessary to take a careful approach while explaining similar properties in super-Eddington sources like ULXs. Nevertheless, such an interpretation of the underlying physics is exciting and can possibly be formally invoked in future studies of ULXs. In the context of XRBs, the negative correlation between luminosity and spectral photon index is attributed to the Type I luminous hot accretion flow (LHAF) in systems where the accretion rate is high but not too high that the accretion time scale is shorter than the growth time scale of thermal instability. Unless the density is too low, the electrons in the plasma would be radiatively efficient, which means total luminosity can be approximated as the hard luminosity (L_{hard}). During a higher accretion rate, soft luminosity (L_{soft}) will not sufficiently increase since the synchrotron absorption depth would increase. This would lead to the negative correlation between L_X and Γ . As mentioned earlier, the super-Eddington accretion interpretation is a much more feasible scenario in the case of NGC 1042 ULX1, a possible stellar-mass system. Thus, the above interpretation needs to be treated with caution. Nonetheless, the increasing synchrotron absorption depth with increasing accretion rate could still be an intriguing physical mechanism that can explain the negative $\Gamma-L_X$ correlation.

The negative correlation between Γ and L_X can also be interpreted in light of the Compton scattering process. When the accretion rate is higher, i.e., luminosity is also higher, a higher Compton up-scattering photon fraction would

increase the spectral hardness. For example, in a pulsar system, the pressure and electron density increase when the mass accretion rate increases. Due to these effects, the optical depth becomes higher, increasing the $y = \frac{\tau k_B T_e}{m_e c^2}$ parameter in the Comptonization process. Thus the higher fraction of Compton up-scattered photons manifests as a harder spectrum due to a higher accretion rate (see, e.g., [Malacaria et al. 2015](#) and references therein). However, this interpretation is mainly valid for sub-critical sources as mentioned in [Malacaria et al. 2015](#). Nevertheless, we argue that, since the broadband study of many super-Eddington ULX sources (e.g., [Kaaret et al. 2017](#); [Walton et al. 2020](#)) predicts a strong contribution of Compton scattered photons in the hard spectral regime, the above explanation of harder spectrum due to higher Compton up-scattered photons with increasing accretion rate is also feasible for super-critical sources.

Let us consider a direct context of modern interpretations of ULX spectral properties. This appearance of a harder spectrum when the source is brighter can be interpreted as the geometric beaming of hard photons directly to the line of sight, as explained in section 4.4.1. In addition, for neutron star systems, the hard spectrum is often interpreted as the emission from the strong accretion column (e.g., [Gúrpide et al. 2021a](#); [Pintore et al. 2017](#); [Walton et al. 2018a](#)). The relative contribution of variation in accretion rate and magnetic field strength would determine the physical length scales of the system, i.e., the magnetospheric radius R_M and spherization radius R_{sph} . The contribution of the accretion column in the observed spectrum would be stronger if R_M truncates the disk close to the R_{sph} (see [Walton et al. 2018a](#)). Hence the spectra will eventually be harder. This would imply that the hard emission directly coming from the accretion column would be a key factor for the increase in luminosity. In fact, the observed trend in table 4.3 suggests that the harder spectral epochs like XM2 and XM4 have increased flux in the powerlaw component, which eventually supports this physical scenario of hard emission directly coming from the accretion column.

In summary, NGC 1042 ULX1 is a bright ULX, the luminosity of which reaches a few times $\sim 10^{40}$ erg s⁻¹. The spectral properties established from the analysis of XMM-Newton and NuSTAR observations indicate that the source resembles the characteristics of a stellar-mass super-Eddington accretor. The source exhibits variability in luminosity and spectral hardness which is possibly related

to the change in accretion rate, varying strength of Compton scattering, or disk occultation. In future studies, the energy-dependent variability in the source beyond ~ 10 keV can be monitored by broadband X-ray observations which can shed light on the accretion state of the source in a more comprehensive form.

Synchrotron cutoff in ULXs

This chapter is based on the results that appeared in the literature as Synchrotron Cutoff in Ultraluminous X-Ray Sources, Ghosh T., Sethi S., Rana V., 2023, ApJ, 948, 62 (Ghosh et al. 2023); arXiv:2210.02682

5.1 | Prologue

Broadband spectral analysis from the highest S/N observations has unequivocally confirmed that most of the ULXs (if not all) display a unique spectral curvature at energies $\simeq 10$ keV (e.g., Bachetti et al. 2013; Rana et al. 2015; Walton et al. 2013, 2014, 2015a,b; West et al. 2018). This spectral feature is one of the unique traits of ULXs compared to the hard state of Galactic XRBs and AGNs. Since the discovery of the first neutron star ULX (Bachetti et al. 2014), the perception regarding the nature of the compact object has been revolutionized. In a modern-day view, a foremost conjecture is that a large fraction of the ULX population is neutron stars (e.g., King & Lasota 2016, 2020; King et al. 2017).

Recent studies predict some theoretical models of emission mechanisms in ULXs that can explain the origin of such high luminosity from neutron stars (e.g., Mushtukov et al. 2019, 2017, 2015, 2018). However, there is no compelling theoretical model that can explain the origin of the unique spectral cutoff in these sources. A few phenomenological scenarios have been explored in some of the recent observational studies where emission components like Compton scat-

tering in the coronal region in low magnetic sources like black holes or comptonization occurring in the accretion column in highly magnetized neutron stars (see, e.g., [Walton et al. 2018a, 2020](#); [West et al. 2018](#)) can explain the high energy emission feature in ULXs including the cutoff. Since most ULXs observed with broadband X-ray data confirmed this unique feature, a common physical origin of such spectral cutoff could be a feasible reality. In this chapter, we propose an alternative theoretical model to explain the observed spectral cutoff based on the first principle of synchrotron radiation from different latitudes. We primarily explore possible scenarios of this phenomenon in the context of ULXs and estimate physical parameters related to both the luminosity and the spectral cutoff in ULXs. We also discuss the possibility of extending this model in the context of other sources like XRBs.

One of the most prevalent radiative processes in the context of astrophysical systems is synchrotron radiation ([Rybicki & Lightman 1979](#)). The non-relativistic case of synchrotron radiation is cyclotron radiation, where the spectrum becomes discrete. However, the emission yields a near-continuum spectrum for relativistic particles due to the predominant contribution from the higher harmonics in the observed spectrum (see [Landau & Lifshitz 1975](#); [Rybicki & Lightman 1979](#) for a review). The synchrotron radiation process in astrophysical contexts is well explored in multiple wavelengths, including soft to hard X-rays (e.g., [Heinz 2004](#); [Kisaka & Tanaka 2017a,b](#); [Longair 2011](#); [Maccarone 2005](#); [Markoff et al. 2005](#); [Riegler et al. 1970](#)). In this chapter, we study the impact of high-latitude, optically thin, classical synchrotron emission on the radiation spectrum for a large range of speeds of the charged particles. Our study encompasses a broad range from semi-relativistic to ultra-relativistic electrons.

We arrange the structure of this chapter as follows. First, we briefly review the underlying physics of synchrotron radiation relevant to our work in section 5.2. In section 5.3, we also provide a detailed calculation to obtain the approximate analytical expressions that construct the framework to understand the emission from semi-relativistic to highly relativistic electrons for a range of latitudes. We discuss the pre-processing method of the data used in the chapter in section 5.4. The main results are presented in section 5.5. In section 5.6, we provide a comprehensive summary of our findings, discuss the importance of

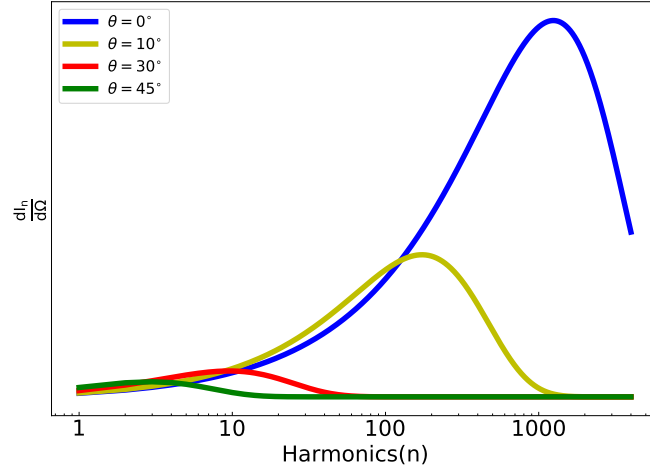


Figure 5.1: The synchrotron spectra are shown as a function of multipoles (Eq. (5.1)) for different latitudes. The $B = 5 \times 10^{11}$ Gauss and $\gamma = 10$ is used for this figure. The role of high-latitude emission in introducing spectral curvature is seen. For a fixed B and γ , the spectral cutoff shifts to a lower harmonic due to high-latitude emission.

this new theoretical model in the context of ULX systems, and discuss possible methods to distinguish our proposed model from other models.

5.2 | Synchrotron radiation: fundamentals

We assume a geometric construct in which, close to the surface of a neutron star, incoherent synchrotron radiation originates. Typically, the length scale of magnetic field lines is much larger than the curvature of the gravitating body. Thus, it is prudent to assume that the magnetic field lines are straight on the scales from which the observed synchrotron emission occurs. Without loss of generality, we assume that the magnetic field is in the z -direction of Cartesian geometry, and the charged particles move in a circular motion around the uniform magnetic field lines in the xy plane.

For a single electron, the angular distribution of the radiated power (erg sec^{-1}) per unit solid angle ($d\Omega$) in the n th harmonic (or an angular frequency

of observation, ω) can be expressed as (Landau & Lifshitz 1975):

$$dI_n = \frac{e^2 \omega^2}{2\pi c} \left[\tan^2 \theta J_n^2(n\beta \cos \theta) + \beta^2 J_n'^2(n\beta \cos \theta) \right] d\Omega \quad (5.1)$$

Here $\beta = v/c$, B is the magnetic field strength, and θ is the angle between radiated emission and the orbital plane of the particle. $J_n(x)$ is the Bessel function and $J_n'(x)$ is its derivative. The discrete energy levels of the electron's energy are denoted by integer n where $\omega = n\omega_B$. $\omega_B = eB/\gamma m_e c$, $\gamma = 1/\sqrt{1-\beta^2}$ is the relativistic boost, e and m_e are the charge and mass of the particle, respectively.

Our study aims to analyze the emission from both semi-relativistic and ultra-relativistic plasmas. Eq. (5.1) allows the transition from the cyclotron to synchrotron radiation. Suppose the argument of the Bessel functions is small, $\beta \ll 1$. In that case, the emission is dominated by low multipoles, $n \simeq 1$ (cyclotron radiation with most of the radiation occurring at $\omega \simeq \omega_B$). As the argument of Bessel functions approaches unity, the contribution of higher multipoles increases. In the ultra-relativistic case with $\theta \simeq 0$ (emission close to the plane of rotation), the emission is dominated by multipoles $n \lesssim \gamma^3$, with an exponential cutoff at large frequencies. For $\gamma \gg 1$, the spectral gap between successive multipoles $\Delta\omega = \omega_B \ll \omega$, and the emission spectrum is near-continuum (synchrotron radiation). We discuss the case of non-zero θ below.

Eq. (5.1) gives the synchrotron spectrum for a single electron of energy $E = m_e c^2 \gamma$. In reality, it is prudent to consider a range of electron energies. Thus, we assume a distribution of electron's energy with an exponential cutoff powerlaw $f(\gamma) = N\gamma^{-p} \exp(-\gamma/\gamma_{max})$ in the range γ_{min} and γ_{max} (e.g., Reynolds & Keohane 1999). The overall normalization is given by N . In this work, the minimum relativistic boost γ_{min} is treated as a free parameter, and the maximum boost $\gamma_{max} = 1000\gamma_{min}$ is considered. We assume the energy spectral index $p = 2.2$, consistent with the shock acceleration mechanism (e.g., Allen et al. 2001). We find that, in our analysis, if the γ_{max} is larger than γ_{min} by more than a few factors of 10, its impact on our results is negligible. The factors needed for conversion to flux units for comparison with the data are absorbed in the definition of N : $N = \rho_N V / D^2$, where ρ_N is the number density of relativistic electrons, V is the volume of the emitting region, and D is the luminosity distance to the source.

As noted above, the transition from the cyclotron to synchrotron radiation can be analytically understood from Eq. (5.1). When the relativistic boost γ is large, the emission is dominated by large n and is restricted to an angle $\theta \simeq 1/\gamma$ centered on the plane of the orbit. On the other hand, for semi-relativistic electrons, i.e., intermediate $\gamma \lesssim 20$, substantial emissions from higher latitudes are possible. In this chapter, we explore the possibility that the observed radiation could emanate from high latitudes with respect to the plane of the orbit. In this case, $\beta' = \beta \cos \theta$ acts as the effective velocity parameter in Eq. (5.1) and determines the frequency at which the synchrotron spectrum begins to fall exponentially. In Figure 5.1, the synchrotron spectra for different values of θ are shown. As expected, for a fixed β and B , the spectral cutoff shifts to smaller harmonics n for larger θ .

Figure 5.1 is based on the numerical evaluation of Bessel functions in Eq. (5.1). A more direct insight into the relevant physics can be comprehended with the analytic approximations of Bessel functions. In the literature, such analytic expressions have been computed for angle-averaged emission for $\beta \simeq 1$ (e.g., Schwinger et al. 1998). However, such a similar approximation is not valid in our study as the relevant parameter for us is $\beta \cos \theta$, which can deviate significantly from unity for large angles even for $\beta \simeq 1$. We find that using the stationary phase approximation, it is possible to approximate the Bessel function and its derivative in Eq. (5.1) even when β' deviates significantly from unity (Schwinger et al. 1998 employs this method in the angle-averaged case for $\beta \simeq 1$). This allows us to obtain the following approximate expressions for the Bessel function and its derivative, as discussed in the next section.

5.3 | Analytic approximation of Bessel function

We start with the integral representation of the Bessel function and their derivatives to obtain their approximate analytic expressions (e.g., Landau & Lifshitz

1975; Schwinger et al. 1998),

$$J_n(z) = \int_0^\pi d\phi \frac{1}{\pi} \cos(z \sin \phi - n\phi) \quad (5.2)$$

$$J'_n(z) = - \int_0^\pi d\phi \frac{1}{\pi} \sin \phi \sin(z \sin \phi - n\phi) \quad (5.3)$$

Here $z = n\beta \cos \theta = n\beta'$. As the integrands are highly oscillatory, the main contribution to the integrals arises from regions near $\phi = 0$ when the phase is large (stationary phase approximation). This is ensured by the condition $n\beta' \gg 1$. Expanding the phase of $J_n(z)$ around $\phi = 0$, we get:

$$z \sin \phi - n\phi = n\beta' \sin \phi - n\phi = -n \left[\phi(1 - \beta') + \frac{\beta' \phi^3}{3!} \right] \quad (5.4)$$

Making the substitution, $\phi = (1 - \beta')^{1/2} y / \beta'^{1/2}$ yields:

$$\phi(1 - \beta') + \frac{\beta' \phi^3}{3!} = \frac{(1 - \beta')^{3/2}}{\beta'^{1/2}} \left(y + \frac{y^3}{6} \right) \quad (5.5)$$

The stationary phase approximation is satisfied by the condition :

$$\frac{d}{dy} \left(y + \frac{y^3}{6} \right) = 0 \quad (5.6)$$

In this case, the stationary phase points are located at:

$$y = \pm \sqrt{2}i \quad (5.7)$$

Following the procedure outlined in Schwinger et al. 1998, in the neighborhood of the stationary phase point, we can write:

$$y = \sqrt{2}i + \zeta, \quad (5.8)$$

where ζ is real and small, which gives:

$$y + \frac{y^3}{6} = \sqrt{2}i \left(\frac{2}{3} + \frac{\zeta^2}{2} \right) \quad (5.9)$$

Thus, we can write:

$$J_n(n\beta') = \int_0^\infty dy \frac{1}{\pi} \frac{(1 - \beta')^{1/2}}{\beta'^{1/2}} \cos \left(n \left[\frac{(1 - \beta')^{3/2}}{\beta'^{1/2}} \left(y + \frac{y^3}{6} \right) \right] \right) \quad (5.10)$$

First, we consider the case when $n(1 - \beta')^{3/2}/\beta'^{1/2} \ll 1$. In this case, the main contribution to the integral comes from the region where y is large. Given that most of the contribution to the integral comes from regions where the phase is close to unity, the integration limit can be extended to infinity (e.g., [Schwinger et al. 1998](#)). Solving the resultant integral, we get:

$$J_n(n\beta') \simeq 0.447n^{-1/3}\beta'^{-1/3} \text{ for } n\frac{(1 - \beta')^{3/2}}{\beta'^{1/2}} \ll 1 \quad (5.11)$$

In the case of, $n(1 - \beta')^{3/2}/\beta'^{1/2} \gg 1$, the integral can be written as:

$$J_n(n\beta') = \text{Re} \int_0^\infty dy \frac{1}{\pi} \frac{(1 - \beta')^{1/2}}{\beta'^{1/2}} \exp\left(in(1 - \beta')^{3/2}(y + y^3/6)/\beta'^{1/2}\right) \quad (5.12)$$

Since most of the contribution arises from the vicinity of the stationary point, this can be readily integrated as

$$J_n(n\beta') \simeq 0.335n^{-1/2}(1 - \beta')^{-1/4}\beta'^{-1/4} \times \exp\left(-2\frac{\sqrt{2}}{3}n\beta'^{-1/2}(1 - \beta')^{3/2}\right) \quad (5.13)$$

Following a similar calculation procedure, we obtain the approximate forms of $J'_n(n\beta')$ also. These approximated forms are given in Eq. 5.14.

$$\begin{aligned} J_n(n\beta') &\simeq 0.447n^{-1/3}\beta'^{-1/3} \text{ for } n \leq n_c \\ J_n(n\beta') &\simeq 0.335n^{-1/2}(1 - \beta')^{-1/4}\beta'^{-1/4} \\ &\quad \times \exp\left(-2\frac{\sqrt{2}}{3}n\beta'^{-1/2}(1 - \beta')^{3/2}\right) \text{ for } n \geq n_c \\ J'_n(n\beta') &\simeq 0.411n^{-2/3}\beta'^{-2/3} \text{ for } n \leq n_c \\ J'_n(n\beta') &\simeq 0.474n^{-1/2}(1 - \beta')^{1/4}\beta'^{-3/4} \\ &\quad \times \exp\left(-2\frac{\sqrt{2}}{3}n\beta'^{-1/2}(1 - \beta')^{3/2}\right) \text{ for } n \geq n_c \end{aligned} \quad (5.14)$$

with

$$n_c \simeq \frac{\beta'^{1/2}}{(1 - \beta')^{3/2}}. \quad (5.15)$$

n_c denotes the harmonic at which spectral cutoff occurs. It is important to note that our analytical results extend the procedure outlined by [Schwinger et al. 1998](#) from the extreme relativistic case $\beta' \simeq 1$ to arbitrary β' . The analytic expressions given in Eq. (5.14) agree with numerical results to be better than 10% in the acceptable range of $\beta' \gtrsim 0.3$ (see below). Also, for $\beta' \simeq 1$ ($\beta \simeq 1$ and $\theta \simeq 0$), $1/(1 - \beta') \simeq 2\gamma^2$, and $n_c \simeq \gamma^3$ which agrees with the angle-averaged ultrarelativistic case ([Schwinger et al. 1998](#)).

Our aim in this chapter is to explain the spectral cutoff as observed in ULXs. For fitting the X-ray continuum spectral data, we require $n_c \gg 1$. This requires: $n_c \geq 1$, which gives $0.3 \lesssim \beta \lesssim 1$ and $0.3 \lesssim \cos \theta \lesssim 1$ ¹. Thus, continuum X-ray spectra constrain the latitude $\theta \lesssim 70^\circ$ and the particle's velocity $0.3c \lesssim v \lesssim c$. One can consider the intriguing possibility that the observed spectrum could arise from a set of discrete lines (though it is unlikely, as we argue below). We note that the exponential terms in Eq. (5.14) adequately capture the cutoff frequency in the entire parameter range of interest, which is key to modeling the ULX cutoff frequency. While we compute Bessel functions numerically for the purpose of data analysis, these analytic expressions are crucial for interpreting our results.

In Figure 5.1, we display synchrotron spectra for emission from different latitudes. Eq. (5.14) allows us to understand the spectral shapes seen in the figure. The spectral cutoff occurs at an angular frequency $\omega \simeq n_c \omega_B$. For emission close to the plane of the rotation ($\theta \simeq 0$), $n_c \simeq \gamma^3$. However, for larger angles $n_c < \gamma^3$, as Eq. (5.15) shows, and the spectral cutoff shifts to smaller frequencies. As we discuss later, the spectral cutoff in the data we analyze occurs at $E \simeq 10 \text{ keV}$. This cutoff can be explained for a large range of γ , B , and θ , as will be discussed below in more detail. Although we only assume the particle's motion in the plane perpendicular to the magnetic field, the qualitative description of the results would not change if the electron has a z-component of velocity. Simply, this case can be incorporated into our analysis by altering B to $B_\perp \equiv B \cos \chi$, where χ is the angle between the velocity vector and the magnetic field (e.g., [Landau & Lifshitz 1975](#)).

¹<https://www.wolfram.com/mathematica/>

5.4 | Pre-processing of data

Here, we discuss the detailed procedure of pre-processing the data used in this chapter. We have used XSPEC only to generate the flux data points from observed spectra. Finally, we performed a different fitting method for our analysis.

To find the congruence between our theoretical model and real observed data, we have selected the NuSTAR observations of two bright pulsar ULXs, NGC 5907 ULX1 (RA: 15:15:58.62, Dec.: +56:18:10.3; [Fürst et al. 2017](#); [Israel et al. 2017a](#); [Walton et al. 2015a](#)) and NGC 7793 P13 (RA: 23:57:50.9, Dec.: -32:37:26.6; [Fürst et al. 2016](#); [Israel et al. 2017b](#); [Walton et al. 2018b](#)). The distances to the host galaxies are $\simeq 17.1$ Mpc (e.g., [Fürst et al. 2017](#)) and $\simeq 3.5$ Mpc (e.g., [Walton et al. 2018b](#)), respectively. NuSTAR has observed these two sources several times in the past decade. This allows us to observe their long-term spectral evolution and inspect how the spectral parameters of the theoretical model vary over time. Since the spectral curvature happens in the higher energy range, NuSTAR is the best instrument to model the spectral curvature in the spectra of these sources. Generally, the broadband spectra of ULXs are explained with multiple components like neutral absorption, geometrically thin or slim accretion disk, and a phenomenological model of either magnetic or non-magnetic Comptonization processes (see, e.g., [Kaaret et al. 2017](#)). The neutral absorption and thermal disk components mostly play a significant role in the soft energy regime ($E \lesssim 5$ keV). This work aims to explain the spectral cutoff in ULXs with a new theoretical model, which occurs in a higher energy range ($E \simeq 10$ keV). Hence, we try to minimize contamination from soft components and adequately model the spectral break. Thus, we restrict the energy range of our analysis within $\simeq 5$ –25 keV.

Our study considers all the available NuSTAR data sets for both sources. However, there are a few observations of NGC 5907 ULX1, for which the S/N is poor due to the faintness of the source. Therefore, we do not utilize these data for our analysis. In figure 5.2, we plot the spectra from the NuSTAR observations of both sources. In particular, we detect two distinct flux states for NGC 7793 P13. Interestingly, within $\simeq 5$ –25 keV energy range, both the sources exhibit similar spectral profiles in all observations except differences in flux.

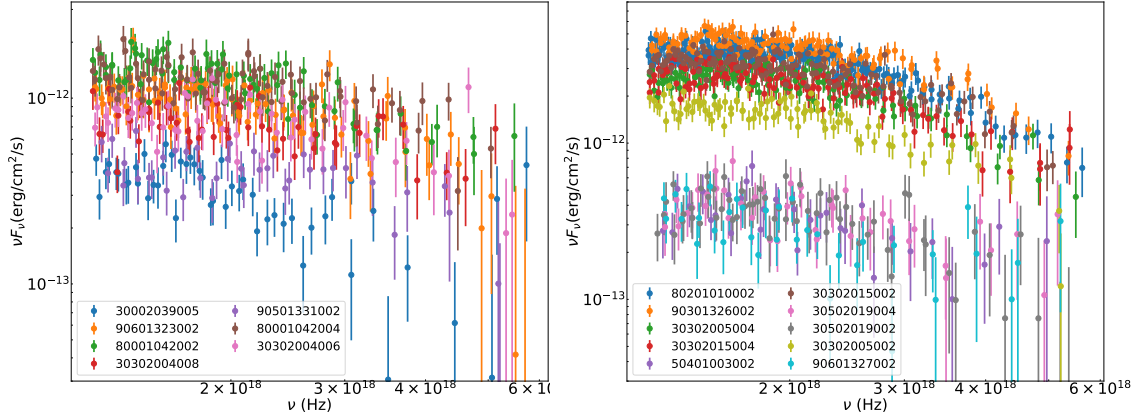


Figure 5.2: The 5–25 keV spectra of NGC 5907 ULX1 (left) and NGC 7793 P13 (right) are displayed for multiple NuSTAR observations. As discussed in the text, the spectra above ~ 5 keV show similar spectral shapes with variations in flux in different observations for both sources.

5.4.1 | Data reduction process

The NuSTAR data are extracted following the standard data reduction method explained in Chapter 2. Broadly, we follow the data reduction method specific to these two sources as outlined in previous works (e.g., Fürst et al. 2017, 2016; Israel et al. 2017a,b; Lin et al. 2022; Walton et al. 2015a, 2018b). The source photon extraction region is selected as a 50 arcsec radius circle for both sources. In all cases, a 100 arcsec radius circle is selected to extract photons from background regions. The spectra are grouped with a minimum of 30 counts per energy bin for all NGC 5907 ULX1 spectra. For NGC 7793 P13 spectra, the spectra are grouped with a minimum of 50 counts per energy bin where the source is in a high flux state and 20 counts per energy bin where the source is in a low flux state (observation IDs - 30502019002, 30502019004, 50401003002, 90601327002).

The XSPEC spectral analysis package is used to convert the spectral data points into flux units for further analysis. We find that background significantly dominates the spectra of all NuSTAR data beyond $\simeq 25$ keV. Hence, we do not utilize the spectral data above this energy for our analysis. In some low flux state observations, the background starts dominating well below $\simeq 20$ keV. Neverthe-

less, to provide a similar treatment to all observations, we consider spectra up to $\simeq 25$ keV for all cases. The NuSTAR spectra are fitted with a cutoff powerlaw model (in XSPEC, the syntax is `constant*cutoffpl`). The instrumental cross-calibration differences are represented by the `constant` model, and `cutoffpl` is used to model the exponentially cutoff powerlaw spectral continuum. We find that this model within 5.0–25.0 keV energy range gives a statistically good fit for both sources. We fix the index of the `cutoffpl` model to the value of 0.59, a typical value for ULX pulsars (see, e.g., [Walton et al. 2020](#)). The neutral absorption is not considered since it plays a predominant role only in the softer regime of the spectra. We then convert the spectral counts into flux νF_ν (erg/cm²/sec) by the `eeufspec` command and take the data points in the energy range 5.0–25.0 keV ($\simeq 1.2\text{--}6.0 \times 10^{18}$ Hz) to perform further analysis described in the section 5.5. To further verify the robustness of this data extraction procedure, instead of the `cutoffpl` model, we utilize another model, such as a simple powerlaw of photon index 0, and then extract the spectra in flux unit using `eeufspec`. We find that our results are insensitive to the choice of XSPEC models used to generate the flux data points.

5.5 | Analysis and Results

It is easy to understand that if $\beta \simeq 1$, γ and B are degenerate with each other in Eq. 5.1. As we wish to explore a range of electron speeds from semi-relativistic to ultra-relativistic, this degeneracy cannot be removed². Thus, γ_{min}/B is chosen as one of the parameters in our analysis instead of separately quantifying γ_{min} and B . Therefore, our analysis has three parameters, namely, γ_{min}/B , θ , and N . Later, one more parameter is fixed to deal with residual degeneracies. We also convert the model to νF_ν unit by appropriately scaling Eq. 5.1 by a multiplicative factor $n = \omega/\omega_B$, where $\omega = 2\pi\nu$.

² $\beta \simeq 1$ approximation is appropriate for the ultra-relativistic cases or semi-relativistic cases in higher latitudes.

For our model, the observed flux can be written as:

$$\nu F_\nu = N' \int_{x_{min}}^{x_{max}} S x^{-p} \exp(-x/x_{max}) dx \quad (5.16)$$

where $x = \gamma/B$,

$$N' = \frac{N}{\int_{x_{min}}^{x_{max}} x^{-p} \exp(-x/x_{max}) dx} \quad (5.17)$$

and,

$$S = \frac{2\pi e^2 \nu^3}{c \nu_B} \left[\tan^2 \theta J_{\frac{\nu}{\nu_B}}^2 \left(\frac{\nu}{\nu_B} \cos \theta \right) + J_{\frac{\nu}{\nu_B}}'^2 \left(\frac{\nu}{\nu_B} \cos \theta \right) \right] \quad (5.18)$$

We choose two different statistical methods, namely, the frequentist approach and Bayesian analysis, to explore the congruence of the data and the model. Since it is hard to determine the best-fit and errors on all three parameters simultaneously, we perform our analysis for fixed angle θ and keep the other two parameters $\gamma_{min}/B = x_{min}$ and N free to vary. For the frequentist approach, we first carry out a minimum χ^2 analysis using the `scipy` (Virtanen et al. 2020) “`curve_fit`” tool³. The best-fit parameters, χ^2 values, and 1σ errors (computed using covariance matrix) are given in Table 5.1. We consider three values of $\theta = 1^\circ, 15^\circ, 30^\circ$ for our analysis of each data set. As discussed in the foregoing, this choice is based on the acceptable range of latitudes to ensure $n_c \gg 1$. In Figure 5.3, we plot the data, the best-fit curve, and spectral residuals for one observation for each source.

In the Bayesian analysis, we utilize the Markov chain Monte Carlo (MCMC) method using `python emcee` package⁴ (Foreman-Mackey et al. 2013). We find the convergence of chains in each case, and the computed posterior probabilities agree with the results obtained using the frequentist method. In figure 5.4, we plot the marginalized posterior probabilities from the MCMC analysis for a subset of data. The MCMC analysis is done with 32 random walkers and 500 burn-in, and 5000 post-burn-in iterations to reach convergence. We use a combination of two moves, namely, `moves.DEMove` and `moves.DESnookeyMove` with

³https://docs.scipy.org/doc/scipy/reference/generated/scipy.optimize.curve_fit.html

⁴<https://emcee.readthedocs.io/en/stable/>

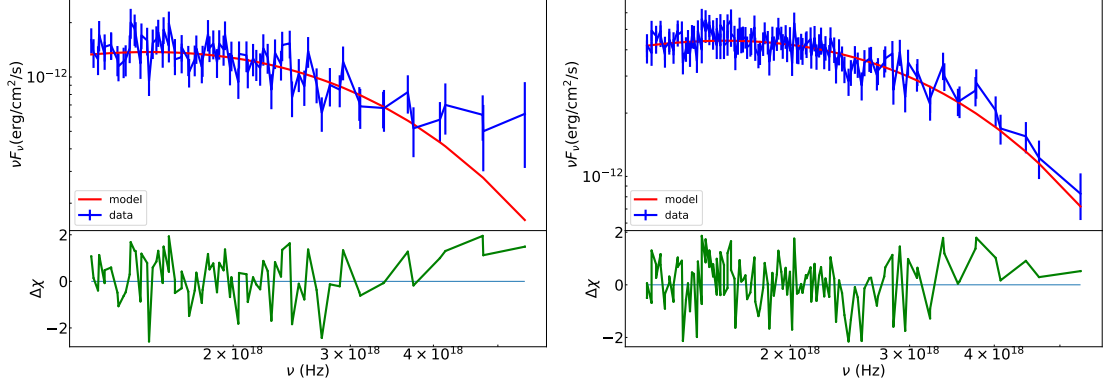


Figure 5.3: Example plots depicting the congruence of the theoretical model with the spectra of two ULXs. Each plot is shown for one observation of each source. The data with the model over-plotted are shown in the top panels, and corresponding residuals are shown in the bottom panels. The models shown here are for 1° angle in case of NGC 5907 ULX1 (left; Observation - 80001042002) and 30° angle for NGC 7793 P13 (right; Observation - 90301326002).

80% and 20% probability, respectively, at each step. These posterior probabilities represent the convergence of the chains for the given parameter sets in our analysis.

We next discuss the physical implications of the parameter range suggested by statistical analyses. We find that for fixed emission angles, the spectrum is scaled by the parameter x_{min} , and the overall amplitude is scaled by N . A particular combination of γ_{min} , B , and θ is necessary to obtain the spectral feature in the X-ray energy band. Also, our analysis suggests that the spectra are governed mainly by the particles with relativistic boost close to γ_{min} . The higher values of boost (i.e., close to γ_{max}) contribute less to the observed spectra. Interestingly, we do not find significant long-term spectral variability in the high-energy band for both sources. Thus, the parameter x_{min} remains nearly the same for all observations (Table 5.1). However, owing to the changes in flux in different observation epochs, the parameter N varies significantly.

In table 5.1, we find that the estimated range of $x_{min} = \gamma_{min}/B$ varies from $10^{-6} G^{-1}$ to $10^{-11} G^{-1}$ for the range of θ . It can be verified from the expression for $\nu_B = \omega_B/(2\pi)$ and Eq. (5.15) that the results given in Table 5.1 correspond to

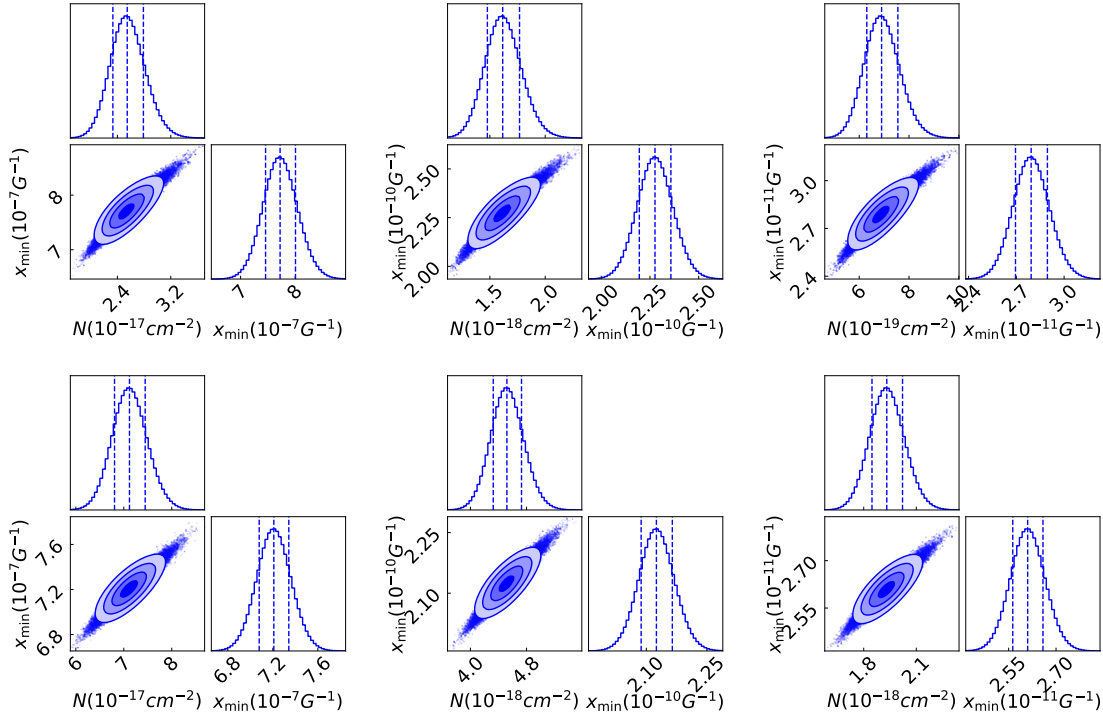


Figure 5.4: Based on the MCMC analysis described in the text, we display corner plots for two parameters N and x_{min} for emission angles: 1° , 15° , 30° (from left to right). The top and bottom panels correspond to NGC 5907 ULX1 (Observation - 80001042002) and NGC 7793 P13 (Observation - 90301326002), respectively. The 0.16, 0.5, and 0.84 quantiles are shown as vertical lines in the figures. 50 bins are used in the histograms, which are smoothed with 3σ Gaussian kernel.

a cutoff frequency of around 10 keV. The allowed range of x_{min} encompasses a large range of particle speeds and magnetic field strengths. At higher latitudes, our results are consistent with semi-relativistic electrons, i.e., $\gamma_{min} \simeq 20$ and $B \simeq 10^{12}$ G. On the other hand, for emission from close to the rotational plane of the electrons, the results are consistent with ultra-relativistic particles (i.e., $\gamma_{min} \simeq 10^5$) for the same magnetic field strength. This magnetic field strength is expected on the surface of neutron stars (e.g., [Caballero & Wilms 2012](#); [Pétri 2016](#)). Since both the relativistic electron density ρ_N and the volume of emission region V are very poorly determined, even theoretically, the overall normalization $N = \rho_N V / D^2$ is highly uncertain. Typically, in neutron star magnetosphere, the lower plasma density limit is given by the Goldreich-Julian limit

(Goldreich & Julian 1969), which depends on the pulsar spin period, magnetic field strength, and alignment of spinning axis with magnetic field line. Depending on the volume of the emission region, we find that the estimated number density could be comparable to or higher than the Goldreich-Julian limit (Goldreich & Julian 1969) for a 1 sec spinning pulsar with $B \simeq 10^{12}$ G, i.e., 7×10^{10} particles cm^{-3} . In reality, the plasma density can be significantly higher than the Goldreich-Julian limit (see Lyutikov & Gavriil 2006 and references therein). This means our results are consistent with this theoretical expectation. We also determine that the emitting region is optically thin to synchrotron self-absorption and Compton scattering for a range of acceptable parameters.

The magnetic field strength at which the quantum effects become important is the Schwinger limit $\sim 4.4 \times 10^{13}$ G. If we restrict the maximum limit of the magnetic field on the NS surface to this value, then the maximum value of γ_{min} can be estimated. For a lower x_{min} value (i.e., lower γ_{min} or higher B), we get emission at higher latitudes which requires a lower value of N to explain the observed ULX flux. On the other hand, when x_{min} is higher, we get emissions closer to the plane of orbit, and higher N is required to generate such high flux in these sources. In the future, it would be possible to constrain all the parameters adequately if we can have at least one parameter determined from other data. Our results suggest that the spectral curvature in ULXs might have a common origin of synchrotron radiation, and all the ULXs that exhibit such spectral cutoff are possibly highly magnetized neutron stars. This theoretical model can also be employed to explain the high energy cutoff in X-ray binary pulsar sources. Essentially, this model suggests that the spectral curvature is governed by plasma velocity, magnetic field strength, electron number density, and emission angle.

5.6 | Discussions

In this chapter, we focus on explaining the spectral cutoff at $E \simeq 10$ keV in ULXs. For that purpose, we choose two known bright pulsar ULXs since it is a generic feature of many pulsar ULXs to exhibit such spectral cutoff. We propose a new theoretical model of synchrotron radiation at a range of latitudes as a

Table 5.1: The results from the python curve fit with the best-fit parameters and χ^2 are listed for 7 NuSTAR observations of NGC 5907 ULX1 and 10 NuSTAR observations of NGC 7793 P13. The errors are calculated with 1- σ confidence from the covariance matrix using the parameter `absoulte_sigma=True`.

Observations	$\theta = 1^\circ$			$\theta = 15^\circ$			$\theta = 30^\circ$		
	x_{min} ($10^{-7} G^{-1}$)	N ($10^{-17} cm^{-2}$)	$\chi^2/d.o.f$	x_{min} ($10^{-10} G^{-1}$)	N ($10^{-18} cm^{-2}$)	$\chi^2/d.o.f$	x_{min} ($10^{-11} G^{-1}$)	N ($10^{-19} cm^{-2}$)	$\chi^2/d.o.f$
NGC 5907 ULX1									
30002039005	(9.54 ± 0.56)	(1.10 ± 0.18)	57/49	(2.81 ± 0.16)	(0.70 ± 0.12)	57/49	(3.45 ± 0.20)	(2.97 ± 0.49)	57/49
30302004006	(6.38 ± 0.36)	(1.00 ± 0.12)	66/52	(1.88 ± 0.11)	(0.63 ± 0.08)	66/52	(2.31 ± 0.13)	(2.72 ± 0.34)	66/52
30302004008	(5.94 ± 0.35)	(0.81 ± 0.10)	62/49	(1.75 ± 0.10)	(0.51 ± 0.06)	62/49	(2.15 ± 0.12)	(2.21 ± 0.27)	62/49
80001042002	(7.69 ± 0.27)	(2.52 ± 0.23)	80/78	(2.27 ± 0.08)	(1.60 ± 0.14)	80/78	(2.78 ± 0.10)	(6.84 ± 0.61)	80/78
80001042004	(6.57 ± 0.26)	(1.69 ± 0.15)	82/77	(1.94 ± 0.08)	(1.07 ± 0.10)	82/77	(2.38 ± 0.09)	(4.58 ± 0.41)	83/77
90501331002	(5.97 ± 0.46)	(0.47 ± 0.08)	34/39	(1.76 ± 0.14)	(0.30 ± 0.05)	34/39	(2.16 ± 0.16)	(1.28 ± 0.21)	34/39
90601323002	(7.23 ± 0.29)	(1.66 ± 0.16)	89/88	(2.13 ± 0.09)	(1.05 ± 0.10)	90/88	(2.62 ± 0.10)	(4.50 ± 0.43)	90/88
NGC 7793 P13									
30302005002	(7.66 ± 0.20)	(3.07 ± 0.20)	77/82	(2.26 ± 0.06)	(1.95 ± 0.13)	77/82	(2.77 ± 0.07)	(8.30 ± 0.55)	77/82
30302005004	(7.46 ± 0.15)	(4.58 ± 0.23)	111/117	(2.20 ± 0.04)	(2.90 ± 0.15)	111/117	(2.70 ± 0.05)	(12.40 ± 0.62)	111/117
30302015002	(7.53 ± 0.14)	(5.95 ± 0.27)	147/133	(2.22 ± 0.04)	(3.77 ± 0.17)	147/133	(2.73 ± 0.05)	(16.10 ± 0.73)	148/133
30302015004	(7.53 ± 0.17)	(4.75 ± 0.26)	130/123	(2.22 ± 0.05)	(3.02 ± 0.17)	130/123	(2.72 ± 0.06)	(12.88 ± 0.70)	130/123
30502019002	(7.41 ± 0.53)	(0.65 ± 0.11)	42/61	(2.18 ± 0.16)	(0.41 ± 0.07)	42/61	(2.68 ± 0.19)	(1.77 ± 0.30)	42/61
30502019004	(6.93 ± 0.62)	(0.57 ± 0.12)	32/42	(2.04 ± 0.18)	(0.36 ± 0.08)	32/42	(2.51 ± 0.22)	(1.55 ± 0.32)	32/42
50401003002	(7.37 ± 0.79)	(0.59 ± 0.15)	25/31	(2.17 ± 0.23)	(0.38 ± 0.10)	25/31	(2.67 ± 0.28)	(1.60 ± 0.41)	25/31
80201010002	(7.26 ± 0.10)	(6.20 ± 0.22)	156/204	(2.14 ± 0.03)	(3.94 ± 0.14)	156/204	(2.63 ± 0.04)	(16.81 ± 0.58)	156/204
90301326002	(7.20 ± 0.14)	(7.11 ± 0.33)	104/123	(2.12 ± 0.04)	(4.51 ± 0.21)	104/123	(2.61 ± 0.05)	(19.26 ± 0.89)	105/123
90601327002	(9.65 ± 1.01)	(1.00 ± 0.30)	35/34	(2.84 ± 0.30)	(0.63 ± 0.19)	35/34	(3.49 ± 0.36)	(2.70 ± 0.80)	35/34

possible physical emission mechanism to explain the observed spectral shape. Based on the analysis of 17 spectra from two PULX sources, our main results are summarized in Table 5.1. Figure 5.3 shows the fit and residual for one spectrum for each source.

Other models like the comptonization from the coronal region of a non-magnetic source and comptonization from the magnetized column in neutron stars (see, e.g., [Walton et al. 2020](#); [West et al. 2018](#)) have been explored to explain the dominant emission in hard X-ray range in ULXs. Compton scattering in the presence of a high magnetic field in neutron stars is a possible candidate to explain high luminosity in these sources ([Mushtukov et al. 2015](#)). In principle, there could be two possible ways to distinguish our proposed scenario from these models, which we discuss below.

The parameter value x_{min} indicates the possible relativistic boost of the plasma and the magnetic field strength. For example, in Table 5.1, we see that for $\theta \simeq 30^\circ$, the best-fit value $x_{min} = \gamma_{min}/B \simeq 2 \times 10^{-11} G^{-1}$. This could correspond, for instance, to a semi-relativistic electron ($\gamma_{min} \simeq 20$) along with a magnetic field $B \simeq 10^{12} G$. In such cases, the fundamental mode of emission, $\nu_B = eB/(2\pi m_e c \gamma_{min}) \simeq 600 eV$. Since this value is larger than the spectral

resolution of NuSTAR in the energy range of interest, we might observe the spectrum as a set of discrete cyclotron lines. However, it is important to understand that such an interpretation could be difficult owing to mixing with larger γ values and the width of spectral lines, which are difficult to ascertain. This would also require either re-analysis of the data or new data. Our analysis also intriguingly raises the possibility that the discreteness property of the spectrum could be a probe of the latitude of the emission. As we have already discussed in section 5.3, an upper limit on the latitude of emission can be obtained by requiring $n_c \gg 1$; this yields a stringent upper bound $\theta \simeq 70^\circ$. For fitting continuum X-ray spectral data in the energy range of interest, this requirement motivates the upper limit of $\theta \simeq 30^\circ$ we use in table 5.1.

Another possible probe of our model could be the polarization of received photons. The photons emerging from higher latitudes of synchrotron radiation would be elliptically polarized, while those from closer to the plane of the orbit would be linearly polarized. While the non-magnetic Comptonization will not show polarized emission, the magnetic Comptonization and the synchrotron radiation could display different degrees of polarization. Modern X-ray polarimeters such as the Imaging X-ray Polarimetry Explorer (IXPE; [Weisskopf et al. 2016](#)) and upcoming mission X-ray Polarimeter Satellite (XPoSAT) with X-ray polarimeter instrument POLIX ([Paul 2022](#)) might be able to address these questions.

We provide a brief summary of our main results and perspectives below:

1. We propose that classical, high-latitude and optically thin synchrotron radiation is a possible theoretical model to explain the spectral cutoff in ULXs. Typically, for standard angle-averaged and ultra-relativistic classical radiation, the cutoff occurs at energies $\gamma^3 \nu_B$ for radiation close to the plane of the orbit. However, we show that the cutoff frequency shifts to much smaller frequencies for high-latitude emission following the Eq. (5.15). Quantum effects only dominate the cutoff for energies close to the electron rest mass and hence cannot be responsible for the observed cutoff at $E \simeq 10 \text{ keV}$.
2. We utilize 17 NuSTAR spectra of two PULXs in different flux states to com-

pare with the model. The observed fluxes are theoretically modeled using four parameters. However, due to the degeneracy between parameters, we can only estimate two parameters from the data. Two different statistical approaches are carried out to test the robustness of our statistical analysis. These methods are frequentist and Bayesian analysis (using MCMC). While we find a large range of possible theoretical parameters from our analysis, the most compelling case corresponds to the high-latitude emission ($\theta \simeq 30^\circ$) from a semi-relativistic plasma from the surface of the neutron star ($B \simeq 10^{12} G$ and $\gamma \simeq 20$). We also find that the plasma is optically thin for a plausible range of parameters from our analysis.

3. Future X-ray polarization data might be useful to verify the model for different ULXs and further constrain the physical parameters with much better precision. We also discussed that the discreteness of the observed spectrum could also be a possible probe of the semi-relativistic plasma for high-latitude emission.

Super-Eddington accretion onto ULXs

This chapter is based on the results that appeared in the literature as

1. *Constraint on the Accretion of NGC 6946 X-1 Using Broadband X-Ray Data, Ghosh T., Rana V., 2023, ApJ, 949, 78 (Ghosh & Rana 2023a); arXiv:2301.09837*
2. *Super-Eddington accretion on to a stellar mass ultraluminous X-ray source NGC 4190 ULX1, Ghosh T., Rana V., 2021, MNRAS, 504, 974 (Ghosh & Rana 2021); Erratum: 2023, MNRAS, 522, 1183 (Ghosh & Rana 2023b); arXiv:2103.10265.*

In addition to the above publications, this chapter also includes results from the analysis of several other sources that are not published.

6.1 | Prologue

A population study of any astrophysical class of objects is crucial to understanding the broad picture of the underlying emission mechanism in the sources. Such studies include exploring common properties as well as differences among several sources in a particular group. A systematic study of ULXs and their distinctive groups would help probe the accretion mechanism in these mysterious sources. As discussed in the previous chapters, we studied individual ULXs and their spectral and timing properties. We also explored a new theoretical model to probe a unique spectral feature in ULXs. In this chapter, we study a few bright

Table 6.1: Sample of ULXs studied in this chapter

Sl.	ULX	RA	Dec.	spectral state	Distance (Mpc)
1	NGC 6946 X-1	20:35:00.7	+60:11:31	SUL	7.72
2	NGC 4190 ULX1	12:13:45	+36:37:55	BD	2.9
3	NGC 1291 ULX1	3:17:13.82	-41:10:34.6	BD	8.6
4	NGC 4254 X2	12:18:56.1	+14:24:19	HUL	33.2
5	NGC 4244 ULX1	12:16:56.927	+37:43:35.89	SUL/SSUL	3.6

ULX sources (see Table 6.1) with somewhat distinctive spectral features, albeit their implications converge to a common conclusion on the accretion mechanism. The sample of sources is selected based on the spectral hardness of the sources. We select the sources in a range of soft to hard spectral states and confine our study to a limited number of sources so that we can discuss different models and their implications on the accretion mechanism of these sources in detail.

Another selection criterion of these sources is based on their broad classification of ULX spectral states. Broadly, the sources belong to different states like broadened disk and ultraluminous states, and we explore their similar and dissimilar properties. First, we discuss a soft source NGC 6946 X-1 with a detailed broadband X-ray spectral study and shed light on its accretion mechanism. We then implement similar spectral modeling to other ULX sources with high-quality XMM-Newton data. Finally, we compare their spectral properties and interpret the source characteristics.

6.2 | Accretion constraint on NGC 6946 X-1

NGC 6946 is a starburst galaxy with a distance of ~ 7.72 Mpc (Anand et al. 2018). Since it is a starburst galaxy, it hosts multiple ULXs (Earnshaw et al. 2019) including NGC 6946 X-1 (RA: 20:35:00.7, Dec.: +60:11:31). In the literature, NGC 6946 X-1, is also known as ULX-3 (see Earnshaw et al. 2019 and references therein). Being one of the brightest ULX in the galaxy, the source is also known for its soft spectral nature, which has been confirmed to show emission line signatures (Kosec et al. 2021; Pinto et al. 2016) like other soft ULX sources. Here,

Table 6.2: Observation log of NGC 6946 X-1. pn data are not used for observation 0870830201, and MOS1 data are not available for observation 0870830401.

Serial No.	Observation ID XMM-Newton	Observation ID NuSTAR	Observation start date	Epoch ID	Spectral Exposure time (ksec) pn/MOS1/MOS2/FPMA/FPMB
1	0870830101	50601001002	2020-07-08	XN1	12.5/16/16/100/99
2	0870830201	50601001004	2020-12-13	XN2	-/16/16/94/91
3	0870830301	50601001006	2021-04-02	XN3	8.5/14/14/83/84
4	0870830401	50601001008	2021-05-25	XN4	12/-/16/88/89

we study its broadband X-ray spectral properties using XMM-Newton and NuSTAR data. From the analysis of continuum features, we provide some crucial constraints on the accretion mechanism in this ULX.

6.2.1 | Observation details

We analyze the simultaneous broadband data of NGC 6946 X-1 jointly observed by XMM-Newton and NuSTAR in 2020-2021. Using archival XMM-Newton and NuSTAR data, the source has been previously analyzed in detail (see, e.g., [Earnshaw et al. 2019](#); [Hernández-García et al. 2015](#); [Kajava & Poutanen 2009](#); [Kosec et al. 2018a, 2021](#); [Middleton et al. 2015a](#); [Pintore et al. 2017](#); [Qiu & Feng 2021](#)). The readers are directed to these papers for an overview of the previous analyses. Here, we focus on the 2020-2021 joint observations by XMM-Newton and NuSTAR. Previous joint XMM-Newton and NuSTAR observation data taken in 2017 were analyzed in [Earnshaw et al. 2019](#) in detail. Therefore, we compare the results from 2020-2021 broadband data to those obtained in [Earnshaw et al. 2019](#) and emphasize the new findings, which are compelling owing to the multiple simultaneous broadband X-ray observations of the source. The observations for NGC 6946 X-1 used in this chapter are tabulated in Table 6.2.

In XMM-Newton observation 0870830201, the source falls in the chip gap of the pn camera. Thus, the pn data are significantly affected. Therefore, we do not utilize the pn data of this observation for scientific analysis. In observation 0870830401, MOS1 data are not available. We utilize the `espfilt` task to clean the data from background flaring, and after that standard data reduction process is followed. The source region is selected from a 20 arcsec circle, and the background region is selected from a 40 arcsec circle in a nearby region from the

same chip. We select `FLAG==0` criteria for spectral extraction for all cameras. The spectra are grouped to have 20 counts per bin with an oversampling factor of 3.

The raw data of NuSTAR are cleaned and pre-processed using `nupipeline` with `saacalc=3`, `saamode=STRICT` and `tentacle=yes` parameters to maintain a conservative approach while handling the background due to South Atlantic Anomaly. The source extraction region is a 40 arcsec radius circle, and a nearby 60 arcsec radius circle from the same chip is chosen for the background region for all observations. The spectra are grouped to have 20 counts per energy bin.

6.2.2 | Analysis and Results

First, individual analysis of the joint XMM-Newton and NuSTAR spectra for all four epochs is carried out to investigate spectral characteristics and any variability over time. The neutral absorption model `tbabs` is used with updated abundance (Wilms et al. 2000) and cross-section (Verner et al. 1996). The uncertainties in parameters are estimated within a 90% confidence interval unless mentioned otherwise. The convolution model `cf1ux` is used to measure the flux. The XMM-Newton spectra are utilized in the 0.3–10.0 keV energy range, whereas the NuSTAR spectra are fitted in the 3.0–20.0 keV energy range, since beyond 20.0 keV, the spectra are significantly dominated by the background.

We start analyzing the spectra with an absorbed `powerlaw` model and find that the residual shows a broad feature around ~ 0.9 keV in all observations. However, depending on the S/N of the data, the measurement uncertainties on the parameters of the broad feature vary in different epochs. To take a simple approach to fit the broad feature, we follow the method by Earnshaw et al. 2019 and include a gaussian model component. The cross-calibration constant for MOS2 is fixed to 1 and left free to vary for other detectors. The presence of a typical powerlaw break is indicated in the broadband spectra, a feature that is common in other ULXs. In figure 6.1, we show the residual for an absorbed `powerlaw` fit for the XN1 epoch. The residual exhibits an apparent broad feature around ~ 0.9 keV and a high energy spectral cutoff. Hence, an additional multiplicative component `highcut` on top of the `powerlaw` continuum is invoked to fit the spectra for all epochs. Therefore, an absorbed `gaussian+highcut*powerlaw` model fits

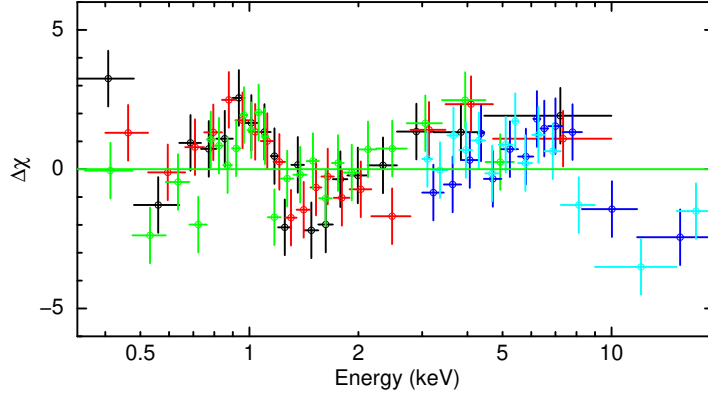


Figure 6.1: Presence of ~ 0.9 keV broad hump feature and a high energy spectral turnover is apparent from the residual of XN1 broadband spectra corresponding to an absorbed powerlaw fit. Data have been rebinned for visual purposes.

all cases well. We find that the spectral parameter throughout all observations of 2020-2021 remains congruent, implying that the source does not significantly vary in spectral nature during these observations. In figure 6.2, we plot the unfolded spectra from all four epochs. It is visually apparent from the figure that broadband spectra from these four epochs possess similar features. However, it is essential to note that for epoch XN2, some parameters are not properly constrained due to the unavailability of pn data but remain consistent within errors of the parameters from other epochs. Hence, we simultaneously fit the spectra for all 2020-2021 epochs with the same model with parameters for all epochs linked.

While simultaneously fitting all these spectra with an absorbed powerlaw, we get a $\chi^2/d.o.f \simeq 858/653$. When we add a gaussian component, the improved fit statistics is $\chi^2/d.o.f \simeq 705/650$. Nevertheless, an additional highcut component further improves the statistics. However, we find that with the addition of highcut component, the neutral absorption (N_H) gives a best-fit value close

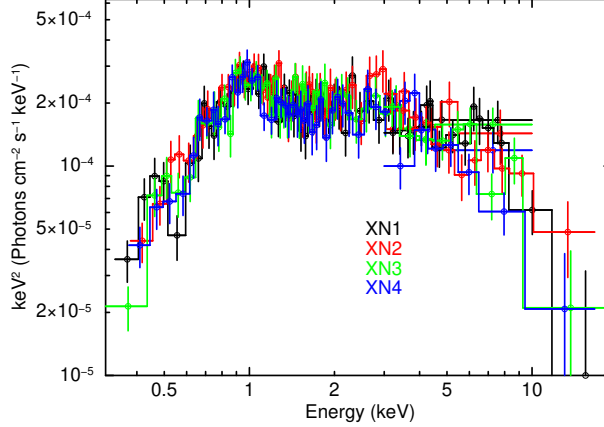


Figure 6.2: Unfolded broadband spectra of NGC 6946 X-1 for four simultaneous XMM-Newton and NuSTAR observations. The spectra are unfolded using a powerlaw model of 0 index and arbitrary normalization. For clarity, only MOS2 and FPMA spectra are exhibited for all four epochs. It is apparent from visual inspection that all four epochs show overlapping spectral features. Data have been rebinned for visual purposes.

to the Galactic absorption value $N_H \sim 0.22 \times 10^{22} \text{ cm}^{-2}$ (HI4PI Collaboration et al. 2016). This is apparently because NGC 6946 is a face-on galaxy, and the local absorption is less compared to the sensitivity of the data. Hence, we fix the N_H to the Galactic value throughout the analysis. We find that the cutoff and folding energies are around $E_{cut} \sim 6.34_{-0.63}^{+0.72} \text{ keV}$ and $E_{fold} \sim 4.06_{-1.06}^{+1.23} \text{ keV}$ with a powerlaw index of $\Gamma \sim 2.35_{-0.04}^{+0.03}$, portraying it as a soft source (see table 6.3). The $\chi^2/d.o.f$ is 556/649 for this simultaneous fit.

We also explore the cutoffpl model instead of the highecut*powerlaw to fit the continuum. We find that the gaussian+cutoffpl model fit gives the N_H value lower compared to the Galactic absorption; hence we fix this parameter to $0.22 \times 10^{22} \text{ cm}^{-2}$ as before and find that the $\chi^2/d.o.f$ is 601/650. An additional diskbb component provides lower $\chi^2/d.o.f$ of 553/648. However, we find that the folding energy of cutoffpl model gives high measurement uncertainty $E_{fold} = 3.20_{-2.20}^{+6.03} \text{ keV}$. Since this cutoffpl model could not provide a well-constrained description of the spectral cutoff, we do not discuss this model

any further for this source.

Finally, we study this source by simultaneously fitting all these four epochs spectra for different spectral models by linking the spectral parameters. This helps constrain the individual parameters with much better precision and, in turn, helps constrain the physical parameters we estimate from the analysis.

We primarily focus on the continuum spectral fitting of 2020-2021 broadband X-ray observations of NGC 6946 X-1. Thus, we undertake a simpler approach to fit the ~ 0.9 keV feature by a Gaussian model (see discussion in chapter 3 for NGC 4395 ULX1 (Ghosh et al. 2022), and discussion on such a similar feature in other ULXs, e.g., Middleton et al. 2015a, 2014). Different models have been invoked to perform the continuum fitting to explore the relevance of different physical scenarios expected in ULX systems. We find that a single component `diskpbb` model does not provide a good fit ($\chi^2/d.o.f \simeq 1340/654$). Significant residuals are observed in the soft energy range where typically soft disk blackbody component and the ~ 0.9 keV broad hump-like feature dominate the spectra. Hence, we utilize the well-explored two-component thermal disk models like `diskbb+diskpbb` to fit the continuum. A Gaussian on top of the two-component thermal disk continuum provides a statistically acceptable fit (see Table 6.4).

When we fit the `tbabs*(gaussian+diskbb+diskpbb)` model, we find that the cool inner disk temperature is around ~ 0.22 keV and the hot inner disk temperature is around ~ 2 keV. The radial dependence of temperature parameter ' p ' in `diskpbb` component converges to the hard limit of 0.5, i.e., the slim-disk limit. Hence, we fix this parameter to 0.5. Interestingly, no additional hard component is required for the 0.3–20.0 keV spectra in any epoch. Table 6.4 describes the model parameters and flux. Figure 6.3 shows the spectra, models, and residuals.

The light curves of NGC 6946 X-1 are analyzed with the motivation of searching for any pulsation in the source. As utilized for other ULX sources, the acceleration search technique is implemented with the HENDRICS (Bachetti 2018; Huppenkothen et al. 2019) tool `HENaccelesearch` in the frequency range of 0.01–6.8 Hz in XMM-Newton data and 0.01–10.0 Hz in NuSTAR data. Nevertheless, there is no significant detection of pulsation in any of the observations.

Table 6.3: Parameters for the fitted $\text{tbabs}*(\text{gaussian}+\text{highcut}*\text{powerlaw})$ model of NGC 6946 X-1 broadband spectra. The total absorbed flux (F_x) is measured in the 0.3–20.0 keV energy range.

Parameter	Unit	Parameter values
N_H	10^{22}cm^{-2}	0.22 (fixed)
E_{line}	keV	0.89 ± 0.03
σ_{line}	keV	$0.15^{+0.03}_{-0.02}$
$Norm$	$10^{-5} \text{photons cm}^{-2} \text{s}^{-1}$	$6.62^{+1.55}_{-1.20}$
E_{cut}	keV	$6.34^{+0.72}_{-0.63}$
E_{fold}	keV	$4.06^{+1.23}_{-1.06}$
Γ		$2.35^{+0.03}_{-0.04}$
$Norm_{pow}$	10^{-4}	2.61 ± 0.14
$\chi^2/d.o.f$		556/649
F_x	$10^{-13} \text{erg cm}^{-2} \text{s}^{-1}$	8.24 ± 0.41

6.2.3 | Discussions

We discuss the broadband spectral properties of a soft ULX source NGC 6946 X-1 from the 2020-2021 observations. Detection of emission lines from the high-resolution grating spectra by previous studies confirms the presence of wind/outflow in the system. The first broadband spectral properties of the source using XMM-Newton, NuSTAR, and Swift data were studied by [Earnshaw et al. 2019](#). They found that X-1 is a persistent ULX as its flux remained consistent with previous estimates (e.g., [Middleton et al. 2015a](#)). Interestingly, our analysis finds that even in 2020-2021 observations, X-1 shows flux $F_x \simeq (8.0 \pm 0.4) \times 10^{-13} \text{erg s}^{-1} \text{cm}^{-2}$ in 0.3–10.0 keV energy range, which is close to the previous findings. Hence, one can discern that NGC 6946 X-1 is indeed a persistent and steady ULX. One crucial comparison with the analysis of [Earnshaw et al. 2019](#) for the 2017 XMM-Newton+NuSTAR observation is the measurement of the N_H component. In the 2017 observation, the N_H is higher than in the 2020-2021 observations. We have verified that, even though we choose the Galactic absorption higher than that used in [Earnshaw et al. 2019](#), we find that the 2017 data can constrain an additional local absorption on top of the Galactic absorption. Another significant result is that the simultaneous fitting of these recent 2020-2021 data

Table 6.4: Parameters for the fitted $\text{tbabs}*(\text{gaussian}+\text{diskbb}+\text{diskpbb})$ model of NGC 6946 X-1 broadband spectra. The bolometric unabsorbed total flux and the flux from individual disk components are measured in the 0.01–100.0 keV energy range.

Parameter	Unit	Parameter values
N_H	10^{22}cm^{-2}	0.22 (fixed)
E_{line}	keV	0.92 ± 0.03
σ_{line}	keV	0.13 ± 0.03
$Norm$	$10^{-5} \text{photons cm}^{-2} \text{s}^{-1}$	$4.84^{+1.78}_{-1.20}$
T_{thin}	keV	$0.22^{+0.02}_{-0.03}$
$Norm_{thin}$		$8.48^{+7.22}_{-2.97}$
T_{slim}	keV	$2.03^{+0.13}_{-0.11}$
p		0.5 (fixed)
$Norm_{slim}$	10^{-4}	$4.45^{+1.31}_{-1.05}$
$\chi^2/d.o.f$		555/649
F_{unabs}^{bol}	$10^{-12} \text{erg cm}^{-2} \text{s}^{-1}$	2.61 ± 0.14
F_{diskbb}^{bol}	$10^{-13} \text{erg cm}^{-2} \text{s}^{-1}$	$4.17^{+0.61}_{-0.64}$
$F_{diskpbb}^{bol}$	$10^{-12} \text{erg cm}^{-2} \text{s}^{-1}$	2.12 ± 0.12

properly constrains the presence of spectral curvature in this ULX, an important feature of super-Eddington accretion in ULXs. We further discuss the implications of the spectral fittings and their relevance to the physical scenario in the ULX. Notably, these models are phenomenological, and any degeneracy between different model combinations can considerably impact the observational implications in the source spectra. With this caution, we primarily discuss the broadband spectral features and results from the thermal disk continuum models. The ~ 0.9 keV broad emission line feature, studied for several ULXs, has been simply treated here with a Gaussian model. We focus on the continuum properties and discuss some related physical aspects.

6.2.3.1 | Outflow scenario in super-critical accretion

There are ULX sources, e.g., NGC 247 ULX1, NGC 55 ULX, NGC 4395 ULX1, NGC 1313 X-1, NGC 5408 ULX1, NGC 300 X-1, Ho IX X-1, Ho II X-1, and NGC

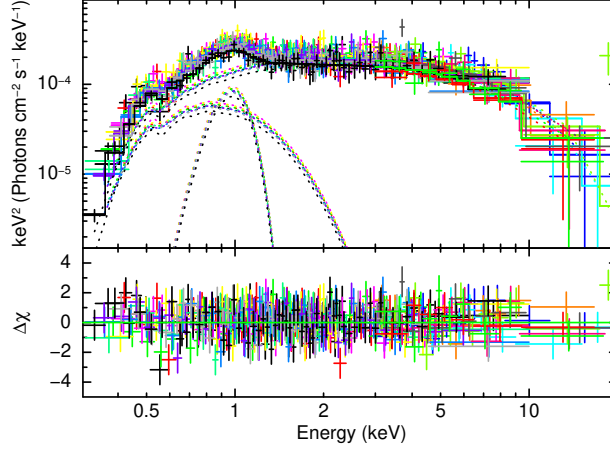


Figure 6.3: The NGC 6946 X-1 spectra, model components, and residuals are shown for all epochs simultaneous fit with $\text{tbabs}*(\text{gaussian}+\text{diskbb}+\text{diskpbb})$ model. Data have been rebinned for visual purposes.

5408 X-1 (Earnshaw & Roberts 2017; Ghosh et al. 2022; Middleton et al. 2015b; Pinto et al. 2016, 2017, 2021) where the strong ~ 0.9 keV feature is detected. In fact, predominantly, the bright sources with softer spectra exhibit such strong ~ 0.9 keV line emission/absorption features (Kosec et al. 2021). A similar ~ 0.9 keV feature is observed in NGC 6946 X-1 (see also Kosec et al. 2021; Middleton et al. 2015b; Pinto et al. 2016). The super-Eddington inflow of material is a possible reason for the origin of such wind or outflow (Takeuchi et al. 2013). The inclination angle of the system with the line of sight is a crucial factor that determines that the soft sources are the best candidates to show these line features. In a soft source, the inclination angle is close to the disk plane. Thus, we observe the inner hot photons only after being down-scattered by the wind, which eventually appear to us as soft photons. Also, due to such inclination, the wind clouds occult the inner disk, and we receive a higher fraction of line emission/absorption from the winds. The wind velocity and direction of its motion determine the strength and energy of the lines.

In NGC 6946 X-1, we see a moderate fraction of both soft and hard photons. Generally, the hard sources are understood as close to the face-on system so that

the hot inner region is aligned close to the line of sight, whereas the ultra-soft sources are perceived to be viewed close to edge-on. Hence, the accretion disk in NGC 6946 X-1 can be interpreted as moderately inclined towards the line of sight (see also [Pinto et al. 2017](#)). As discussed earlier, the notion of optically thick wind due to super-Eddington accretion as the source of the cool disk component in ULXs is widely accepted. We obtain that the bolometric luminosity of the cool disk component is $L_{bol} = 4\pi D^2 F_{bol} \simeq 3 \times 10^{39} \text{ erg s}^{-1}$. If the host is a $\sim 10 M_{\odot}$ black hole, then the luminosity is marginally above the Eddington luminosity. On the other hand, if the host is a neutron star system, then the luminosity would correspond to a super-Eddington luminosity of the source. Therefore, it may be deduced that the soft spectral components, such as the cool accretion disk and the broad $\sim 0.9 \text{ keV}$ feature, are associated with the emission from optically thick wind owing to the accretion close to or above the Eddington accretion rate. On the other hand, the hard spectral component, described by a hot diskpbb model, can emerge from the inner accretion flow for a black hole or neutron star ULX system.

The diskpbb model with the temperature profile of $T(R) \propto R^{-0.5}$ signifies significant advective cooling and photon trapping in a slim accretion disk. In a black hole accretion scenario, it is understood that the inner radius of the hot slim disk is the inner stable circular orbit (ISCO). However, in the neutron star accretor scenario, if the neutron star is weakly or non-magnetized, the inner accretion flow will extend to the neutron star surface or the boundary layer and release energy in the form of an additional harder emission component. In the highly magnetized neutron star case, the inner accretion flow truncates at the magnetospheric radius (R_M). There, the emission from the accretion column can produce a harder emission component. However, the presence of significant outflowing wind can mask the additional harder spectral component from the line of sight, which might be the case from NGC 6946 X-1. The inclination angle of the disk is also a contributing factor in shrouding this additional hard spectral component. Hence, the two-thermal component represents physical accretion flows in both black hole and neutron star systems. We discuss these two scenarios in detail.

6.2.3.2 | Black hole model

The bolometric luminosity of the hot diskpbb component is estimated to be $L_{bol} = 4\pi D^2 F_{bol} \simeq 1.5 \times 10^{40} \text{ erg s}^{-1}$. Such high luminosity is expected to be generated via super-Eddington accretion and thus further justifies that the temperature profile of the inner region of the disk diverges from standard thin disk and takes the form of $T(R) \propto R^{-0.5}$. It is important to discuss that typically, for a spherical emitter, $L_{bol} = 4\pi D^2 F_{bol}$ relation is justified. However, for accretion disks, it is shown that $L_{bol} = (2\pi D^2 / \cos \theta) F_{bol}$ is appropriate (Fukue 2000; Urquhart & Soria 2016), and the estimated luminosity will be dependent on the disk inclination angle. Nevertheless, it is common practice to estimate L_{bol} from $4\pi D^2 F_{bol}$, which is equivalent to the case of accretion disk at 60° inclination. However, for super-critical disks, the self-occultation of the disk due to the geometrical thickness at a high inclination angle and self-irradiation further modifies this simple flux-luminosity relation (Fukue 2000). However, for simplicity, we consider the $L_{bol} = (2\pi D^2 / \cos \theta) F_{bol}$ relation in our work.

From the spectral fitting, we can quantify some important physical parameters. We calculate the inner radius of the disk from the best-fit normalization of the hot disk component ($\sim 4.45 \times 10^{-4}$). Here, we assume a constant radius of the accretion disk. As discussed in chapter 3, the inner disk radius is given by the form $R_{in} = \zeta \kappa^2 N^{0.5} D_{10} (\cos \theta)^{-0.5} \text{ km}$, where N is the normalization, θ is the disk inclination, D_{10} is the distance to the source in 10 kpc unit, ζ is the geometric and κ is the color correction factor (Kubota et al. 1998; Soria et al. 2015). For a Keplerian orbit, the inner radius and the mass of the black hole are related by the form $R_{in} = 6\alpha \frac{GM}{c^2}$, where α is a function of spin parameter and can take the value of 1 for a non-rotating black hole, or ~ 0.21 for an extremely rotating (prograde) Kerr black hole with spin parameter $a^* \sim 0.998$ (Bardeen et al. 1972; Thorne 1974). For the inner hot diskpbb component, using the ζ and κ factors as 0.353 and 3 (Soria et al. 2015; Vierdayanti et al. 2008), respectively, we estimate the inner radius as $\sim 50(\cos \theta)^{-0.5} \text{ km}$. This would correspond to a $\sim 6 M_\odot$ black hole for a non-rotating and face-on system. The disk inclination angle can significantly influence the mass estimate. However, as discussed earlier, it is generally understood that the supersoft ULX sources are observed at

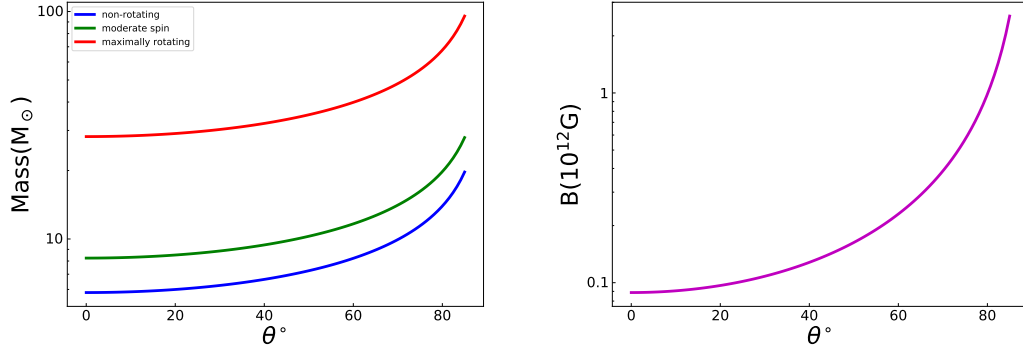


Figure 6.4: Left: For three different spins of the black hole, the variation of the estimated mass as a function of the disk inclination angle is shown. The non-rotating black hole scenario of $a^* = 0$, a moderate spin of $a^* = 0.5$, and a maximally rotating case of $a^* = 0.998$ are shown in the figure. Right: The dependency of estimated magnetic field strength for a neutron star system on the disk inclination angle is depicted.

a high-inclination (close to edge-on) angle. On the contrary, the ULXs, where a hot inner disk component is prominently visible, are understood as low inclination systems (Gu et al. 2016). Thus, for a realistic disk inclination $< 60^\circ$ for NGC 6946 X-1, the mass would be $< 10 M_{\odot}$ for a non-rotating black hole. Simulations for super-critical accretion onto black holes have shown a different perspective of the beaming effect in generating hard X-ray emission in ULXs. For example, Jiang et al. 2014 found that the hard X-ray emissions from the central region are broadly isotropic, whereas, on the contrary, Sądowski & Narayan 2016 found that there is significant beaming along the polar axis.

In figure 6.4 (left), we show the dependency of mass estimate on the disk inclination with different black hole spin. Caution is necessary because this mass estimate depends on the assumption of a Keplerian orbit of constant radius, which might be different in reality depending on the geometry of the disk.

6.2.3.3 | Neutron star model

In a neutron star system, it can be interpreted that the inner hot disk is truncated at the magnetospheric radius (R_M). As discussed in chapter 3, typically R_M is

related to the luminosity by the relation, $R_M = 7 \times 10^7 \Lambda m_1^{1/7} R_6^{10/7} B_{12}^{4/7} L_{39}^{-2/7}$ cm, where $m_1 = M/M_\odot$ is the neutron star mass in solar mass units, $B_{12} = B/10^{12}$ G, $L_{39} = L/10^{39}$ erg s⁻¹, $R_6 = R/10^6$ cm and for disk accretion $\Lambda \sim 0.5$ (Mushtukov et al. 2017). This relation is assumed for a dipole structure magnetic field lines around the neutron star. If we assume that the diskpbb component represents the hot inner region of the disk, then we can estimate typical magnetic field strength equating the inner radius with the R_M . We find that for a $1.4 M_\odot$ neutron star and radius of 10^6 cm, the magnetic field $B \sim 2 \times 10^{11}$ G for a 60° inclined disk with bolometric inner disk luminosity $\sim 1.5 \times 10^{40}$ erg s⁻¹. We plot the estimated magnetic field strength and corresponding disk inclination angle in figure 6.4 (right). In the plot, the bolometric luminosity depends on the angle as $\sim 1.5 \times 10^{40}$ erg s⁻¹ / $(2 \cos \theta)$. Since X-1 is not expected to be an extremely high inclination system, this simple angle dependence of luminosity is viable. In realistic inclination, $< 60^\circ$ case, the strength of the field is $B \lesssim 2 \times 10^{11}$ G. Hence, if NGC 6946 X-1 is a neutron star system, then it probably hosts a moderately magnetized neutron star core.

Several studies have explored different spectral models to justify the neutron star scenario in ULX systems. One characteristic feature is to study the power-law model with a high-energy exponential cutoff. The spectral cutoff in neutron stars is often identified as the emission from the accretion column (Walton et al. 2018a). Pintore et al. 2017, investigated the pulsator-like spectra in ULXs by characterizing them with `highcut*powerlaw` model. NGC 6946 X-1 was studied in the sample with archival XMM-Newton only data. Along with an exponentially cutoff powerlaw continuum, a soft blackbody excess and the ~ 1 keV feature were detected. However, our analysis finds that the latest broadband data are sufficiently well fitted with a `gaussian+highcut*powerlaw` model. Nevertheless, we study a crucial comparison with the pulsator-like spectral model and estimate the hardness and softness ratio as defined in Pintore et al. 2017. We estimate the total unabsorbed flux in 6.0–30.0 keV, 4.0–6.0 keV, and 2.0–4.0 keV bands. We find that hardness $\frac{F_x(6.0-30.0)}{F_x(4.0-6.0)} \sim 1$ and softness $\frac{F_x(2.0-4.0)}{F_x(4.0-6.0)} \sim 2$. This result remains similar to the finding in Pintore et al. 2017. Typically, neutron star systems are expected to have more hardness and lesser softness values. This study can indicate that if X-1 is a neutron star system, then it is not highly mag-

netized, consistent with our estimates, thus making the source less hard. Again, the inclination angle of the disk and the presence of optically thick wind also play a role in determining the hardness of the source.

6.2.3.4 | Accretion onto X-1

The spectral properties of NGC 6946 X-1 provide evidence of super-critical accretion onto a low massive black hole or a moderately magnetized neutron star. Also, an apparent signature of the optically thick wind is expected in such a super-critical accretion scenario. This helps us constrain some physical accretion parameters from a realistic point of view.

As discussed before in chapter 1, the total accretion luminosity in a super-critical accretion disk can be related to the Eddington ratio ($\dot{m}_0 = \dot{m}/\dot{m}_{Edd}$) by the following relation (Shakura & Sunyaev 1973),

$$L \simeq L_{Edd}[1 + \ln \dot{m}_0] \quad (6.1)$$

To estimate the physical parameters, we make some assumptions. The total bolometric unabsorbed luminosity is considered for further calculation. To estimate the luminosity, we have assumed a disk inclination angle of 60° , so that $L_{bol} = 4\pi D^2 F_{bol} = 1.9 \times 10^{40} \text{ erg s}^{-1}$, which is equivalent to the apparent isotropic luminosity relevant for Eq. 6.1.

However, the important factor which constrains the \dot{m}_0 comes from the beaming (King & Lasota 2016; King 2009). An approximate beaming relation gives $b \simeq 73/\dot{m}_0^2$ and the Eddington luminosity is given by $L_{Edd} = 1.5 \times 10^{38} m_1 \text{ erg s}^{-1}$ (Poutanen et al. 2007). Then the relation becomes,

$$\frac{m_1}{L_{40}} \simeq \frac{4900}{\dot{m}_0^2(1 + \ln \dot{m}_0)}, \quad (6.2)$$

where, the accretor mass $m_1 = M/M_\odot$ and the luminosity determine the accretion rate.

As discussed in chapter 1, the spherization radius R_{sph} for a super-Eddington disk is determined by the accretion rate by (Begelman et al. 2006; King 2009; Shakura & Sunyaev 1973),

$$R_{sph} \simeq \frac{27}{4} \dot{m}_0 \frac{2GM}{c^2} \quad (6.3)$$

For the bolometric total luminosity of $1.9 \times 10^{40} \text{ erg s}^{-1}$, if we assume a neutron star of $1.4 M_\odot$, then $\dot{m}_0 \simeq 38$ or in the case of a $\sim 10 M_\odot$ black hole, $\dot{m}_0 \simeq 16$.

Eddington accretion rate ($\dot{m}_{Edd} \simeq 2 \times 10^{18} m_1 \text{ g s}^{-1}$) of a neutron star is $\sim 4.4 \times 10^{-8} M_\odot \text{ yr}^{-1}$. This gives the accretion rate of X-1 to be $\dot{m} = 1.7 \times 10^{-6} M_\odot \text{ yr}^{-1}$, if it is a neutron star. On the other hand, if it is a $10 M_\odot$ black hole, then $\dot{m}_{Edd} \sim 3.2 \times 10^{-7} M_\odot \text{ yr}^{-1}$ and \dot{m} for X-1 is $\sim 5 \times 10^{-6} M_\odot \text{ yr}^{-1}$.

The spherization radius R_{sph} is $\sim 1 \times 10^8 \text{ cm}$ for a neutron star system, and $\sim 3.2 \times 10^8 \text{ cm}$ for a $10 M_\odot$ black hole. As we have assumed the disk inclination of 60° , the inner radius from the hot disk component is $R_{in} \sim 70 \text{ km} \sim 7 \times 10^6 \text{ cm}$. If we assume $R_M \sim R_{in}$, then the magnetospheric radius is less than the R_{sph} of the neutron star estimate, i.e., $R_M < R_{sph}$.

In the scenario of launching of optically thick wind down the R_{sph} for a neutron star, the condition $R_M < R_{sph}$ is self-consistent (King & Lasota 2016). It is interesting to put a stringent constraint on the relation between \dot{m}_0 , the magnetic field strength B_{12} , and disk inclination θ from the self-consistent condition. If we assume that R_M is estimated from the inner disk luminosity (which depends on the inclination angle of the disk), then a simple estimate of the relation would be,

$$\dot{m}_0 > 16 (L_{39}^{sph})^{-2/7} B_{12}^{4/7} (\cos \theta)^{2/7}, \quad (6.4)$$

where L_{39}^{sph} is the apparent spherical luminosity from the disk in units of $10^{39} \text{ erg s}^{-1}$. Thus, the relation for NGC 6946 X-1 would become,

$$\dot{m}_0 > 7 B_{12}^{4/7} (\cos \theta)^{2/7}, \quad (6.5)$$

which is satisfied by the estimated accretion rate and magnetic field for relevant, realistic disk inclination angles. It is important to note that Eq. 6.4 is a general relation, whereas Eq. 6.5 gives the specific condition for the source NGC 6946 X-1.

The non-detection of pulsation in this source possibly implies that R_M is much smaller than the estimated R_{in} , and thus the pulsation is diluted to be de-

tected (Walton et al. 2018a). In that case, the estimated magnetic field in section 6.2.3.3 could be further weaker with lesser R_M . Thus, a necessary condition for a neutron star ULX to be detected as a pulsar is $R_M \simeq R_{sph}$, and as a consequence, these systems must possess high spin-up rates as discussed in King et al. (2017). In the case of a $10 M_\odot$ black hole also, R_{in} which may be comparable to the inner stable circular orbit radius (R_{ISCO}), is much smaller than the R_{sph} .

In summary, NGC 6946 X-1 is a persistent soft ultraluminous X-ray source. Detection of spectral curvature, presence of wind/outflow, and high bolometric luminosity of a hot slim accretion disk scenario prefer super-Eddington accretion onto a stellar mass compact object. If the host is a non-rotating black hole, the realistic measurement indicates that the mass would be $< 10 M_\odot$, or the ULX can host a moderately magnetized neutron star. The estimates of physical length scales are consistent with a geometry where the disk height is extended down the R_{sph} and gets truncated at the R_{ISCO} of a black hole or R_M of a neutron star.

6.3 | Accretion constraint on other ULXs

A detailed study of NGC 6946 X-1 with broadband X-ray data and discussion of different spectral models mapped out the possible underlying physical scenarios of super-Eddington accretion. We further study some other bright ULX sources in this context to understand the accretion mechanism of these sources. We primarily focus on studying the spectral properties of these sources (mentioned in table 6.1) with available XMM-Newton data. To have a consistent outlook for the spectral properties of each of these sources, we restrict the analysis only to the soft energy band with XMM-Newton owing to the high effective area of the instrument. The data reduction of these sources follows the standard method discussed in Chapter 2.

Table 6.5: Observation log of XMM-Newton data for four sources. In observation ID 0654650101 of NGC 4190 ULX1, the flaring corrected cleaned exposure time of pn data is extremely low (~ 0.1 ksec), hence not utilized for the spectral analysis.

Serial No.	Observation ID	Observation date	Spectral Exposure time (ksec) pn/MOS1/MOS2
NGC 4190 ULX1			
1	0654650101	2010-06-06	-/3.7/4
2	0654650201	2010-06-08	4/12.4/12.3
3	0654650301	2010-11-25	6.3/10.4/11
NGC 1291 ULX1			
1	0201690201	2005-01-03	15.2/17.5/17.8
NGC 4254 X2			
1	0147610101	2003-06-29	7.2/11/12
2	0742240801	2016-12-27	12.4/23/17.4
3	0913090101	2023-01-01	52.5/76.3/80
NGC 4244 ULX1			
1	0553880201	2008-11-16	17.5/25.7/26.7

6.3.1 | Observations and Results

The XMM-Newton observations utilized for these analyses are mentioned in Table 6.5.

NGC 4190 ULX1 (RA: 12:13:45, Dec.: +36:37:55; the galactic distance of ~ 2.9 Mpc; [Kosec et al. 2018a](#)) is a bright ULX source in a nearby low surface brightness galaxy NGC 4190. The source has been observed by XMM-Newton three times. Previously, this source has been studied (e.g., [Koliopanos et al. 2017](#); [Sutton et al. 2014, 2013](#)) in a sample of sources in the purview of interpreting some of its spectral properties and studying the fractional variability. We include this bright source in our sample of ULXs to analyze its X-ray spectral characteristics in light of the super-Eddington accretion mechanism discussed in the previous section with relevant spectral models and comprehend its underlying physical scenarios. A 30 arcsec circle source and 60 arcsec circle background regions are chosen for the analysis.

NGC 1291 ULX1 (RA: 3:17:13.82, Dec.: -41:10:34.6; [Swartz et al. 2004](#)) is another bright ULX with a galactic distance of ~ 8.6 Mpc ([Liu & Bregman 2005](#)).

The source is located at the outer ringlike spiral of the galaxy NGC 1291. We utilize the only available archival XMM-Newton data of this source and study its spectral properties in detail. A 20 arcsec circle source and 40 arcsec circle background regions are chosen for the analysis.

NGC 4254 X2 (RA: 12:18:56.1, Dec.: +14:24:19; the galactic distance of ~ 33.2 Mpc; Sutton et al. 2012) is an important source in the sample since it has the hardest spectrum. Sutton et al. 2012 studied NGC 4254 X2 with one XMM-Newton data (ID - 0147610101). We discuss all available XMM-Newton data in our analysis, including one data set we obtained from our proposal for this source (ID - 0913090101). The new XMM-Newton data with high exposure time indicates some interesting features of this source spectra, which we discuss here. A 20 arcsec circle source and 40 arcsec circle background regions are chosen for the analysis.

On the other hand, NGC 4244 ULX1 is the softest source in our sample (RA: 12:16:56.927, Dec.: +37:43:35.89; the galactic distance ~ 3.6 Mpc; Liu & Mirabel 2005). This source was discovered to be a ULX with extremely steep spectra by Chandra data (Cagnoni et al. 2003). The source was observed by XMM-Newton three times. However, only in one XMM-Newton observation was the source detected in an active state, which we discuss here. A 20 arcsec circle source and 40 arcsec circle background regions are chosen for the analysis.

We give a generic treatment to these sources by studying the standard spectral models employed in ULXs. Thus, we can shed light on the possible variations and similarities among these sources. The simple powerlaw fitting of XMM-Newton data of these sources give powerlaw index values in the range of ~ 1.7 – 2 for NGC 4190 ULX1 and NGC 1291 ULX1, ~ 1.4 – 1.9 for NGC 4254 X2, and ~ 4 for NGC 4244 ULX1 (see table 6.6). Thus, we can interpret that the softest among the samples is NGC 4244 ULX1. NGC 4254 X2 is the hardest, and the other two sources, NGC 4190 ULX1 and NGC 1291 ULX1, possess intermediate hardness. The typical unabsorbed luminosity in 0.3–10.0 keV energy band for the best-fit of powerlaw model ranges between $\sim (3$ – $8) \times 10^{39}$ erg s $^{-1}$ for NGC 4190 ULX1, $\sim 3.5 \times 10^{39}$ erg s $^{-1}$ for NGC 1291 ULX1, $\sim (3$ – $7) \times 10^{40}$ erg s $^{-1}$ for NGC 4254 X2, and $\sim 3 \times 10^{39}$ erg s $^{-1}$ for NGC 4244 ULX1. In the case of NGC 4254 X2, for epochs 0147610101 and 0742240801, the powerlaw model provides

a sufficiently good fit, possibly owing to their low count statistics. We, therefore, utilize only the new observation (ID - 0913090101) of this source for further complicated models.

As prescribed by [Sutton et al. 2013](#), if we add a `diskbb` component on top of the `powerlaw` continuum in the high S/N observations, the source spectral states are manifested as the broadened disk (BD) state for NGC 4190 ULX1 and NGC 1291 ULX1; a hard ultraluminous (HUL) state for NGC 4254 X2. For NGC 4244 ULX1, the spectral state mostly resembles a soft or supersoft ultraluminous (SUL/SSUL) state.

We also explore the exponential cutoff powerlaw model to see if the typical break in the spectra is apparent in these sources. We could detect the cutoff within the XMM-Newton energy band in most sources except NGC 4254 X2. In table 6.7, we report the spectral fitting parameters for this specific model. It is important to note that for NGC 4244 ULX1, the folding energy (E_{fold}) ranges within a lower value compared to other ULXs, which is expected owing to its soft spectral nature. For NGC 4190 ULX1, the single-component cutoff powerlaw model is well-constrained, confirming the curvature in its spectra. For NGC 1291 ULX1 also, the cutoff powerlaw component is well-fitted; however, we find that the lower limit of N_H value gives a smaller value compared to the Galactic column density. Hence, we fix the N_H to its best-fit value as mentioned in table 6.7.

For NGC 4254 X2, the single cutoff powerlaw component in the spectra is not well constrained. We find that for NGC 4254 X2, an additional soft disk component helps constrain the cutoff with a better statistical fit. However, even in that case, the photon index of `cutoffpl` component is not well constrained. Hence, we fix the photon index value to 0.59 ([Walton et al. 2020](#)), a typical value consistent with pulsar ULX spectra (see also the analysis of NGC 1042 ULX1 in Chapter 4). Thus, we report the NGC 4254 X2 spectral fitting with a `diskbb+cutoffpl` model in table 6.8.

Henceforth, we further explore the widely used single component `diskpbb` model for all these sources. We find significant differences in the parameters for different sources. The `diskpbb` thermal model gives an acceptable statistical fit for the NGC 4190 ULX1 and NGC 1291 ULX1 spectra. The hot disk in the “ p ”

Table 6.6: The fitting parameters for `tbabs*powerlaw` model for four sources. The flux (F_x) is the absorbed flux in 0.3–10.0 keV energy range.

Observation ID	N_H 10^{22}cm^{-2}	Γ	Norm (10^{-4})	$\chi^2/d.o.f$	F_x $10^{-12} \text{erg cm}^{-2} \text{s}^{-1}$
NGC 4190 ULX1					
0654650101	$0.22^{+0.06}_{-0.05}$	1.87 ± 0.12	$5.55^{+0.76}_{-0.66}$	82/65	$2.55^{+0.22}_{-0.20}$
0654650201	0.28 ± 0.02	1.98 ± 0.04	$8.23^{+0.43}_{-0.41}$	410/260	$3.24^{+0.11}_{-0.10}$
0654650301	0.23 ± 0.01	1.74 ± 0.03	$11.45^{+0.42}_{-0.40}$	430/321	6.06 ± 0.13
NGC 1291 ULX1					
0201690201	0.20 ± 0.04	$2.04^{+0.12}_{-0.11}$	$0.71^{+0.09}_{-0.08}$	98/76	0.28 ± 0.02
NGC 4254 X2					
0147610101	$0.37^{+0.10}_{-0.09}$	$1.70^{+0.18}_{-0.17}$	$0.77^{+0.17}_{-0.14}$	28/39	0.40 ± 0.05
0742240801	$0.17^{+0.06}_{-0.05}$	1.43 ± 0.12	$0.39^{+0.06}_{-0.05}$	43/64	0.31 ± 0.03
0913090101	0.14 ± 0.03	1.43 ± 0.07	0.24 ± 0.02	143/156	0.19 ± 0.01
NGC 4244 ULX1					
0553880201	0.32 ± 0.04	$4.09^{+0.21}_{-0.20}$	$1.98^{+0.22}_{-0.20}$	94/81	$0.28^{+0.01}_{-0.02}$

free MCD model (with a p -value close to ~ 0.6) in these two sources describes their broadened disk type spectral nature. The `diskpbb` model fit of the NGC 4254 X2 data manifests an unphysically high temperature of the disk. Hence, we do not report the spectral fitting parameters from this model in this source. NGC 4244 ULX1 provides a well-behaved fit with `diskpbb` model; however, the “ p ” parameter converges to 0.5, the slim disk limit (hence we fix this parameter), similar to the case of NGC 4395 ULX1, or NGC 6946 X-1 studied in this thesis. We report the spectral fitting parameters for this model in table 6.9. The residuals for the best-fit models in these four sources are shown in figure 6.5.

6.3.2 | Discussions

We explore different spectral models in a sample of ULX sources within a wide range of spectral hardness. The high energy spectral cutoff detected in NGC 4190 ULX1 and NGC 1291 ULX1 confirmed that these sources are not in the canonical hard state of XRBs. This high energy spectral cutoff could be a manifestation of super-Eddington accretion (Gladstone et al. 2009; Sutton et al. 2013) or the synchrotron spectral cutoff discussed in Chapter 5. The typical advection-

Table 6.7: The fitting parameters for `tbabs*cutoffpl` model for four sources. The flux (F_x) is the absorbed flux in 0.3–10.0 keV energy range.

Observation ID	N_H 10^{22}cm^{-2}	Γ	E_{fold} keV	Norm (10^{-4})	$\chi^2/d.o.f$	F_x $10^{-12} \text{erg cm}^{-2} \text{s}^{-1}$
NGC 4190 ULX1						
0654650101	< 0.13	$0.61^{+0.56}_{-0.39}$	$2.38^{+1.96}_{-0.62}$	$5.61^{+0.77}_{-0.67}$	68/64	$2.36^{+0.21}_{-0.20}$
0654650201	0.09 ± 0.03	0.64 ± 0.18	$2.27^{+0.36}_{-0.28}$	$8.32^{+0.43}_{-0.41}$	252/259	3.05 ± 0.10
0654650301	0.11 ± 0.02	0.93 ± 0.12	$3.86^{+0.68}_{-0.51}$	$11.36^{+0.40}_{-0.39}$	297/320	$5.77^{+0.13}_{-0.14}$
NGC 1291 ULX1						
0201690201	0.06(fixed)	$0.91^{+0.19}_{-0.20}$	$2.47^{+0.78}_{-0.51}$	$0.78^{+0.11}_{-0.09}$	82/76	0.26 ± 0.02
NGC 4254 X2						
0913090101	0.14 ± 0.03	$1.43^{+0.07}_{-0.14}$	> 24	0.24 ± 0.02	143/155	0.19 ± 0.01
NGC 4244 ULX1						
0553880201	$0.18^{+0.06}_{-0.07}$	$2.25^{+1.15}_{-1.12}$	$0.91^{+1.58}_{-0.37}$	$4.76^{+4.39}_{-2.10}$	87/80	0.27 ± 0.01

Table 6.8: The fitting parameters for `tbabs*(diskbb+cutoffpl)` model for NGC 4254 X2. The flux (F_x) is the absorbed flux in 0.3–10.0 keV energy range.

Observation ID	N_H 10^{22}cm^{-2}	T_{in}^{cool} keV	$Norm_{cool}$	Γ	E_{fold} keV	Norm (10^{-5})	$\chi^2/d.o.f$	F_x $10^{-12} \text{erg cm}^{-2} \text{s}^{-1}$
NGC 4254 X2								
0913090101	$0.20^{+0.09}_{-0.07}$	$0.31^{+0.09}_{-0.06}$	$0.29^{+0.81}_{-0.21}$	0.59(fixed)	$5.96^{+1.71}_{-1.06}$	$1.51^{+0.27}_{-0.26}$	129/154	0.19 ± 0.01

Table 6.9: The fitting parameters for `tbabs*(diskpbb)` model for three sources. The flux (F_x) is the absorbed flux in 0.3–10.0 keV energy range.

Observation ID	N_H 10^{22}cm^{-2}	T_{in} keV	p	Norm	$\chi^2/d.o.f$	F_x $10^{-12} \text{erg cm}^{-2} \text{s}^{-1}$
NGC 4190 ULX1						
0654650101	< 0.16	$1.59^{+0.54}_{-0.30}$	$0.65^{+0.14}_{-0.08}$	< 0.045	68/64	$2.33^{+0.21}_{-0.19}$
0654650201	0.12 ± 0.03	$1.52^{+0.12}_{-0.10}$	$0.64^{+0.04}_{-0.03}$	$1.86^{+1.00}_{-0.67} \times 10^{-2}$	248/259	3.03 ± 0.10
0654650301	0.14 ± 0.02	$2.15^{+0.19}_{-0.15}$	0.61 ± 0.02	$0.75^{+0.34}_{-0.25} \times 10^{-2}$	299/320	$5.73^{+0.13}_{-0.14}$
NGC 1291 ULX1						
0201690201	0.09 ± 0.06	$1.49^{+0.42}_{-0.25}$	$0.60^{+0.08}_{-0.05}$	< 0.004	81/75	0.26 ± 0.02
NGC 4244 ULX1						
0553880201	0.12 ± 0.02	0.37 ± 0.03	0.5(fixed)	$0.44^{+0.22}_{-0.15}$	93/81	0.27 ± 0.01

dominated accretion disk-like spectral feature, represented by a “ p ” free disk with p value ~ 0.6 , further justifies the super-Eddington accreting nature of these two sources. The hot inner disk temperature as a characteristic temperature in the observed spectra indicates that these two sources are low inclination systems, such that the inner regions are visible along the line of sight.

NGC 4254 X2 is a persistent hard source. The parameters of `cutoffpl` com-

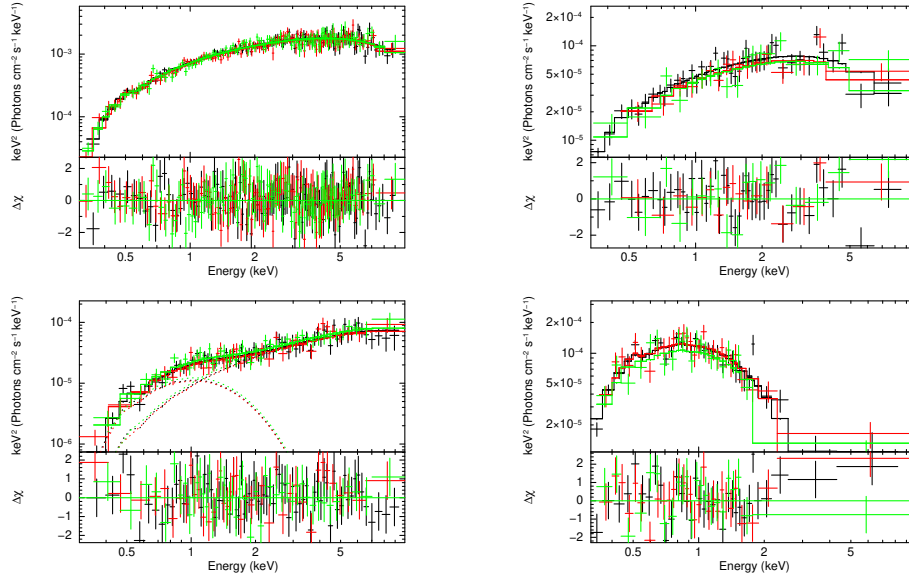


Figure 6.5: The best-fit spectra with models and residuals are shown for four sources. NGC 4190 ULX1 (top left; ID - 0654650301), NGC 1291 ULX1 (top right; ID - 0201690201), NGC 4254 X2 (bottom left; ID - 0913090101), and NGC 4244 ULX1 (bottom right; ID - 0553880201) spectra are shown. The `diskbb+cutoffpl` model fit is shown for NGC 4254 X2, and the `diskpbb` model fit is shown for the other three sources.

ponent are consistent with the parameters found in pulsar ULX sources, along with a strong presence of a cool thermal component. The hard nature of this source could be related to the low inclination angle of the source towards the line of sight, such that the direct hard emission from the inner region is beamed toward the observer. The presence of spectral curvature consistent with the values seen in pulsar ULXs and a cool thermal component, representing the optically thick wind, may indicate that the hard source NGC 4254 X2 is a super-Eddington stellar mass accretor.

NGC 4244 ULX1 is a transient soft ULX source with close proximity to the spectral feature of SSUL sources. A slim disk with $p = 0.5$ of the “ p ” free disk can describe the source spectra. This can be interpreted as strong advection in the inner region of the accretion disk of the source, similar to soft sources like NGC 4395 ULX1 and NGC 6946 X-1. In fact, as argued by [Urquhart & Soria 2016](#),

these supersoft ultraluminous sources can be explained as super-Eddington accreting ULXs observed through the densest outflowing wind.

To summarize, all four sources, NGC 4190 ULX1, NGC 1291 ULX1, NGC 4254 X2, and NGC 4244 ULX1, exhibit spectral characteristics that manifest a common accretion mechanism of super-Eddington accretion process similar to what we observe in other ULXs including NGC 6946 X-1.

Summary and Future prospects

7.1 | Summary

This thesis aims to investigate the spectral and timing properties of some individual ULXs, interpreting the insights of their physical accretion and emission mechanism and striding to map out a generic picture for some of the unique spectral characteristics of ULXs. The main results of the thesis are primarily described in four chapters, namely chapters 3, 4, 5, and 6. The summary of each of these chapters is briefly mentioned below.

7.1.1 | Hard X-ray flaring in NGC 4395 ULX1

We analyze recent XMM-Newton observations of a nearby ULX, NGC 4395 ULX1, and detect X-ray flaring events in a short time scale for the first time in the source. We find that the flaring incidents are spectrally harder compared to the non-flaring episodes. Thus, the fractional variability in the source light curve is significantly high for harder photons. The continuum spectra for all epochs are best described by two thermal components, namely a Keplerian disk and a slim accretion disk. On top of the continuum, we find a broad feature around ~ 0.9 keV, which is apparently associated with the forest of emission/absorption lines. This broad feature suggests wind/outflow in the ULX due to super-critical accretion. Interestingly, the flaring spectra exhibit higher slim inner disk temperature, suggesting a higher accretion rate and advection-dominated accre-

tion scenario. The non-flaring episodes exhibit steady temperatures for the inner hot and outer cool disks throughout different observations. The inner disk luminosity-temperature profile is broadly consistent with both $L \propto T^2$ and $L \propto T^4$ relations expected for advection-dominated and standard thin disk scenarios, respectively. The origin of such transient flaring events is best interpreted as an intrinsic variation in accretion rate and the presence of variable clumpy wind in the inner region of the accretion disk.

7.1.2 | Variability in spectra of NGC 1042 ULX1

Studying X-ray spectral variability in different ULXs sheds light on the variation in accretion scenarios in these sources. We study long-term data from XMM-Newton and report spectral variability in the X-ray band for a bright ULX NGC 1042 ULX1. The significant spectral variability is observed above ~ 1 keV, thus indicating that the hard spectral component like inner accretion flow, Comptonization process, or emission from NS accretion column gives rise to such variability. The characteristic cool thermal disk temperature of ~ 0.2 keV manifests similarities to the spectral states of UL state sources. We detect an apparent anti-correlation between luminosity and powerlaw index, thus suggesting that spectra become harder when the source is in a brighter state. Again, this feature can be related to variation in accretion rate, strong geometric beaming, varying strength in Comptonization, presence of wind/outflow in the system, or varying disk occultation. In general, the source exhibits HUL-type spectra and thus can be understood as a low-inclination system. The recent NuSTAR observation confirms the presence of characteristic spectral curvature in the source similar to other ULXs. All of these results conclude that the source is not an IMBH but another stellar-mass super-Eddington accretor.

7.1.3 | Synchrotron spectral cutoff in ULXs

Most ULX shows a unique spectral curvature at energies $E \simeq 10$ keV. However, the theoretical origin of such curvature is not well understood in the literature. We propose a novel mechanism based on the first principle of synchrotron radi-

ation to explain the origin of such spectral cutoff. We show that depending on the variation of latitude of the emitted synchrotron radiation, relativistic plasma within a configuration of neutron star magnetic field can give rise to such spectral cutoff. Analysis of two bright PULXs suggests that a large range of physical parameters can explain the spectra, for example, with an NS magnetic field of $B \simeq 10^{12} \text{ G}$, a semi-relativistic plasma with $\gamma \simeq 10\text{--}20$ for high latitude emission or a highly relativistic plasma ($\gamma \simeq 10^5\text{--}10^6$) for emission close to the electron's orbital plane would explain the spectra in a similar profile. We discuss that future studies with new data and polarimetric studies can decipher the method of distinctions from other proposed models to describe high-energy ULX spectra. If the new theoretical model is indeed the origin of spectral cutoff in ULXs, then most ULXs that show such spectral cutoff are neutron stars.

7.1.4 | Super-Eddington accretion mechanism in ULXs

We study some individual ULX sources with a varying range of spectral photon index. Most of the sources have shown spectral characteristics compatible with the expected physical mechanism in the super-Eddington accretion process. The broadband X-ray data of a persistent soft ULX source NGC 6946 X-1 shows the presence of a cool thermal accretion disk with temperature $T_{cool} \sim 0.2 \text{ keV}$ and a hot geometrically modified slim accretion disk with an inner temperature of $T_{hot} \sim 2 \text{ keV}$. The inner temperature radial profile is consistent with $T(R) \propto R^{-0.5}$, expected for a slim accretion disk. The presence of $\sim 0.9 \text{ keV}$ emission/absorption broad feature with a cool thermal disk-like component suggests the presence of optically thick wind due to super-critical accretion. With the assumptions of realistic disk inclination angle, we estimate the host compact object of NGC 6946 X-1 is comparable to $\sim 6\text{--}10 M_{\odot}$ non-rotating black hole or the ULX hosts a neutron star with $B \lesssim 2 \times 10^{11} \text{ G}$ magnetic field. Similar studies are explored with other sources like NGC 4190 ULX1, NGC 1291 ULX1, NGC 4254 X2, and NGC 4244 ULX1. Different spectral models provide distinct parameter space in these sources. However, the presence of spectral curvature and advection-dominated accretion disk in NGC 4190 ULX1 and NGC 1291 ULX1 suggest that these broadened disk sources are super-Eddington ac-

cretors. The hard ULX NGC 4254 X2 exhibits similar spectral parameters consistent to the pulsar ULX systems in terms of an exponential cutoff powerlaw along with a cool disk component, suggesting similar properties to the super-Eddington ULXs. NGC 4244 ULX1 is the softest ULX in the sample, with the presence of a slim accretion disk similar to the spectral characteristics of soft ULXs like NGC 4395 ULX1 and NGC 6946 X-1. All the spectra of these different sources imply the super-Eddington accretion mechanism, which eventually increases the sample size of super-Eddington accreting binary systems.

7.2 | Future Prospects

The works discussed in the thesis can be extended in the future for several prospective studies. A systematic study of searching for transient events in ULXs would help in establishing the variability in accretion mechanisms in ULX systems. Continuous monitoring of a population of ULXs is required for such investigations. As an extension, a systematic exploration of fractional variability measurement and quantitative estimates of energy-dependent light curves of such transient events would be helpful in the same direction.

A coherent examination of correlation measurements between different spectral parameters is well explored in XRB and AGN science. It would be prudent to have such systematic studies for a population of ULX sources, including high S/N data. In fact, more broadband data are necessary for such studies to properly constrain the soft and hard energy components and find the correlation between them. Such correlation studies would portray a complete picture of accretion in these sources.

We have developed a novel theoretical model to explain the spectral cutoff observed in ULXs. This model needs to be explored for more samples of sources and needs to be tested for XRB systems. Further developing the model in a general setting, which includes the properties of ambient medium generated from the accretion process, is important for future work. Broadband X-ray study of multiple ULXs with a complete description of soft energy components along with the high energy spectral curvature would further establish the picture of

the common physical environment in these sources.

Our brief sample study and implication of the super-Eddington accretion mechanism as the origin of such high power in ULXs is important to extend for a larger sample of sources with broadband data. The methods we have discussed to interpret the super-Eddington accretion and estimation process of mass, magnetic field, and accretion rate would be important for future statistical surveys and simulation studies of ULXs.

In the future, we would also focus on studying a special class of bright ULXs, known as HLXs, to understand the origin of their extreme luminosities. If the interpretation of IMBHs as a host of HLXs does not seem feasible from a robust survey of broadband X-ray data, then new theoretical models need to be explored to explain such high luminosities in these sources.

A robust search for pulsation in these sources warrants high S/N data with sufficient count statistics. We would look for more data to have meaningful studies in this direction. With a growing number of neutron star ULXs, a primary survey of the sources can be based on the works by [Pintore et al. 2017](#) and [Walton et al. 2018a](#). Once the spectral characteristics indicate pulsator-like behavior, a thorough search of pulsation can be executed in these sources.

In the future, it is also important to theoretically explore the origin of outflowing wind due to super-Eddington accretion flow and why they are predominantly found in soft ULX sources. In this regard, an extension of the study by [Qiu & Feng 2021](#) with more samples of sources would shed light on the physics of wind/outflow.

Finally, it is crucial to focus on understanding the canonical properties in ULXs with a large population study. We will also explore developing models on the polarization properties of ULXs, especially for pulsar ULXs in the booming era of X-ray polarimetric studies by instruments like IXPE or POLIX. Future missions like Advanced Telescope for High ENergy Astrophysics (Athena; [Barret et al. 2020](#)) and the X-ray Imaging and Spectroscopy Mission (XRISM; [XRISM Science Team 2020](#)) will be crucial to decipher more mysteries of ULXs owing to their high effective area and spectral resolution.

References

- Abramowicz, M., Jaroszynski, M., & Sikora, M. 1978, *A&A*, 63, 221
- Abramowicz, M. A., Czerny, B., Lasota, J. P., & Szuszkiewicz, E. 1988, *ApJ*, 332, 646
- Agrawal, V. K., & Nandi, A. 2015, *MNRAS*, 446, 3926
- Allen, G. E., Petre, R., & Gotthelf, E. V. 2001, *ApJ*, 558, 739
- Anand, G. S., Rizzi, L., & Tully, R. B. 2018, *AJ*, 156, 105
- Andersen, B. C., & Ransom, S. M. 2018, *ApJL*, 863, L13
- Arnaud, K. A. 1996, in *Astronomical Society of the Pacific Conference Series*, Vol. 101, *Astronomical Data Analysis Software and Systems V*, ed. G. H. Jacoby & J. Barnes, 17
- Atapin, K., Fabrika, S., & Caballero-García, M. D. 2019, *MNRAS*, 486, 2766
- Bachetti, M. 2018, HENDRICS: High ENergy Data Reduction Interface from the Command Shell, *Astrophysics Source Code Library*, record [ascl:1805.019](#)
- Bachetti, M., Rana, V., Walton, D. J., et al. 2013, *ApJ*, 778, 163
- Bachetti, M., Harrison, F. A., Walton, D. J., et al. 2014, *Nature*, 514, 202
- Bachetti, M., Maccarone, T. J., Brightman, M., et al. 2020, *ApJ*, 891, 44
- Bardeen, J. M., Press, W. H., & Teukolsky, S. A. 1972, *ApJ*, 178, 347
- Barra, F., Pinto, C., Walton, D. J., et al. 2022, *MNRAS*, 516, 3972
- Barret, D., Decourchelle, A., Fabian, A., et al. 2020, *Astronomische Nachrichten*, 341, 224

- Begelman, M. C. 2002, *ApJ*, 568, L97
- Begelman, M. C., King, A. R., & Pringle, J. E. 2006, *MNRAS*, 370, 399
- Blackburn, J. K. 1995, in *Astronomical Society of the Pacific Conference Series*, Vol. 77, *Astronomical Data Analysis Software and Systems IV*, ed. R. A. Shaw, H. E. Payne, & J. J. E. Hayes, 367
- Blackburn, J. K., Shaw, R. A., Payne, H. E., Hayes, J. J. E., & Heasarc. 1999, *FTOOLS: A general package of software to manipulate FITS files*, *Astrophysics Source Code Library*, record [ascl:9912.002](#)
- Boggs, P. T., & Rogers, J. E. 1990, *Contemporary Mathematics*, 112, 183
- Brightman, M., Harrison, F. A., Barret, D., et al. 2016, *ApJ*, 829, 28
- Brightman, M., Harrison, F. A., Fürst, F., et al. 2018, *Nature Astronomy*, 2, 312
- Brightman, M., Harrison, F. A., Bachetti, M., et al. 2019, *ApJ*, 873, 115
- Caballero, I., & Wilms, J. 2012, *Mem. Soc. Astron. Italiana*, 83, 230
- Cagnoni, I., Turolla, R., Treves, A., et al. 2003, *ApJ*, 582, 654
- Canuto, V., Lodenguai, J., & Ruderman, M. 1971, *Phys. Rev. D*, 3, 2303
- Carpano, S., Haberl, F., Maitra, C., & Vasilopoulos, G. 2018, *MNRAS*, 476, L45
- Cash, W. 1979, *ApJ*, 228, 939
- Colbert, E. J. M., & Mushotzky, R. F. 1999, *ApJ*, 519, 89
- D’Aì, A., Pinto, C., Del Santo, M., et al. 2021, *MNRAS*, 507, 5567
- D’Angelo, C. R., Fridriksson, J. K., Messenger, C., & Patruno, A. 2015, *MNRAS*, 449, 2803
- Davis, S. W., Narayan, R., Zhu, Y., et al. 2011, *ApJ*, 734, 111
- Dewangan, G. C., Griffiths, R. E., & Rao, A. R. 2006, *ApJ*, 641, L125
- Dimoudi, S., Adamek, K., Thiagaraj, P., et al. 2018, *ApJS*, 239, 28
- Dotan, C., & Shaviv, N. J. 2011, *MNRAS*, 413, 1623
- Earnshaw, H. M., & Roberts, T. P. 2017, *MNRAS*, 467, 2690
- Earnshaw, H. P., Grefenstette, B. W., Brightman, M., et al. 2019, *ApJ*, 881, 38

- Edelson, R., Turner, T. J., Pounds, K., et al. 2002, *ApJ*, 568, 610
- Fender, R. P., Belloni, T. M., & Gallo, E. 2004, *MNRAS*, 355, 1105
- Feng, H., & Kaaret, P. 2009, *ApJ*, 696, 1712
- Feng, H., & Soria, R. 2011, *New Astronomy Reviews*, 55, 166
- Foreman-Mackey, D., Hogg, D. W., Lang, D., & Goodman, J. 2013, *PASP*, 125, 306
- Frank, J., King, A., & Raine, D. 2002, *Accretion Power in Astrophysics*, 3rd edn. (Cambridge: Cambridge University Press)
- Fukue, J. 2000, *PASJ*, 52, 829
- Fürst, F., Walton, D. J., Stern, D., et al. 2017, *ApJ*, 834, 77
- Fürst, F., Walton, D. J., Harrison, F. A., et al. 2016, *ApJL*, 831, L14
- Fürst, F., Walton, D. J., Heida, M., et al. 2018, *A&A*, 616, A186
- Gabriel, C., Denby, M., Fyfe, D. J., et al. 2004, in *Astronomical Society of the Pacific Conference Series*, Vol. 314, *Astronomical Data Analysis Software and Systems (ADASS) XIII*, ed. F. Ochsenbein, M. G. Allen, & D. Egret, 759
- Gehrels, N., Chincarini, G., Giommi, P., et al. 2004, *ApJ*, 611, 1005
- Gendreau, K. C., Arzoumanian, Z., Adkins, P. W., et al. 2016, in *Society of Photo-Optical Instrumentation Engineers (SPIE) Conference Series*, Vol. 9905, *Space Telescopes and Instrumentation 2016: Ultraviolet to Gamma Ray*, ed. J.-W. A. den Herder, T. Takahashi, & M. Bautz, 99051H
- Ghosh, T., & Rana, V. 2021, *MNRAS*, 504, 974
- . 2022, *MNRAS*, 517, 4247
- . 2023a, *ApJ*, 949, 78
- . 2023b, *MNRAS*, 522, 1183
- Ghosh, T., Rana, V., & Bachetti, M. 2022, *ApJ*, 938, 76
- Ghosh, T., Sethi, S., & Rana, V. 2023, *ApJ*, 948, 62
- Giacconi, R., Gursky, H., Paolini, F. R., & Rossi, B. B. 1962, *Phys. Rev. Lett.*, 9, 439
- Gladstone, J. C., Roberts, T. P., & Done, C. 2009, *MNRAS*, 397, 1836

- Godet, O., Plazolles, B., Kawaguchi, T., et al. 2012, *ApJ*, 752, 34
- Goldreich, P., & Julian, W. H. 1969, *ApJ*, 157, 869
- Gu, W.-M., Sun, M.-Y., Lu, Y.-J., Yuan, F., & Liu, J.-F. 2016, *ApJL*, 818, L4
- Gúrpide, A., Godet, O., Koliopanos, F., Webb, N., & Olive, J. F. 2021a, *A&A*, 649, A104
- Gúrpide, A., Godet, O., Vasilopoulos, G., Webb, N. A., & Olive, J. F. 2021b, *A&A*, 654, A10
- Harrison, F. A., Craig, W. W., Christensen, F. E., et al. 2013, *ApJ*, 770, 103
- Heil, L. M., Vaughan, S., & Roberts, T. P. 2009, *MNRAS*, 397, 1061
- Heinz, S. 2004, *MNRAS*, 355, 835
- Hernández-García, L., Vaughan, S., Roberts, T. P., & Middleton, M. 2015, *MNRAS*, 453, 2877
- HI4PI Collaboration, Ben Bekhti, N., Flöer, L., et al. 2016, *A&A*, 594, A116
- Hirano, A., Kitamoto, S., Yamada, T. T., Mineshige, S., & Fukue, J. 1995, *ApJ*, 446, 350
- Homan, J., & Belloni, T. 2005, *Ap&SS*, 300, 107
- Homan, J., Wijnands, R., van der Klis, M., et al. 2001, *ApJS*, 132, 377
- Huppenkothen, D., Bachetti, M., Stevens, A. L., et al. 2019, *ApJ*, 881, 39
- Israel, G. L., Belfiore, A., Stella, L., et al. 2017a, *Science*, 355, 817
- Israel, G. L., Papitto, A., Esposito, P., et al. 2017b, *MNRAS*, 466, L48
- Jansen, F., Lumb, D., Altieri, B., et al. 2001, *A&A*, 365, L1
- Jiang, Y.-F., Stone, J. M., & Davis, S. W. 2014, *ApJ*, 796, 106
- Kaaret, P., & Feng, H. 2009, *ApJ*, 702, 1679
- Kaaret, P., Feng, H., & Roberts, T. P. 2017, *ARA&A*, 55, 303
- Kaaret, P., Simet, M. G., & Lang, C. C. 2006, *Science*, 311, 491
- Kajava, J. J. E., & Poutanen, J. 2009, *MNRAS*, 398, 1450
- Kara, E., Pinto, C., Walton, D. J., et al. 2020, *MNRAS*, 491, 5172
- King, A., & Lasota, J.-P. 2016, *MNRAS*, 458, L10

- . 2020, *MNRAS*, 494, 3611
- King, A., Lasota, J.-P., & Kluźniak, W. 2017, *MNRAS*, 468, L59
- King, A., Lasota, J.-P., & Middleton, M. 2023, *New Astronomy Reviews*, 96, 101672
- King, A. R. 2009, *MNRAS*, 393, L41
- King, A. R., Davies, M. B., Ward, M. J., Fabbiano, G., & Elvis, M. 2001, *ApJ*, 552, L109
- Kisaka, S., & Tanaka, S. J. 2017a, *ApJ*, 837, 76
- . 2017b, *Journal of Physics: Conference Series*, 932, 012015
- Koliopanos, F., Vasilopoulos, G., Godet, O., et al. 2017, *A&A*, 608, A47
- Körding, E., Falcke, H., & Markoff, S. 2002, *A&A*, 382, L13
- Kosec, P., Pinto, C., Fabian, A. C., & Walton, D. J. 2018a, *MNRAS*, 473, 5680
- Kosec, P., Pinto, C., Walton, D. J., et al. 2018b, *MNRAS*, 479, 3978
- Kosec, P., Pinto, C., Reynolds, C. S., et al. 2021, *MNRAS*, 508, 3569
- Kozłowski, M., Jaroszynski, M., & Abramowicz, M. A. 1978, *A&A*, 63, 209
- Krauss, M. I., Kilgard, R. E., Garcia, M. R., Roberts, T. P., & Prestwich, A. H. 2005, *ApJ*, 630, 228
- Kubota, A., & Makishima, K. 2004, *ApJ*, 601, 428
- Kubota, A., Tanaka, Y., Makishima, K., et al. 1998, *PASJ*, 50, 667
- Landau, L. D., & Lifshitz, E. M. 1975, *The classical theory of fields* (Oxford: Pergamon Press)
- Lasota, J.-P. 2016, in *Astrophysics and Space Science Library*, Vol. 440, *Astrophysics of Black Holes: From Fundamental Aspects to Latest Developments*, ed. C. Bambi, 1
- Lin, L. C.-C., Hu, C.-P., Takata, J., et al. 2022, *ApJ*, 924, 65
- Liu, J.-F., & Bregman, J. N. 2005, *ApJS*, 157, 59
- Liu, Q. Z., & Mirabel, I. F. 2005, *A&A*, 429, 1125
- Longair, M. S. 2011, *High Energy Astrophysics* (Cambridge: Cambridge University Press)
- Luangtip, W., Roberts, T. P., & Done, C. 2016, *MNRAS*, 460, 4417
- Lyutikov, M., & Gavriil, F. P. 2006, *MNRAS*, 368, 690

- Maccarone, T. J. 2005, *MNRAS*, **360**, L68
- Makishima, K., Maejima, Y., Mitsuda, K., et al. 1986, *ApJ*, **308**, 635
- Malacaria, C., Klochkov, D., Santangelo, A., & Staubert, R. 2015, *A&A*, **581**, A121
- Markoff, S., Nowak, M. A., & Wilms, J. 2005, *ApJ*, **635**, 1203
- Middleton, M. J., Heil, L., Pintore, F., Walton, D. J., & Roberts, T. P. 2015a, *MNRAS*, **447**, 3243
- Middleton, M. J., Roberts, T. P., Done, C., & Jackson, F. E. 2011, *MNRAS*, **411**, 644
- Middleton, M. J., Walton, D. J., Fabian, A., et al. 2015b, *MNRAS*, **454**, 3134
- Middleton, M. J., Walton, D. J., Roberts, T. P., & Heil, L. 2014, *MNRAS*, **438**, L51
- Mineshige, S., Hirano, A., Kitamoto, S., Yamada, T. T., & Fukue, J. 1994, *ApJ*, **426**, 308
- Mitsuda, K., Inoue, H., Koyama, K., et al. 1984, *PASJ*, **36**, 741
- Motta, S. E., Marelli, M., Pintore, F., et al. 2020, *ApJ*, **898**, 174
- Mushtukov, A. A., Ingram, A., Middleton, M., Nagirner, D. I., & van der Klis, M. 2019, *MNRAS*, **484**, 687
- Mushtukov, A. A., Suleimanov, V. F., Tsygankov, S. S., & Ingram, A. 2017, *MNRAS*, **467**, 1202
- Mushtukov, A. A., Suleimanov, V. F., Tsygankov, S. S., & Poutanen, J. 2015, *MNRAS*, **454**, 2539
- Mushtukov, A. A., Tsygankov, S. S., Suleimanov, V. F., & Poutanen, J. 2018, *MNRAS*, **476**, 2867
- Narayan, R., & Yi, I. 1995, *ApJ*, **452**, 710
- Nasa High Energy Astrophysics Science Archive Research Center (Heasarc). 2014, HEASoft: Unified Release of FTOOLS and XANADU, Astrophysics Source Code Library, record [ascl:1408.004](#)
- Pasham, D. R., Cenko, S. B., Zoghbi, A., et al. 2015, *ApJL*, **811**, L11
- Pasham, D. R., & Strohmayer, T. E. 2012, *ApJ*, **753**, 139
- Pasham, D. R., Strohmayer, T. E., & Mushotzky, R. F. 2014, *Nature*, **513**, 74
- Paul, B. 2022, in 44th COSPAR Scientific Assembly. Held 16-24 July, Vol. 44, 1853, [Abstract E1.12-0010-22](#)
- Pétri, J. 2016, *Journal of Plasma Physics*, **82**, 635820502

- Pinto, C., Middleton, M. J., & Fabian, A. C. 2016, *Nature*, 533, 64
- Pinto, C., Alston, W., Soria, R., et al. 2017, *MNRAS*, 468, 2865
- Pinto, C., Walton, D. J., Kara, E., et al. 2020, *MNRAS*, 492, 4646
- Pinto, C., Soria, R., Walton, D. J., et al. 2021, *MNRAS*, 505, 5058
- Pintore, F., Zampieri, L., Stella, L., et al. 2017, *ApJ*, 836, 113
- Pintore, F., Marelli, M., Salvaterra, R., et al. 2020, *ApJ*, 890, 166
- Pintore, F., Motta, S., Pinto, C., et al. 2021, *MNRAS*, 504, 551
- Poutanen, J., Lipunova, G., Fabrika, S., Butkevich, A. G., & Abolmasov, P. 2007, *MNRAS*, 377, 1187
- Qiu, Y., & Feng, H. 2021, *ApJ*, 906, 36
- Rana, V., Harrison, F. A., Bachetti, M., et al. 2015, *ApJ*, 799, 121
- Ransom, S. 2011, PRESTO: PulsAR Exploration and Search TOolkit, Astrophysics Source Code Library, record [ascl:1107.017](#)
- Ransom, S. M., Eikenberry, S. S., & Middleditch, J. 2002, *AJ*, 124, 1788
- Rao, F., Feng, H., & Kaaret, P. 2010, *ApJ*, 722, 620
- Remillard, R. A., & McClintock, J. E. 2006, *ARA&A*, 44, 49
- Reynolds, C. S. 2021, *ARA&A*, 59, 117
- Reynolds, S. P., & Keohane, J. W. 1999, *ApJ*, 525, 368
- Riegler, G., Bolt, E., & Serlemitsos, P. 1970, *Nature*, 226, 1041
- Rodríguez Castillo, G. A., Israel, G. L., Belfiore, A., et al. 2020, *ApJ*, 895, 60
- Rybicki, G. B., & Lightman, A. P. 1979, Radiative processes in astrophysics (New York: Wiley)
- Sadowski, A. 2011, *arXiv e-prints*, [arXiv:1108.0396](#)
- Sathyaprakash, R., Roberts, T. P., Walton, D. J., et al. 2019, *MNRAS*, 488, L35
- Schwinger, J., DeRaad, L., Milton, K., & Tsai, W.-Y. 1998, Classical Electrodynamics (1st ed.) (Boca Raton: CRC Press)

- Shakura, N. I., & Sunyaev, R. A. 1973, *A&A*, 24, 337
- Shapiro, S. L., & Teukolsky, S. A. 1983, *Black Holes, White Dwarfs, and Neutron Stars: The Physics of Compact Objects* (New York: Wiley)
- Shimura, T., & Takahara, F. 1995, *ApJ*, 445, 780
- Ŝadowski, A., & Narayan, R. 2016, *MNRAS*, 456, 3929
- Soria, R., Kuntz, K. D., Long, K. S., et al. 2015, *ApJ*, 799, 140
- Stobart, A. M., Roberts, T. P., & Warwick, R. S. 2004, *MNRAS*, 351, 1063
- Stobart, A. M., Roberts, T. P., & Wilms, J. 2006, *MNRAS*, 368, 397
- Straub, O., Godet, O., Webb, N., Servillat, M., & Barret, D. 2014, *A&A*, 569, A116
- Strohmayer, T. E., & Mushotzky, R. F. 2003, *ApJ*, 586, L61
- . 2009, *ApJ*, 703, 1386
- Strohmayer, T. E., Mushotzky, R. F., Winter, L., et al. 2007, *ApJ*, 660, 580
- Sutton, A. D., Done, C., & Roberts, T. P. 2014, *MNRAS*, 444, 2415
- Sutton, A. D., Roberts, T. P., & Middleton, M. J. 2013, *MNRAS*, 435, 1758
- Sutton, A. D., Roberts, T. P., Walton, D. J., Gladstone, J. C., & Scott, A. E. 2012, *MNRAS*, 423, 1154
- Swartz, D. A., Ghosh, K. K., Tennant, A. F., & Wu, K. 2004, *ApJS*, 154, 519
- Syunyaev, R. A., & Shakura, N. I. 1986, *Soviet Astronomy Letters*, 12, 117
- Takeuchi, S., Ohsuga, K., & Mineshige, S. 2013, *PASJ*, 65, 88
- Thorne, K. S. 1974, *ApJ*, 191, 507
- Urquhart, R., & Soria, R. 2016, *MNRAS*, 456, 1859
- Uttley, P., & McHardy, I. M. 2001, *MNRAS*, 323, L26
- Vasilopoulos, G., Koliopanos, F., Haberl, F., et al. 2021, *ApJ*, 909, 50
- Vaughan, S., Edelson, R., Warwick, R. S., & Uttley, P. 2003, *MNRAS*, 345, 1271
- Verner, D. A., Ferland, G. J., Korista, K. T., & Yakovlev, D. G. 1996, *ApJ*, 465, 487
- Vierdayanti, K., Watarai, K.-Y., & Mineshige, S. 2008, *PASJ*, 60, 653

- Vinokurov, A., Fabrika, S., & Atapin, K. 2018, *ApJ*, 854, 176
- Virtanen, P., Gommers, R., Oliphant, T. E., et al. 2020, *Nature Methods*, 17, 261
- Walton, D. J., Fuerst, F., Harrison, F., et al. 2013, *ApJ*, 779, 148
- Walton, D. J., Harrison, F. A., Grefenstette, B. W., et al. 2014, *ApJ*, 793, 21
- Walton, D. J., Harrison, F. A., Bachetti, M., et al. 2015a, *ApJ*, 799, 122
- Walton, D. J., Middleton, M. J., Rana, V., et al. 2015b, *ApJ*, 806, 65
- Walton, D. J., Fürst, F., Heida, M., et al. 2018a, *ApJ*, 856, 128
- Walton, D. J., Fürst, F., Harrison, F. A., et al. 2018b, *MNRAS*, 473, 4360
- Walton, D. J., Pinto, C., Nowak, M., et al. 2020, *MNRAS*, 494, 6012
- Watarai, K.-y., Fukue, J., Takeuchi, M., & Mineshige, S. 2000, *PASJ*, 52, 133
- Webb, N. A., Barret, D., Godet, O., et al. 2010, *ApJL*, 712, L107
- Weisskopf, M. C., Brinkman, B., Canizares, C., et al. 2002, *PASP*, 114, 1
- Weisskopf, M. C., Ramsey, B., O'Dell, S., et al. 2016, in *Society of Photo-Optical Instrumentation Engineers (SPIE) Conference Series*, Vol. 9905, *Space Telescopes and Instrumentation 2016: Ultraviolet to Gamma Ray*, ed. J.-W. A. den Herder, T. Takahashi, & M. Bautz, 990517
- West, L. A., Lehmer, B. D., Wik, D., et al. 2018, *ApJ*, 869, 111
- Wilms, J., Allen, A., & McCray, R. 2000, *ApJ*, 542, 914
- XRISM Science Team. 2020, *arXiv e-prints*, arXiv:2003.04962
- Yang, Q.-X., Xie, F.-G., Yuan, F., et al. 2015, *MNRAS*, 447, 1692